



TECHNISCHE
UNIVERSITÄT
WIEN

Vienna University of Technology

Dissertation

Ion-beam induced magnetic nano-structures of Fe grown on Cu(100)

*ausgeführt zum Zwecke der Erlangung des akademischen Grades eines
Doctors der technischen Wissenschaften unter der Leitung von*

Ao.Univ.Prof.Dipl.-Ing.Dr.techn. Peter Varga

E134

Institut für Angewandte Physik
Technische Universität Wien

*eingereicht an der Technischen Universität Wien
Technisch-Naturwissenschaftliche Fakultät*

von

Sameena Shah Zaman

Matrikelnummer. 0825624

Wiedner Hauptstr. 8-10, 1040 Wien

Vienna, October 31, 2011

Abstract

Fe on Cu(100) is a system which has been extensively studied over the last decades due to its complex and rich variety of structures and magnetic properties as well as for providing a prototypical system for magnetic ultrathin films. For 2-4 ML Fe grows as strained bcc with nano-martensitic structure, for 5-10 ML it grows as fcc (paramagnetic) film at room temperature with rare needle shaped bcc crystallites. Below room temperature, a (2×1) or $(2 \times 2)p4g$ reconstruction occurs with the so called ‘magnetic live layer’ and for thickness more than 10 ML, it grows as relaxed bcc. It has been shown that with Ar^+ ion irradiation, 8 ML Fe film undergoes a structural change from fcc to bcc. This change was confirmed by scanning tunneling microscopy (STM) and low energy electron diffraction (LEED). A “Thermal Spike” model was proposed for the transformation process and writing a magnetic pattern was demonstrated by ion-beam projection lithography.

In the current thesis, STM experiments will be presented, providing more insight into the surface magneto-optical Kerr effect (SMOKE) data previously presented by Rupp et al. for 8 ML Fe films with different ions. Best transformation results were obtained for heavier ions for all ion energies. Also the fcc-bcc transformation of 8 ML Fe film through a Au layer by Ar^+ ion irradiation was investigated using STM.

Films with thickness ≤ 2 nm are too thin for some applications like magnetic flux guides, therefore thicker films are desirable. Thus, one aim of the present work is to show that we can extend the above mentioned work to thicker Fe films provided we use some additional material to support them. For this purpose we have used CO pressure during growth to stabilize the Fe film as previously suggested by Kirilyuk et al. Then Ar^+ ion irradiation is used to induce a structural change in a 4 nm (22 ML) thick Fe film from fcc to bcc grown in CO pressure. Oxygen and carbon together contribute to the surface and bulk stability of fcc Fe phase respectively. STM images show the nucleation of bcc crystals which increase with the Ar^+ ion dose and eventually result in complete transformation of the film from fcc to bcc. Intermixing with the Cu substrate impedes the transformation. The best transformation results are obtained for 2 keV Ar^+ energy. LEED also shows the transformed patterns. For the magnetic properties, SMOKE measurements confirm the transformation from paramagnetic to strongly ferromagnetic with an in-plane easy axis.

We were also successful in stabilizing even thicker metastable fcc Fe films. The growth

technique used for stabilizing 8 nm (44 ML) thick fcc Fe film is co-evaporation of Fe and Invar ($\text{Fe}_{64}\text{Ni}_{36}$). The structural analysis was carried out using STM. The main factor affecting the stability limit of these thick fcc Fe films was found to be the concentration of Ni in the films. The most suitable Ni-concentration for stable fcc Fe films was found to be close to 15.1%.

We have employed the technique of the ion-induced transformation to write small ferromagnetic patches by Ar^+ irradiation through a gold coated SiN mask with regularly arranged 80-nm diameter holes, which was placed on top of the as-prepared fcc Fe films. Nanopatterning was performed on both 8-monolayer (ML) Fe films grown in ultrahigh vacuum as well as 22-ML films stabilized by dosing carbon monoxide during growth. The structural transformation of these nano-patterned films was investigated using STM. In both 8 and 22-ML fcc Fe films, the bcc needles are found to protrude laterally out of the irradiated part of the sample, limiting the resolution of the technique to a few 10 nm. The magnetic behavior of the transformation areas was confirmed by magnetic force microscopy.



(In the name of Allah the most merciful, the most beneficent)

Acknowledgements

I would like to express my gratitude to my Ph.D. supervisor, ***Prof.Dr. Peter Varga*** for giving me the opportunity to work in his group. His constant attention, encouragement and careful guidance have made the appearance of this thesis possible. I am also very thankful to ***Prof.Dr. Michael Schmid*** for his continuous support, expert advices and help. Although I had limited interaction with ***Prof.Dr. Ulrike Diebold***, nevertheless I am grateful to her for suggestions about my work and for sharing inspiring words about attitude in life.

I owe valuable assistance to a dedicated colleague *Andreas Buchsbaum* who introduced me to the experimental setup and who was a very attentive and patient instructor during that time. I want to acknowledge the help from **all my colleagues** in *I.A.P* (Institut für Angewandte Physik) group, especially *Philipp Scheiber* whose ever ready help with translation of german texts was very beneficial and also with proof reading my thesis despite his busy schedule. I would like to say many thanks to all of you for providing a joyous and friendly working environment and my very best wishes for everything you do in future.

I am highly indebted to ***HEC*** (Higher Education Commission) ***Pakistan*** for their uninterrupted financial assistance during my stay in Austria.

Last but not the least, I want to thank ***my parents*** and my siblings for their love, encouragement and support that gave me strength through out the cumbersome research period.

If not for the above mentioned people my Dissertation would never have been completed successfully.

Contents

Contents	iv
1 Introduction	1
1.1 Background and Previous Investigations	1
1.2 Outline of Our Work	3
2 Basics	6
2.1 Nucleation and Growth Modes	6
2.2 Magnetism	10
2.2.1 Diamagnetism	10
2.2.2 Paramagnetism	11
2.2.3 Ferromagnetism	13
2.2.4 Magnetic Anisotropy	14
2.2.5 Superparamagnetism	14
2.2.6 Magnetic Domains	16
2.3 Ion-surface Interaction	17
2.3.1 Channeling	19
2.3.2 Sputtering	20
2.3.3 Intermixing	20
2.3.4 Intermixing in thermal spike phase	21

2.3.5	The Stopping and Range of Ions in Matter (SRIM code)	23
3	Techniques	25
3.1	Measurement Techniques	25
3.1.1	Scanning Tunneling Microscopy (STM)	25
3.1.2	Low-Energy Electron Diffraction (LEED)	30
3.1.3	Auger Electron Spectroscopy (AES)	32
3.2	Surface magneto-optic effect	33
3.2.1	Kerr Effect	34
4	Experimental setup	37
4.1	UHV system	37
4.2	Experimental set-up	37
4.2.1	The RT-STM (Room Temperature Scanning Tunneling Microscopy) system	38
4.2.2	The setup for ion irradiation through a mask	39
4.2.3	The SMOKE setup (Surface Magneto-Optical Kerr Effect)	41
4.2.4	Sample preparation	42
4.2.5	Ion current measurement and neutralization problems	43
5	8 ML Fe films on Cu(100)	44
5.1	Introduction	44
5.2	SMOKE measurements	44
5.3	STM measurements	49
5.4	Discussion	54
5.4.1	Au coated 8-ML Fe films	58
6	CO-stabilized 22 ML Fe films on Cu(100)	63
6.1	Introduction	63

6.2	Film growth and stability factors	63
6.3	Surface morphology of 22 ML fcc Fe films	65
6.4	oxygen removal	70
6.5	Ion beam induced Transformation	71
6.5.1	STM	71
6.6	LEED	77
6.7	SMOKE	77
6.8	Mechanism of the Ion-Induced Transformation	80
6.9	22 ML Fe film coated by Pd and Au	83
7	44 ML $\text{Fe}_x\text{Ni}_{1-x}$ films on Cu(100)	87
7.1	Introduction	87
7.2	Film Growth and Properties of 44 ML fcc Fe film	87
7.3	STM measurements	89
7.4	Ion beam induced Transformation	90
7.5	Discussion	93
8	Nanopatterning by irradiation through a mask	95
8.1	Introduction	95
8.2	Results	96
8.2.1	8 ML fcc Fe film	96
8.2.2	22 ML fcc Fe film	99
8.3	Discussion	100
8.4	Magnetic Force Microscopy	101
9	Conclusion	104
9.1	Conclusion	104
	List of Figures	106

Bibliography**112**

Chapter 1

Introduction

1.1 Background and Previous Investigations

The emergence of scanning probe microscopies and nanotechnology in the 1980's opened new doors for scientists to investigate the material at small scale; so much so that matter at nano-meter scale was possible to be investigated. Since then technological advancement is progressing to improve our ability to produce and understand structures in that dimension and finally manipulate it for different applications. Tremendous efforts are being carried out to develop and establish this field.

Magnetic properties of various nano-scale systems have wide range of applications in recent as well as in future technology for developing high performance products. As memory storage devices for computers, these systems earn lot of attention with, of course a parallel desire for miniaturization. Most of the applications range from nano-patterned storage media [1–4] (requiring hard-magnetic materials) to magnetic flux guides (soft magnetic, e.g., flux concentrators for magnetic-field sensors) [5].

Focussing on the Fe/Cu(100) system which is one of the most frequently investigated system for the last decades, the phase diagram shows that the bulk Fe exists in the α phase [body-centered-cubic (bcc); ferromagnetic] at room temperature and above 1180 K, it attains the γ phase [face-centered cubic (fcc); paramagnetic] [6, 7] (Fig. 1.1). In 1967, Jesser and Matthews found out that metastable fcc Fe could be grown pseudomorphically on Cu(100) [8]. This discovery led to many possibilities of exploring this system through different techniques. It was found out that Fe on Cu(100) shows surprising magnetic [9–27] and structural properties [16, 17, 23, 28–42] depending on the Fe layer thickness [18] and temperature [12, 18, 30, 43]. And as it is not yet completely understood; therefore it is still motivating many scientists to carry out further research on this interesting and promising

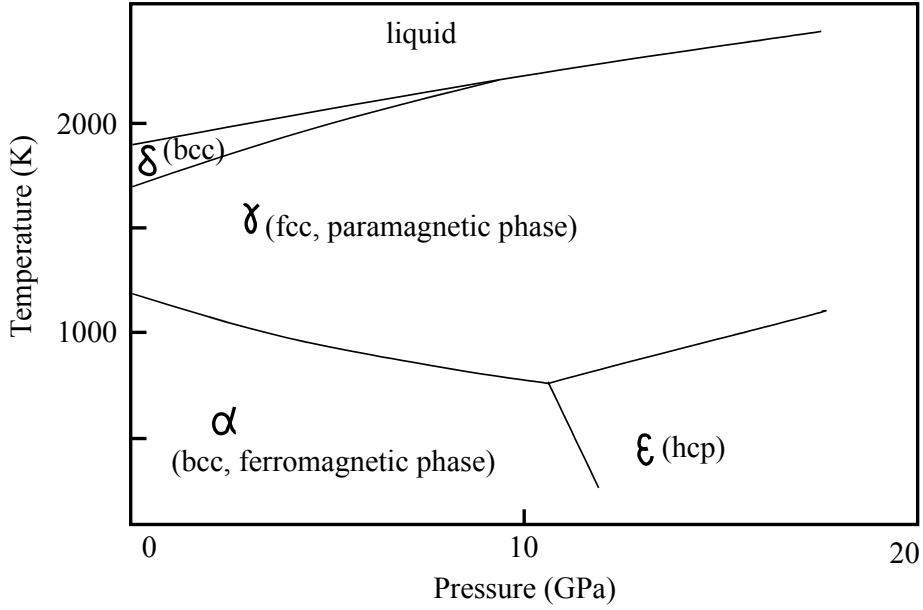


Figure 1.1: The Fe-Phase diagram [44–46].

system.

Early investigations show contradictory results for some aspects of this system, e.g., the critical thickness of the transformation from fcc to the bulklike bcc phase was reported to be 11 monolayer (ML) (Ref. [16]) and 17 ML (Ref. [17]). This contradictory issue could be resolved by considering different impurity levels in the films [47, 48]. This could be understood as a direct consequence of two different experimental set-ups (different residual gas pressure, impurities from setup etc). There was also confusion about the ground state of fcc Fe, which is usually considered antiferromagnetic [12, 49], while some researchers observed a ferromagnetic ground state for fcc Fe grown on Cu single crystal, especially for low thicknesses [11, 14, 50]. This controversy was successfully resolved by Biedermann et al. [7, 39, 51] using atomically resolved scanning tunneling microscopy (STM), which pinpoints the bcc-like nature of these films as the true source of ferromagnetism. For supporting experimental data, this system also triggered a plethora of theoretical investigations [40, 52–56]. Despite its partly controversial and scientifically rich history, the Fe-Cu system has emerged as an interesting prototype system for surface magnetism for academic research.

Taking a brief look at the structural and magnetic properties of this rich system gives us an idea about the complexities involved in this system. At room temperature, the structure and magnetic moment of the Fe film as a function of film thickness can be divided into the following three ranges [7, 16, 39], as shown in Fig. 1.2 [57]:

(1) Range-I, film thickness below 4 ML: Below 2 ML Fe, strong intermixing of Fe and Cu is observed. STM images show that already at 0.2 ML Fe, bcc-like distortions of Fe

clusters with only 3-4 surface atoms are present on the surface. Also groups of three atoms (which adhere to the fcc positions) are embedded in the substrate itself [7]. For 1.7 ML thick Fe film, significant reduction is observed in the Cu content on the Fe film surface. Above about 2 ML, Fe grows as strained bcc(110) lattice due to the fact that the atoms are adapting to the underlying fcc structure. STM images show a bcc-like phase which is sheared, periodically changing, shearing directions forming a zig-zig pattern. The sheared angle is found to be $\approx 14^\circ$. This structure is known as a nanomartensitic structure. These films are ferromagnetic with an out-of-plane easy axis [7, 16, 39, 58]. However, the upper limit of this range depends slightly on the hydrogen coverage [58].

(2) Range-II, film thickness 5-10 ML: In this range, pseudomorphic growth of Fe is observed on Cu(100) with fcc structure at room temperature. Cooling of these films to 80 K results in an area covered by a bcc-like surface layer, with STM revealing a (2×1) or $(2 \times 2)p4g$ reconstruction, called as the "magnetic live layer" at the top [16, 51, 59–61]. A few strained bcc "needles" may also be found at room temperature, while most of the film is still nonmagnetic [62].

(3) Range-III, film thickness above 10 ML: Above ≈ 10 ML, the film grows with a relaxed bcc(110) structure and is ferromagnetic with an in-plane easy axis [63].

1.2 Outline of Our Work

Rupp et al. has already shown that the fcc-to-bcc (and, hence, paramagnetic-to-ferromagnetic) transformation of the range-II films can be induced by Ar^+ ion irradiation for 8-ML films grown in UHV [64]. Surface magneto optic Kerr effect (SMOKE) studies were carried out, and it was established that this could be a potential system for creating ferromagnetic nano-structures [64].

Chapter 5 discusses in detail the structural (STM) and magnetic (SMOKE) [conducted by Rupp et al. [57]] evolution of 8 ML fcc Fe film irradiated with different ions at different ion energies. Also an attempt is made to observe the fcc-bcc transformation through a Au coated 8 ML Fe film using STM.

The study of the thicker films on this Fe/Cu(100) system (where thicker films above 10 ML, only grow as bcc) is an interesting enough motivation in itself and is helpful in improving our understanding of this complex system. Also, for some applications like in flux guides, films thinner than 2 nm are not suitable, therefore thicker films are desirable. Therefore, the presented thesis is an extension of the work described in [64].

Chapter 6 presents a technique for stabilizing thicker fcc Fe films as proposed by Kirilyuk et al. [47, 48]. We used CO as a stabilizing agent for our 22 ML fcc Fe films; CO dissociates into carbon and oxygen, contributing to the bulk and surface stability of the fcc Fe film, respectively [47, 48]. We present a detailed study of the ion-induced transformation of these

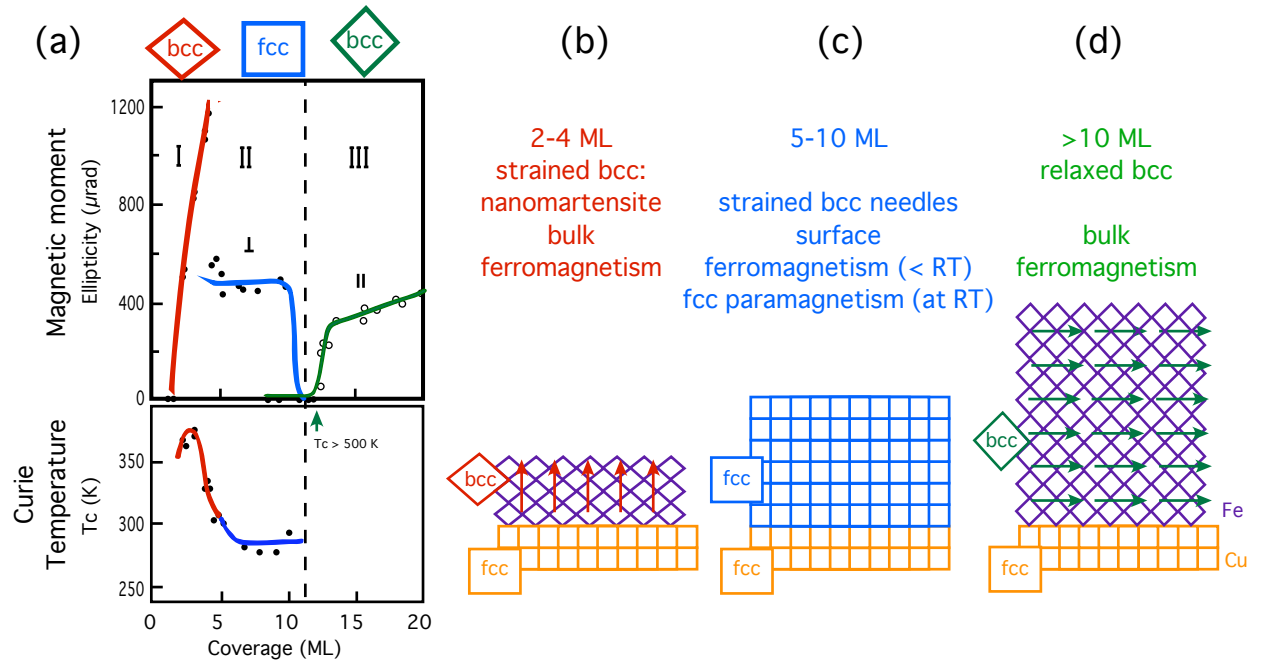


Figure 1.2: correlation between the structural and magnetic properties of Fe as a function of film thickness (a) magnetic moment and curie temperature as a function of Fe film thickness [16], (b) bulk ferromagnetism is observed with strained bcc having nanomartensitic structure [7, 16, 39, 58], (c) at RT; films are paramagnetic with fcc and below RT; surface magnetism is observed [16, 51, 59–62] (d) above 10 ML, films show bulk ferromagnetism with relaxed bcc phase [63].

films (by STM, AES and LEED), including magnetic measurements by SMOKE [65].

In chapter 7, the stabilization and structure of even thicker fcc Fe films i.e. 44 ML is presented. These films were stabilized by alloying small amounts of fcc metal Ni. This was realized by co-evaporation of Fe and Invar on Cu(100), and investigated by STM. We also highlighted the factors limiting the thickness of the fcc Fe films and transformation.

In chapter 8, we present ion nano-patterning of these films (i.e. 8 ML and 22 ML fcc films) using a mask, which is an easy-to-handle and a cost-effective experimental method for any UHV system. In these studies, we explore the feasibility of this method for nano patterning and the spatial resolution that can be obtained with this method.

All the experiments presented in this thesis were conducted in ultra high vacuum at room temperature.

Chapter 2

Basics

This chapter provides an explanation of the basic terminologies which are used in the upcoming chapters. We begin by describing the growth modes of nano-particles on the substrate surface, followed by magnetism section and ion-surface interactions.

2.1 Nucleation and Growth Modes

The morphology and structure of the film on a substrate depends on a number of processes involved during the film growth. The figure 2.1 illustrates some of the common processes carried out during thin film growth on the substrate surface. Being a non-equilibrium phenomenon, kinetics and thermodynamics of the system play an important role in the thin film growth. During film growth, evaporated atoms continuously diffuse on the surface, interact with each other (resulting in 2D and 3D islands), attach to step edges/ kinks and also some atoms may re-evaporate from the surface. These interactions between atoms determine the morphology and properties of the film.

For better understanding, it is worthwhile to have a detailed view of these underlying principles which dictate the growth mode of the films. The condensation of the material from the gas phase on to the substrate surface is given by the following impinging rate equation [66]:

$$R = \frac{C_g p}{\sqrt{2\pi M k_B T}} \quad (2.1)$$

where

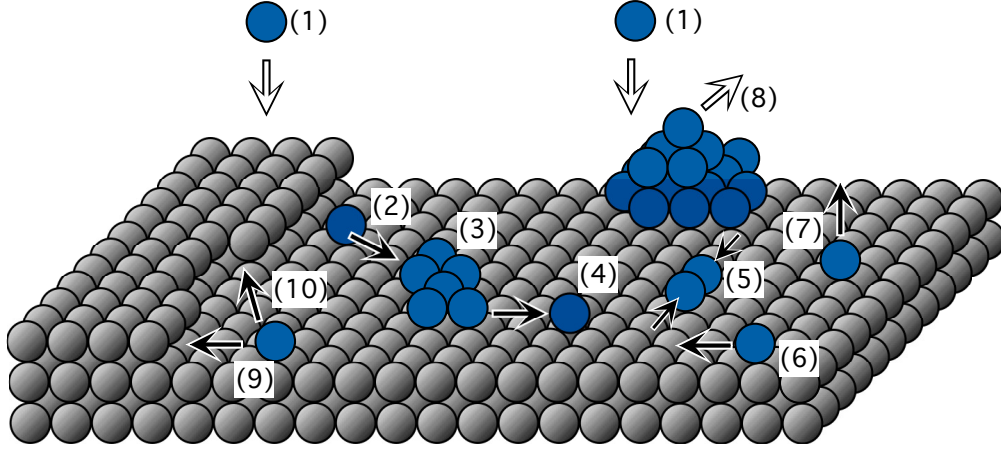


Figure 2.1: Schematic view of the processes occurring during film growth: (1) evaporated atoms, (2) atom diffusing to a cluster, (3) 2D cluster, (4) atom dissociating from the cluster, (5) cluster nucleation, (6) atom diffusing on the substrate surface, (7) atom re-evaporating from the surface, (8) re-evaporation from a 3D cluster, (9) atom diffusing to step edge or (10) to kink.

R : rate of the particles arriving at the substrate surface (number of particles per cm^2 per second)

C_g : geometrical shape factor

p : gas vapor pressure

M : molecular weight of the gas particles

k_B : Boltzmann constant

T : the temperature of the source

The condensed particles (or atoms) might diffuse along the substrate surface or might re-evaporate immediately back into the gas phase. The particles diffusing on the surface or adatoms might result in the adsorption of particles at special sites like the edges or defects or they might re-evaporate too. The mean square distance $\langle x^2 \rangle$ covered by the diffusing particles or atoms during the time t is given by:

$$\langle x^2 \rangle = 2a_o^2 \nu t e^{-\frac{E_{ac}}{k_B T_s}} \quad (2.2)$$

where

a_o : jump length

ν : vibrational frequency ($\approx 10^{13} \text{ s}^{-1}$)

E_{ac} : activation energy for diffusion

k_B : Boltzmann constant

T_s : the temperature of the substrate

From Eq. 2.2, one can see that the desorption rate is low for the low substrate temperature. For high substrate temperatures, the adatoms might diffuse into the bulk of the substrate depending on the miscibility between substrate and evaporated material at that particular temperature. The adatoms that do not desorb or diffuse can eventually end up forming nucleation points and grow into an island. The nucleation can be either of the following two types:

a) Heterogeneous nucleation: In surfaces having high step/defect density, growth occurs at the step edges or at the surface defect sites called heterogeneous nucleation. b) Homogeneous nucleation: In this case, nucleation starts randomly on the surface, i.e., the adatoms keep diffusing on the surface until they form small clusters with other diffusing adatoms, and keep on increasing in size by incorporating more adatoms. These clusters consisting of few adatoms can dissociate back to individual atoms until they attain a stable size called the "critical nucleation size". The critical size depends on the binding energies of the islands, substrate temperature and the desorption rate of the adatoms.

Generally, taking into consideration the higher coverages i.e. more than a sub-monolayer, the growth process of an evaporated material can be divided into the following three modes [67]:

1. The 2-D growth mode: Frank-van der Merwe growth mode (FM), it is also known as the layer-by-layer growth. In this growth mode the film grows on the surface of the substrate by forming consecutive closed layers. There is a stronger interaction between the substrate and the layer atoms than between the atoms in a layer [68].
2. The 2 and 3-D growth mode: Stransky-Krastanov growth mode (SK), it is also known as the layer-plus island growth mode. After forming few complete layers, 3-D island formation occurs on top of layers. Factors responsible for this growth mode could be the symmetry or orientation of the film with respect to the substrate. If the lattice parameter of the film is different from that of the substrate then also the resulting film grows in SK mode [69]. After the evaporation of several layers, at one point the strain inside the layers become too large to allow homogeneous layer growth. Therefore, the strain and surface tension might result in small islands.
3. The 3-D growth mode: Volmer-Weber growth mode (VW), it is also known as the island growth mode. In this case, 3-D islands are formed with no closed layers. The interaction between the neighboring atoms in a layer is stronger than the interaction between the film material and substrate [70].

A simple general distinction between different growth modes can be made on the basis of the surface or interface tension γ i.e. the free energy (per unit area) to create an additional

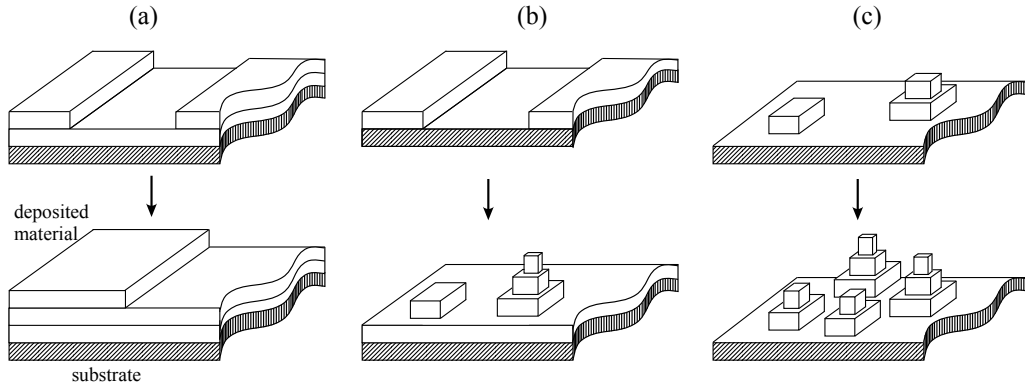


Figure 2.2: (a) Schematic view of the three growth modes: (a) Frank-van der Merwe growth mode (FM), (b) Stransky-Krastanov growth mode (SK) (c) Volmer-Weber growth mode (VW)

piece of surface of interface. As γ is also the force per unit length, the force equilibrium at a point where the substrate and a 3D island of the evaporated film touch require the following equation :

$$\gamma_S = \gamma_{SF} + \gamma_F \cos \phi \quad (2.3)$$

where

γ_S : surface tension between substrate and vacuum interface

γ_{SF} : surface tension between substrate and film interface

γ_F : surface tension between vacuum and film interface

ϕ : contact angle

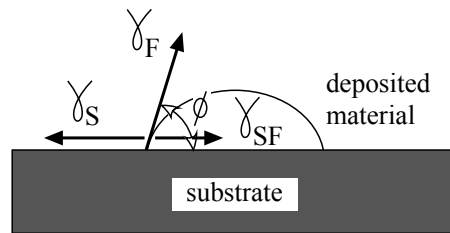


Figure 2.3: simplified view of the deposited material on the substrate surface, where γ_S , γ_{SF} and γ_F are the surface tension between substrate and vacuum interface, substrate and film interface, and between vacuum and film interface respectively.

Depending on the value of angle ϕ , different growth modes can be distinguished as following:

$\gamma_S \geq \gamma_{SF} + \gamma_F$, $\phi = 0$	FM growth mode
$\gamma_S < \gamma_{SF} + \gamma_F$, $\phi > 0$	VW growth mode
$\gamma_S > \gamma_{SF} + \gamma_F$, $\phi > 0$ plus strain	SK growth mode

The SK mode can be easily explained on the basis of change in the value of γ_S , γ_{SF} or γ_F with increasing amount of deposited material, which may be due to the structural changes or due to difference in lattice parameters. For Fe/Cu(100) system, the lattice constants of Cu and Fe are 3.62, 3.57 (fcc Fe) and 2.86 (bcc Fe) Å respectively. As the lattice mismatch is $< 2\%$, therefore, epitaxy results in SK growth mode. The Fe film grows as fcc on Cu(100) due to strain which increases with the thickness. Therefore,

$\gamma_{Cu} > \gamma_{Cu-Fe}$, $\phi > 0$ plus strain	SK growth mode
---	----------------

After the first layer the term γ_F could be neglected as the Fe is deposited on the already deposited Fe layers.

2.2 Magnetism

When the matter is placed in the magnetic field, different types of magnetic properties are observed depending on the type of interaction with the magnetic field. As part of this thesis addresses magnetic properties of Fe films, we therefore discuss a few magnetic terms which are relevant to the results presented in the later chapters. More details can be found in literature [71–73].

2.2.1 Diamagnetism

The magnetization of materials can have two possible sources; one from orbital motion of electrons and the other from the spin motion of the electrons. Diamagnetic materials have no magnetization in the zero field. When this material is placed in the magnetic field, the applied magnetic field effects the motion of the moving electrons in such a way that it produces a magnetic moment opposing that of the applied magnetic field. The origin for this magnetization is an orbital motion of electrons about the nuclei of the atom, which is electromagnetically induced by the applied magnetic field. This is the same as the Lenz's law; the induced current produces a magnetic flux that opposes any change in the applied field, which causes the material to be slightly repelled by the magnetic field. The magnetic response of a material is quantified by magnetic susceptibility χ (i.e. the ratio

of magnetization M to magnetic field H : ($H = \chi M$), which is found to be negative for diamagnetic materials and usual order of magnitude is about 10^{-5} , as shown in Fig. 2.4 (a).

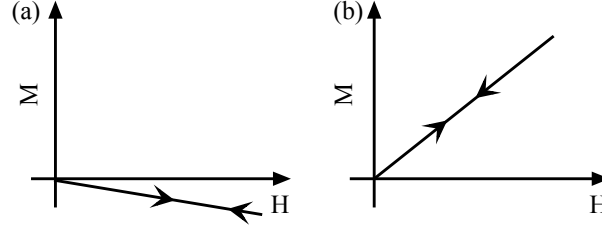


Figure 2.4: Magnetization versus applied magnetic field, (a) diamagnetic system and (b) a paramagnetic system. The arrow show the direction of increasing and decreasing applied magnetic field.

2.2.2 Paramagnetism

Paramagnetism is a kind of magnetism which generally occurs in elements or compounds possessing unpaired electrons. The magnetization is found to be proportional to the applied magnetic field shown in Fig. 2.4(b). If the field is extremely strong, however, the magnetic moments are strictly oriented in the direction of applied field until magnetic saturation is reached. For a constant applied field, an increase in the temperature T means an increase in the disorientation of the magnetic spins due to thermal motion and a decrease in magnetic susceptibility. The magnetic susceptibility is positive with order of magnitude between 10^{-3} and 10^{-5} . The Langevin theory of paramagnetism treats the paramagnetic substance as a classical (non-quantum-mechanical), collection of permanent magnetic dipoles with no interactions between them. When an external magnetic field is applied to the paramagnet, each magnetic dipole experiences a torque. The potential energy associated with the force that produces this torque is given by:

$$U = -\mu H \cos \theta \quad (2.4)$$

where μ is defined as the magnetic moment of the dipole in the applied magnetic field H , and θ ; the angle between μ and the direction of H . In the absence of thermal agitation each magnetic dipole orients in such a way that the potential energy is minimized i.e., orient parallel to the magnetic field. With all the dipoles lined up, the magnetization is given as:

$$M = N\mu \quad (2.5)$$

N is the number of dipoles per unit volume. The direction of the magnetization would be that of the applied field. In this case a small magnetic field will cause all the dipoles to line up so that the susceptibility would be infinite. But actually, there is thermal agitation which in part offsets the aligning tendency of the magnetic field. The Langevin theory takes this into account and predicts the paramagnetic susceptibility as a function of temperature. In the presence of thermal agitation, the magnetic dipoles are not fully lined up in the direction of the magnetic field, but there is some distribution of angles made with the field. Thus the magnetization is:

$$M = N\mu \cos \theta \quad (2.6)$$

where $\cos \theta$ is the average value of the cosine of the angle between dipole and field. The average is taken over the distribution of dipoles in thermal equilibrium. Statistically, this average is given by Eq. 2.7 ,

$$\cos \theta = \frac{\int e^{-\frac{U}{kT}} \cos \theta d\Omega}{\int e^{-\frac{U}{kT}} d\Omega} \quad (2.7)$$

where $d\Omega$ is the solid angle and $e^{-U/kT}$ is the Boltzmann distribution in the dipole energy in Eq. 2.4 at angle θ with respect to the applied field at absolute temperature T . Solving the integrations result in $L(a)$; the Langevin function of $a = \mu H/kT$. Therefore, Eq. 2.6 is written as:

$$M = N\mu L(a) \quad (2.8)$$

For $a \ll 1$ i.e. $\mu H \ll kT$, then the Langevin function $L(a)$ can be replaced with $a/3$. Eq. 2.8 can be approximated as [72]:

$$M \simeq \frac{N\mu^2}{3kT} \quad (2.9)$$

This is a good approximation except at low temperatures or at extremely high applied fields. The susceptibility χ is derived as [72, 74]:

$$\chi = \frac{M}{H} = \frac{N\mu^2}{3kT} = \frac{C}{T} \quad (2.10)$$

This is known as Curie's law. There are some paramagnetic solids which obey the Curie-Weiss law $\chi = C/(T - \Theta)$ in a certain temperature range, where Θ is the Curie temperature. The modification is due to the effective interactions between the dipoles which were neglected in the preceding development or distortion may be responsible for it.

Eq. 2.10 can also be derived quantum mechanically, taking into account the space quantization of the moment [72, 73].

2.2.3 Ferromagnetism

Ferromagnetism (FM) is a property exhibited by materials having long-range ordering which causes the unpaired electron spins to line up parallel to each other in a region called a magnetic domain. Once a ferromagnetic material is magnetized, it will tend to stay in the magnetized state to some extent even after the removal of applied field. This tendency to "remember the magnetic history" is called hysteresis shown in Fig. 2.5. The fraction of the saturation magnetization which is retained when the driving field is removed is called the 'remanence' of the material, and is an important property of permanent magnets. The value of field required to reduce the magnetization to zero after reaching the saturation, is called 'coercive field' or 'coercivity'. Ferromagnets have high magnetic susceptibilities (\approx between 10^3 and 10^5), and for a given ferromagnetic material, the long range order abruptly disappears at a certain temperature. This temperature is known as the Curie temperature for that material. Typically, the Curie temperature of iron is about 1043 K.

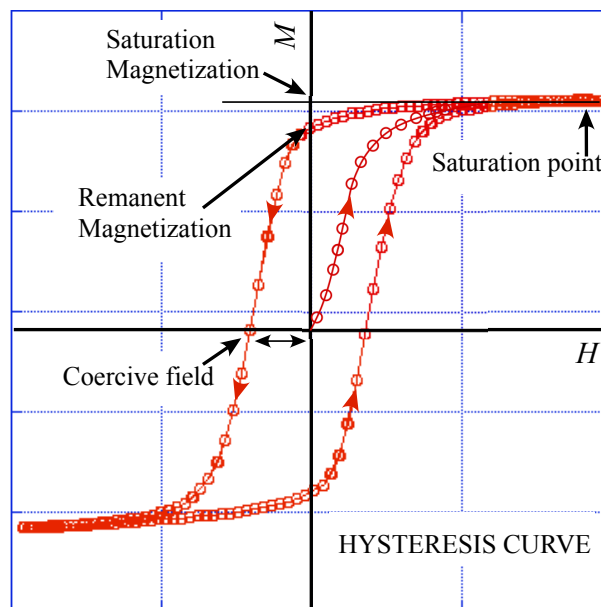


Figure 2.5: Hysteresis loop of a ferromagnetic material.

2.2.4 Magnetic Anisotropy

The magnetic properties of the materials depend on the direction in which they are measured. This dependence on the crystallographic directions is known as Magnetic Anisotropy. There are several kinds of anisotropies; crystal (magnetocrystalline) anisotropy, shape anisotropy and stress anisotropy to name a few. Crystal anisotropy is intrinsically associated with the crystal whereas all other anisotropies are extrinsic or induced to the material.

For a body-centered-cubic Fe (cubic crystal), external magnetic field can be applied along different crystallographic directions, i.e. $\langle 100 \rangle$, $\langle 110 \rangle$ or $\langle 111 \rangle$. It has been found experimentally that it can be easily magnetized in $\langle 100 \rangle$ direction than in the other two directions. It means that the *domain walls* separating two *domains* (see section: 2.2.6) can be easily moved by applying a small magnetic field (order of a few tens of oersteds) in $\langle 100 \rangle$ direction [73]. Therefore, $\langle 100 \rangle$ is the easy direction, it means that this is the lowest energy state of the magnetic moments. Magnetizing material in directions other than easy direction, requires some work against the anisotropy force to turn/rotate the magnetic moment vector away from an easy direction. Therefore, some energy must be stored in the crystal in points in a noneasy direction. This energy term is called as magnetic anisotropy energy. In general, most kinds of magnetic anisotropy like magnetostrictive anisotropy (related to mechanical stress) in the system and volume anisotropy (or surface/interface) may also contribute to the net energy [73].

For thicker fcc Fe films presented in this thesis, the films when transform to bcc crystallites may have magnetocrystalline as well as shape anisotropy associated with their wavy shape.

2.2.5 Superparamagnetism

When the particles are small enough, the ferro or antiferromagnetic materials exhibit behaviour similar to paramagnetism even if the temperatures are below Curie temperature T_C (ferromagnetic nanoparticles) or Néel temperature T_N (antiferromagnetic nanoparticles). This effect is called superparamagnetism (SPM), at which the thermal energy is not sufficient to overcome the coupling forces between neighboring atoms, but is sufficient to change the direction of magnetization of the entire crystallite. The resulting fluctuations in the direction of magnetization cause the magnetic field to average out as zero. Thus the material behaves like a paramagnetic material with the magnetic moment of the entire crystallite tending to align in the direction of the magnetic field. This special behaviour occurs in nanoparticles which are single domain, i.e., single magnetic domain, with typical sizes between 3-50 nm (depending on material), time, temperature and anisotropy.

Fig. 2.6 shows a single domain nanoparticle with uniaxial anisotropy, where the magnetic moment prefers to be oriented along the major axis of particle, either up or down, commonly

known as the "easy axis" of the nanoparticle. Therefore, the magnetic moment can turn from the position $\theta = 0^\circ$ to 180° , only if it has an energy equal to or greater than the energy of the 'anisotropy barrier' i.e. equal to KV . If $KV \ll k_B T$, the magnetic moment fluctuates isotropically in space. And if $KV \gg k_B T$, the magnetic moment cannot switch and when a field is applied the energy can be given by [73]:

$$E(\theta) = -\mu \cdot B - KV \cos^2 \theta \quad (2.11)$$

The mean time between the two flips is given by Neel Arrhenius equation [75]:

$$t_N = t_0 e^{-\frac{KV}{k_B T}} \quad (2.12)$$

where

t_N : average time for the magnetic moment to randomly flip under thermal fluctuations

t_0 : attempt time(period); length of time, characteristic of material, typically 10^{-9} to 10^{-10} sec

K : magnetic anisotropy, V : volume,

KV : energy barrier; it is the energy required to switch the magnetization

k_B : Boltzman constant, T : temperature

Therefore, t_N can vary from few nanoseconds to years. For a given temperature and particle shape, t_N changes from less than a second to several years, when volume V changes by relatively small amount [76]. Let t_m be the magnetisation measurement time of a single SPM nanoparticle, then if $t_m \gg t_N$, the magnetic moment flips several times and averages out to be zero: Thus, SPM occurs. If $t_m \ll t_N$, magnetic moment does not flip and is ferromagnetic. Thus, the state of nanoparticle depends on measurement time. And when $t_m = t_N$, the SPM \leftrightarrow FM transition occurs. The temperature for which $t_m = t_N$, is called Blocking temperature T_B .

This phenomenon is observed at a small length-scale, where the energy required to change the direction of the magnetic moment of a particle is comparable to the ambient thermal energy. Therefore, at this point, the rate of change of direction of particle plays an important role. In several experiments: t_m is kept constant, temperature is varied to see the transition between SPM and FM as function of temperature.

Superparamagnetism limits the storage density of hard disk drives called "superparamagnetic limit". When the areal density reaches 150 Gbits/in^2 , the magnetic energy holding the bits in place on the medium becomes equal to the thermal energy within the disk drive itself. When this happens, the bits can "flip", scrambling the data.

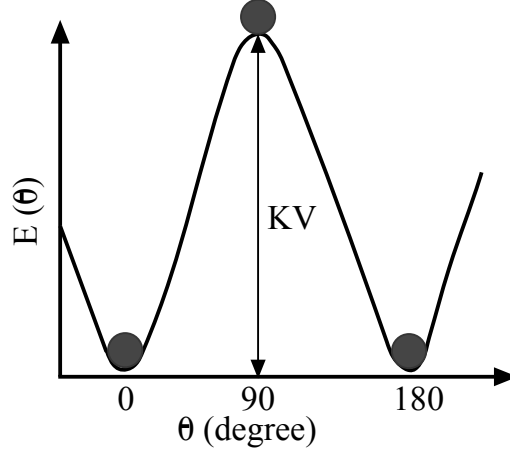


Figure 2.6: Energy as a function of angle for single domain particle

2.2.6 Magnetic Domains

The magnetic domains are a result of energy minimization. To reduce the total magnetic energy E , FM material forms domains of a certain size. Fig. 2.7 shows a single domain which reduces the external magnetic field by forming two domains, since the magnetic lines of force are shortened. On further subdivision, this field is further reduced. The size of domains is defined by minimization of the sum of the following free energy terms [73, 77]:

$$E = E_{ex} + E_A + E_Z \quad (2.13)$$

where

E_{ex} : Exchange anisotropy term arises from an exchange interaction between two magnetic systems at the interface.

E_A : anisotropy could be due to shape, stress, crystal symmetry (magnetocrystalline) etc.

E_Z : Zeeman energy arises due to the interaction between the magnetic material and an applied magnetic field.

The neighboring magnetic domains are linked by boundaries having certain width called domain wall width. It is energetically more favourable to gradually cant the magnetic moments over a region between two domains. Two opposing energies contribute to the width of the domain wall namely exchange energy E_{ex} and magnetocrystalline anisotropy energy. The anisotropy energy is minimum when magnetic moments are aligned parallel to the crystal axes (resulting in thin domain wall), and, exchange energy is minimum when magnetic moments are parallel to each other (resulting in thick domain wall). These two energies compete to get the final width of the domain wall in a material.

Two main types of spin structures inside the domain walls are known; Bloch wall (usually preferable in bulk) and Néel wall (favorable when the film thickness becomes smaller than the wall width). The spin structures of Bloch and Néel walls are shown in Fig. 2.8. For Bloch wall, the spins rotate in a plane parallel to the wall plane whereas, for Néel wall they are perpendicular [72, 74].

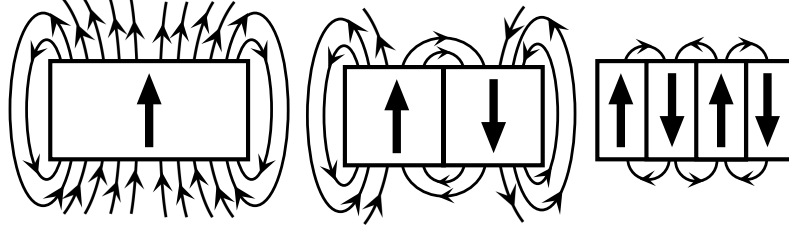


Figure 2.7: Magnetic field energy reduced by formation of domains [72, 74].

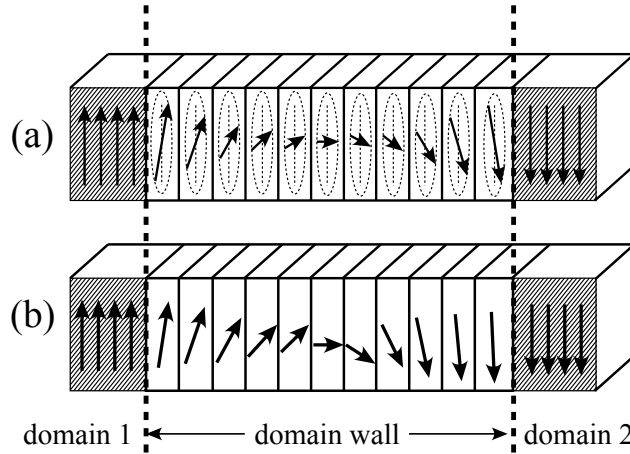


Figure 2.8: Types of domain walls (a) Bloch wall (b) Néel wall [72, 74].

2.3 Ion-surface Interaction

The bombardment of solids with ions having energy ranging from the eV-MeV range results in complex mechanisms of ion-surface interactions, producing a wide range of property changes in the solid. For better understanding, we would emphasize our discussion mainly on the factors concerning ion-induced phase transformation, as it is closely related to the presented work in this thesis. The schematic view of the ion-path in the Fig. 2.9 [57] shows sputtering of solid, ion-implantation and displacement which results in collision cascades.

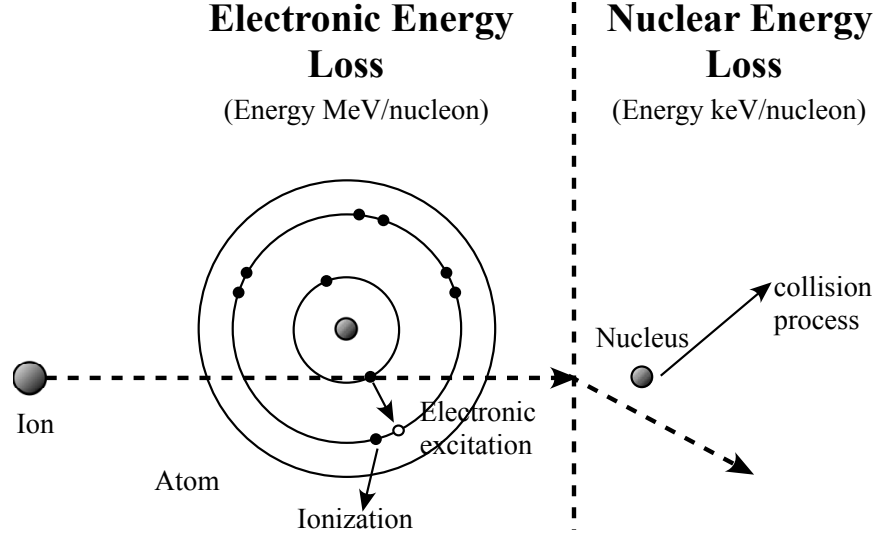


Figure 2.9: Schematic view of the ion-surface interaction: showing electronic and nuclear energy loss of an ion [57].

The energy loss dE (stopping power dE/dx) of an energetic particle traversing a distance dx across a solid can be divided into following two main mechanisms [78, 79]:

$$\frac{dE}{dx} = \frac{dE}{dx}|_e + \frac{dE}{dx}|_n \quad (2.14)$$

where e and n represent the electronic and nuclear collisions respectively.

The first term in Eq. 2.14, $dE/dx|_e$ (electronic energy loss) represents the inelastic collisions between the incoming ion and the electrons in the substrate and also electron-electron interactions. This leads to the ionization, excitation, electron exchange (or transfer) of atoms of the solid and excitation of electron in the ion etc. This can be seen as a quasi-continuous retarding process of the ion. In metals, these electronic losses are relaxed as heat, i.e. the ion energy loss is responsible for the formation of atomic dislocations. High-energy ions are an exception to this, as they induce direct structural changes in the solid known as the so-called Coulomb explosion.

The second term in Eq. 2.14, $dE/dx|_n$ represents the elastic collisions between the interacting particles, i.e. a recoil energy is transferred by the incoming ion to the substrate atom. Here, the ion is deflected which is in contrast to the electronic stopping. The atom leaves its original site if the recoil energy is greater than the threshold energy for displacement (for metals displacement energy ≈ 20 -40 eV). This results in the creation of a vacancy-interstitial or Frenkel pair [74]. And if the recoil energy is too large than the threshold energy for displacement, then the "primary knock-on atom" (PKA) displaces further. This

results in a collision cascade. The so formed collision cascade terminates only when the energy of the colliding atoms becomes lower than the displacement energy. The relative importance of various interactions between the incoming ion and the solid is mainly dictated by the velocity of the incoming ion, its charge and the type of the substrate atoms. However, for low energy ion bombardments, the electronic energy loss term is much higher than the nuclear.

Several atoms are displaced with an energy transfer per atom in the displacement energy range. After the collision phase is the “Thermal-Spike” phase. In the “Thermal-Spike” phase after a few pico seconds, an equilibrium state between the kinetic and potential energies of the disturbed lattice is attained. This is acquired by the energy transfer from the “Thermal-Spike” volume to the surrounding lattice, resulting in a large number of the displaced atoms (within few pico seconds) returning to their original lattice sites. This results in the formation of defects like small clusters of interstitial atoms or vacancies. These defects can get in contact with each other by thermal diffusion in the relaxation phase. Depending on the diffusion length and sample temperature, the point defects could be annealed whereas the cluster defects could grow into large area defect structures.

If the penetration range of the ion is comparable to the thickness of the multilayer system (different materials), then implantation could result in the intermixing across the interface surface.

In the collision phase the atoms are transported through the interface areas due to the nuclear collisions. This process is independent of the thermodynamic properties of materials and always leads to the intermixing the interface. The thermodynamical properties of materials are critical only in the “Thermal-Spike” phase (explained in the later section) during the transition phase from the quasi liquid to the solid state. This leads to the diffusion depending on the thermodynamic properties. For alloy materials, ten times larger intermixing is observed only by mixing in collision phase [57]. Another way for material transport through the interface can take place in the relaxation phase by thermal diffusion. In this case, the diffusion is pronounced due to continuous formation and recombination of vacancies in the interface surrounding.

In the work presented in this thesis, we are dealing with Fe films grown on Cu(100) which is an immiscible system. It is an established fact that at temperatures below 800 K, both metals have negligible solid solubility in equilibrium (equilibrium phase diagram [80]) due to large positive enthalpy of mixing of +19 kJ/mol [81–83].

2.3.1 Channeling

Due to the symmetries in a crystal, the ions can be scattered deep (thousands of Å) along the low index crystal directions by the electrostatic potentials of the atomic chains. This is called "Channeling". Channeling occurs when the interatomic distances are larger than

the size of shadowing cones of the surface atoms. The factor influencing the limits for the deviation of the entrance angle from an ideal symmetry is described by critical angle for channeling θ_c . This angle is given as $\theta_c \propto \sqrt{\frac{Z_1 Z_2}{Ed}}$ where Z_1 and Z_2 are the atomic numbers of the ion and target atom, E energy of ion, and d is the interatomic distance along the row. The ion moving along a channel does not undergo large angle scattering as it cannot get close enough to atomic nuclei. Therefore, small angle scattering results in oscillatory trajectories with hundreds of Å wavelength. Also these ions can lose energy by inelastic collisions with electrons in the channel [79].

2.3.2 Sputtering

Another process of ion-surface interaction is sputtering. When a high-energy ion impinges the solid surface, it dissipates kinetic energy with the solid atoms in a series of collisions and finally comes to rest. As a consequence, a number of atoms gain sufficient energy to cause displacements from their lattice sites and cause a recoil cascades within the solid. Some of these cascades may end up at the surface, imparting enough energy to the surface atoms which leave the surface as positive, negative or neutrals. Hence, bombarded by energetic ions results in the removal of the material from the solid. This process of removal of material from surface by ion impingement is known as *sputtering* shown in Fig. 2.10. Sputtering is characterized by the sputtering yield which is defined as the ratio of the number of sputtered atoms to impinging particle (ion). The sputter yields depend on the incident particle, structure and composition of target material and the experimental details like energy, angle of incidence [79].

It is worth pointing out that “thermal spike” is not the reason for sputtering with ions in keV energy range. Although this was believed in the early times of the thermal spike model [84, 85]. In the presented work, mostly the transformation of the Fe films from fcc-bcc phase is carried out at less than a monolayer of ion irradiation, which is lower than the dose required to carry out sputtering of the films. A decreasing trend in the magnetic signal is observed at above one monolayer which indicates sputtering of the films with ion irradiation (see section 6.7). But in the range in which the transformation is carried out, the ion dose value is low to cause any sputtering.

2.3.3 Intermixing

In our system, intermixing at the Fe-Cu interface may impede the fcc-bcc transformation of the Fe films. This is because Cu(100) at room temperature has fcc structure, and considerable fraction of Cu in the fcc Fe films would not facilitate the transformation to bcc phase. High Fe-Cu intermixing reduce the transformation efficiency of ions and consequently the magnetic property is also suppressed. Therefore, the energy of the ions

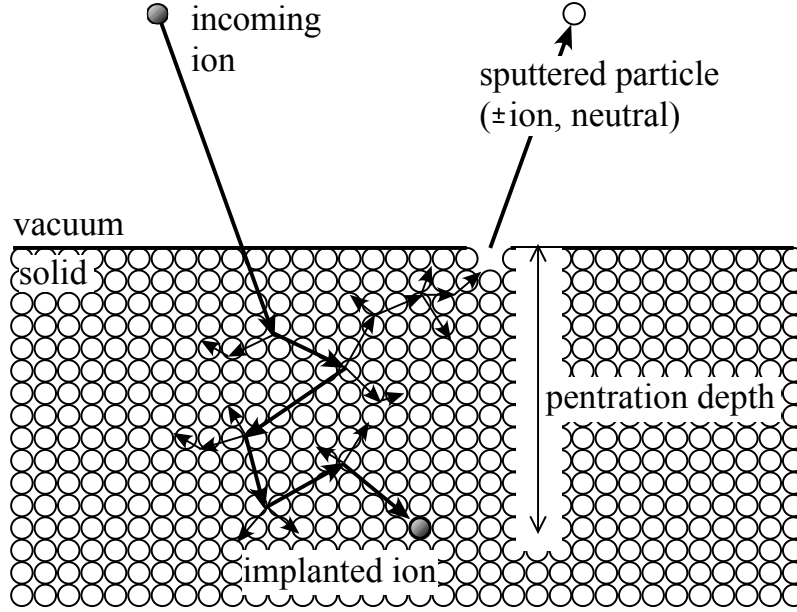


Figure 2.10: Ion-surface interaction: showing sputtering process.

used to carry out efficient transformation was selected so that the fraction of Cu atoms in the melt was negligible as compared to Fe atoms. This was carried out by SRIM (section 2.3.5).

2.3.4 Intermixing in thermal spike phase

Details of the intermixing in the thermal spike phase are presented below [86]. For target atoms $Z > 20$, the ballistic model does not hold well, therefore the *thermal spike model* replaces it to explain the ion beam induced collision cascade. In this work, the materials used are Fe (atomic number, $Z = 26$) and Cu ($Z = 29$) respectively. In *local thermal spikes*, the cascade ends up in the formation of locally separated collision cascades. In the *thermal spikes*, the material gets heated up to the extent that it forms a small molten volume in the material. According to this, if the chemical affinity between the material is high, then chemically driven diffusion processes are possible which lead to higher intermixing rates in comparison to the *ballistic intermixing*. Experimentally, it is seen that this process depends on the thermodynamical variables i.e. mixing enthalpy ΔH_m and the average binding enthalpy ΔH_b of the constituent elements.

ΔH_m is the enthalpy difference between the alloy (A-B atom) and the pure metals (A-A and B-B) or alloy (A-B). Therefore, this value allows to estimate the tendency to form an alloy. The Fe-Cu system is not miscible and at equilibrium has positive mixing enthalpy H_m

of 19 kJ/mol [87] and leads to low mixing rates than for miscible systems. The expression for the mixing rates k_t is given as [86]:

$$k_t = \frac{1}{2} c_1 \frac{Z^{1.77} E_{damage}}{N^{2/3} \Delta H_b^2} \left(1 + c_2 \frac{\Delta H_m}{\Delta H_b} \right) \quad (2.15)$$

where c_1 and c_2 are experimentally determined constants, $c_1 = 2.7 \times 10^{-7} \text{ nm}^3 \text{ keV}$ and $c_2 = 50$. Z and N stand for the average atomic number and average concentration of layer materials.

For heavy ions, *global thermal spike model* describes an overlap of the dense collision cascade that finally becomes a continuous, almost cylindrical spike along the ion path. Assuming the energy deposition of the ion takes place in a small area along the ion path which leads to the locally temperature rise. There the mixing rate is given by [88]:

$$k_g = \mu_1 \frac{E_{damage}^2}{N^{5/3} \Delta H_b^2} \left(1 + \mu_2 \frac{\Delta H_m}{\Delta H_b} \right) \quad (2.16)$$

The phenomenological constants μ_1 and μ_2 are experimentally determined. In *global thermal spike*, the intermixing rate is scaled with the square of the damage energy [86].

In literature, another model is based on molecular dynamics simulations (MDS) of surface defects due to the irradiation with charged particles, called as [89]. There the energy of the impinging ion is distributed homogeneously in a small volume. After a period of picoseconds, the volume is molten. According to the MDS for different systems (eg. Fe, Cu, Ni, Ag, Pd) the relation for the molten volume V_{molten} is given as [78, 90]:

$$V_{molten} \approx V_{atom} \times \frac{E_{nucl}}{14 k_B T_{melt}} \quad (2.17)$$

where V_{atom} is the atomic volume, E_{nucl} is the energy transferred to the target atom in nuclear collisions [calculated by SRIM (discussed in next section)], T_{melt} is the temperature of the melt and k_B is the Boltzmann constant. With this formula, one can estimate the number of atoms in the molten volume and hence estimate intermixing.

The pressure built up inside the melt increases, as the density of liquid in the melt is lower than the density of solid. If the molten volume has contact to the surface, the melt flows out of the surface, this is followed by fast quenching of the melt due to high thermal conductivity in metals. As the melt cools from out to the centre of the molten volume, it crystallizes in the structure of the surrounding solid. The outflow results in vacancy formation in the material, shown schematically in Fig. 2.11 [90].

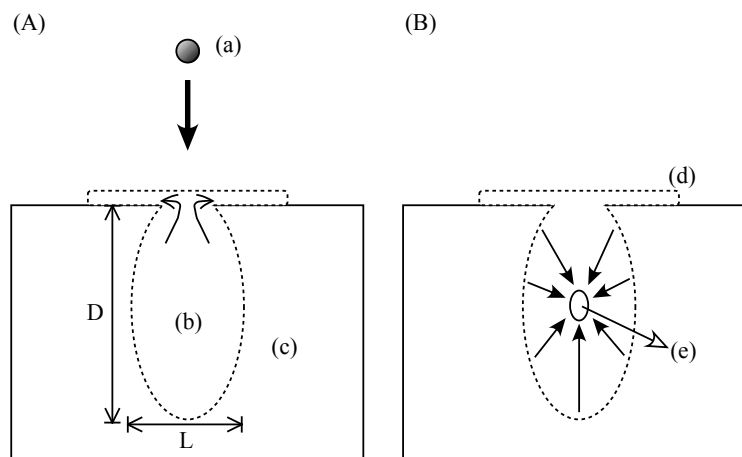


Figure 2.11: melt outflow model: (A) sketch of the ion-surface interaction showing (a) incoming ion, (b) molten volume, (c) solid substrate. Outflow of the material from the molten volume onto the surface is labelled by arrows. (B) After few picoseconds (d) atoms onto the surface form vacancy clusters, (e) the melt freezes out. The arrows pointing in the centre of molten volume show the direction of re-crystallization [90].

2.3.5 The Stopping and Range of Ions in Matter (SRIM code)

SRIM is a group of software programs which is based on the treatment of ion-atom collisions [91]. It can calculate the stopping and range of ions (up to 2 GeV/amu) in matter. The results of the simulation can be displayed as: atom recoil distribution, collision cascade and ion range etc to name a few. SRIM software accepts targets composed of compound materials. It can calculate the final 3D distribution of the ions and also takes into account all kinetics associated with the ion energy loss such as target damage, sputtering, ionization, and phonon production. The energy, angle and type of the incoming ion can be selected easily as per experimental requirement of the system. Hence, this software offers a flexible range of calculation depending on the specific need of the experiment. A detailed description for this simulation software can be found in [91].

We used this software to estimate the penetration depth of Ar^+ ions into the Fe films grown on the Cu substrate at room temperature. The Fe film thicknesses presented in this thesis are 8 (1.4 nm), 22 ML (4 nm) and 44 ML (8 nm). The Ar^+ ion energies used in the experimental work were between 500 eV and 5 keV. We also used it to give an estimation of the number of atoms (Fe or Cu) in the molten volume formed by “thermal spike”. This method can be elaborated as following: The energy transferred to the target atoms i.e. Fe or Cu atoms can be separately determined from the file, E2RECOIL.txt (this file can be

generated by requesting it from the active SRIM screen). Plugging in the corresponding values of constants and E_{nucl} in eq. 2.17 for Fe and Cu, gives an estimate of number of atoms (Fe or Cu) in the molten volume discussed in chapter 6.

Chapter 3

Techniques

3.1 Measurement Techniques

This chapter describes the details of the experimental techniques used to analyze the fcc \rightarrow bcc transformation of the 8, 22 and 44 ML fcc Fe Films.

3.1.1 Scanning Tunneling Microscopy (STM)

STM is one of the most powerful surface analysis tool. It was developed in the early eighties by G. Binnig and H. Rohrer at the IBM [92, 93], earning them a Nobel Prize in Physics in 1986 and enabling the world to image the topography and the electronic structure of a conductive surface in real space with atomic resolution.

It is based on the concept of quantum mechanical tunneling effect: when a fine metallic tip is brought in close proximity (a few Å) to a conductive sample, electrons from one conductor penetrate through a classically impenetrable potential barrier (in our case: vacuum) to another conductor, due to their wave-like nature. This barrier can be approximated by a one-dimensional rectangular potential and electrons can tunnel from the occupied states of one conductor into the unoccupied states of the other conductor at same energy resulting in an equilibrium state between surface and tip at no applied voltage. Generally, as the tip and sample are different materials with different work functions therefore, an electrical field also exists when no voltage is applied ($U = 0$) [94, 95]. The height of this barrier [Fig. 3.1(a)] can be approximated by:

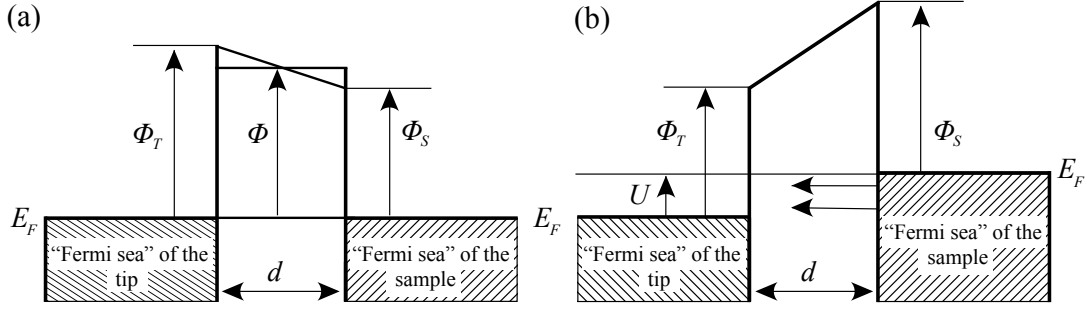


Figure 3.1: (a) One-dimensional rectangular potential barrier caused by different work functions of the tip (ϕ_T) and the sample (ϕ_S). The tunnel effect causes electrical equilibrium between tip and sample (if no additional voltage is applied) for sufficiently small distances between tip and sample. The Fermi level of both surfaces are at the same energy and the electrons have no preferred tunneling direction. (b) Direction of the tunneling current when a negative voltage V is applied to the sample.

$$\phi = \frac{(\phi_S + \phi_T)}{2} \quad (3.1)$$

ϕ_S : work function of the sample

ϕ_T : work function of the tip

For a definite tunneling current direction, a voltage U is applied between the tip and the sample, which shifts the Fermi levels and electrons at higher-level of “Fermi sea” tunnel into unoccupied states of the same energy of the other surface (from sample to tip) (Fig. 3.1(b)). For low tunneling voltages ($U < 1\text{V}$), eq. 3.1 is a good approximation. Although the approximation of a one-dimensional rectangular barrier is a very simplified model, but still some important relations can be deduced from the small voltage approximation. At low tunneling voltages only the electrons with $\phi \approx V-U$, close to the Fermi edge contribute to the tunneling current.

The solution of the time independent Schrödinger equation:

$$\left(-\frac{\hbar^2}{2m}\nabla^2 + W\right)\psi = E\psi \quad (3.2)$$

ψ : electron wave function

E : electron energy

W : height of the potential barrier

is an exponentially decreasing wave function in the vacuum (Fig. 3.2);

$$\psi(z) = \psi(0) e^{-\kappa d} \quad (3.3)$$

with

$$\kappa = \sqrt{\frac{2m(W - E)}{\hbar^2}} \approx \sqrt{\frac{2m\phi}{\hbar^2}} \quad (3.4)$$

d : width of the potential barrier

m : mass of electron

The tunneling current is proportional to the sum of the transition probabilities of the involved state [96, 97]:

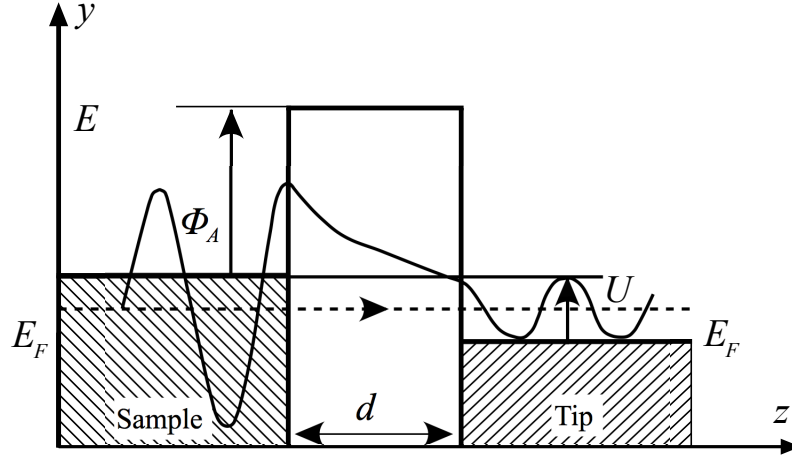


Figure 3.2: One-dimensional rectangular potential barrier and resulting wave function.

$$I \propto T \propto \sum_{E_F - eU}^{E_F} |\psi_n(0)|^2 e^{-2\kappa d} \quad (3.5)$$

In the range eU , the density of states are [96, 97]:

$$\rho(z, E) = \frac{1}{\epsilon} \sum_{E_F - eU}^{E_F} |\psi_n(z)|^2 \quad (3.6)$$

where ϵ is an (infinitesimal) energy range. Assuming that ρ is nearly constant between E and $E \pm eU$ and all electron states between E and $E \pm eU$ can be summed. Therefore, the tunneling current is:

$$I \propto U \rho(0, E_F) e^{-2\kappa d} \quad (3.7)$$

$\rho(0, E_F)$ is the density of states of the Fermi sea in which the electrons are tunneling. Thus the tunneling current is proportional to the tunneling voltage U and to $e^{-2\kappa d}$.

Now we assume that a negative voltage is applied on the sample therefore, the electrons near the Fermi edge of the sample tunnel into unoccupied states of the tip (Fig. 3.2). An increase of the distance between tip and the sample increases the width of the potential barrier and thus decreases the transmission probability and the tunneling current. The strong dependency of the current on the sample-tip distance is of high importance for high-resolution imaging of the surface of the sample. Eq. 3.7 is just an approximate description, while a more detailed description of the tunneling current has to include the following:

- three dimensional geometry
- different Fermi levels of the sample and the tip
- deviation of the potential barrier height from the vacuum level
- interaction between tip and sample for low tip-sample distances

The theory of Tersoff and Hamann is a commonly used approach to make a quantitative prediction of the tunneling current. This model includes the wave functions of the electrons of the tip and the sample [98, 99] and is based on the considerations of Bardeen [100]. In this simple, but nonetheless realistic model, the wave function is separated in a wave function of the tip ψ_μ and of the sample ψ_ν . The two sub-systems are assumed to be independent of each other and thus tip-sample interactions are neglected. The transition probability $\omega_{\mu\nu}$ of an electron (energy E_ν) to tunnel in an unoccupied state of the tip is calculated with the matrix element $M_{\mu\nu}$. $M_{\mu\nu}$ depends on the overlap of the wave functions of the tip and the sample.

$$M_{\mu\nu} = \frac{\hbar^2}{2m} \int d\vec{s} \cdot (\psi_\mu^* \vec{\nabla} \psi_\nu - \psi_\nu \vec{\nabla} \psi_\mu^*) \quad (3.8)$$

$$\omega_{\mu\nu} = \frac{\hbar^2}{2m} |M_{\mu\nu}|^2 \delta(E_\nu - E_\mu) \quad (3.9)$$

The integral in eq. 3.8 extends over an arbitrary area between the tip and the sample. The resulting current is

$$I = \frac{2\pi e}{\hbar} \sum_{\mu,\nu} f(E_\mu) [1 - f(E_\nu + eU)] |M_{\mu\nu}|^2 \delta(E_\mu - E_\nu) \quad (3.10)$$

where $f(E)$ is the Fermi function, μ represents the tip states with energy E_μ and ν represents the surface states. The Fermi function $f(E)$ ensures tunneling to occur from occupied tip states into unoccupied surface states $[1 - f(E_\nu + eU)]$ at positive bias voltage. The term eU is the applied voltage. The delta function restricts the tunneling process to transitions with energy conservation. For small tunneling voltages (≈ 10 mV) and low temperatures, the Fermi function can be approximated by a step function and the Fermi levels of tip and sample are nearly equal. In this case eq. 3.10 can be written as:

$$I = \frac{2\pi}{\hbar} e^2 U \sum_{\mu,\nu} |M_{\mu\nu}|^2 \delta(E_\nu - E_F) \delta(E_\mu - E_F) \quad (3.11)$$

For further simplification for the calculation of I and $M_{\mu\nu}$ Tersoff and Hamann have introduced some more approximations. In addition to the independence of the wave functions of sample and tip and the proportionality of the tunneling current to the matrix element they have assumed wave functions with certain symmetries. The wave function of the sample is represented by a two dimensional Bloch wave, which takes the lattice periodicity into account, with exponential decay in z-direction. The tip is assumed to be spherically symmetric and therefore mainly s-waves from the tip contribute to the tunneling current and ψ_μ is expressed by s-wave functions (Fig. 3.3).

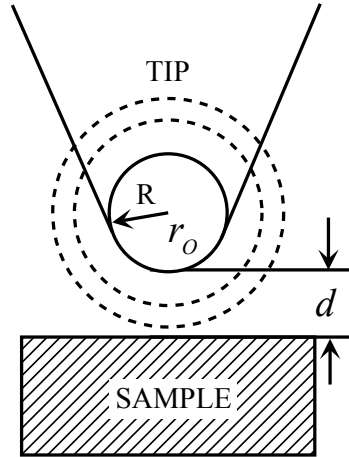


Figure 3.3: Model of a spherical tip and the s-states which are one of the solutions of the time independent Schrödinger equation for a spherically symmetric potential.

Using the assumed wave functions and replacing $M_{\mu\nu}$ in eq. 3.11 leads to an approximation of the tunneling current [96, 101]:

$$I = \frac{32\pi^3 e^2 V \phi D_T(E_F) R^2 e^{2\kappa R}}{\hbar \kappa^4} \sum_{\nu} |\psi_{\nu}(\vec{r}_o)|^2 \delta(E_{\nu} - E_F) \quad (3.12)$$

D_T : density of states of the tip per volume

R : radius of tip

\vec{r}_o : position of the centre of the tip

the sum $\sum_{\nu} |\psi_{\nu}(\vec{r}_o)|^2 \delta(E_{\nu} - E_F)$ is the local density of states of the sample $\rho_s(\vec{r}_o, E_F)$ at the position \vec{r}_o .

In constant current mode, the tip images the contours of a constant density of states of the sample surface. This reflects the electronic properties of the surface as well as the surface topography. Atoms that have the same geometrical height can be imaged by STM differently due to different density of states and appear as a chemical contrast in STM images.

3.1.2 Low-Energy Electron Diffraction (LEED)

The low energy electron diffraction is a commonly used surface analyzing technique for identifying periodic structures on crystals. The de-Broglie wavelength of free electrons can be calculated using:

$$\lambda = \frac{h}{\sqrt{2mE}} \quad (3.13)$$

λ : de-Broglie wavelength

h : Plank's constant

m : mass of electron

E : energy of electron

In LEED, the electrons with energies in range 20 - 500 eV have de-Broglie wavelengths of 0.5 - 2.7 Å. These wavelengths corresponds to the order of the atomic distances, hence satisfy the diffraction condition in crystal lattices. As the mean free path of these electrons is very low (few atomic layers), therefore this makes LEED a highly sensitive technique probing the top few layers of the sample.

Backscattered electrons from the surface lead to interference between the wavefunctions of the electrons. Depending on the wavelength λ and the angle of the scattered electrons to the sample normal ϕ , diffraction minima and maxima appear. This results in an image which is the reciprocal lattice of the investigated surface structure. The bigger the distances of the maxima of the diffraction pattern, the smaller is the periodicity of the crystal surface.

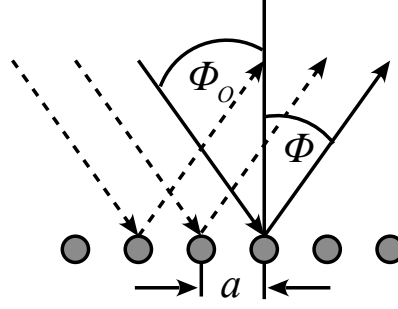


Figure 3.4: Scattering of a plane wave at a one dimensional periodic lattice [97].

The maxima for the one dimensional diffraction, as shown in Fig. 3.4, have to satisfy:

$$a(\sin \phi - \sin \phi_o) = n\lambda \quad (3.14)$$

λ : Wavelength of the primary electrons

ϕ_o : Angle between primary electrons and the sample normal

ϕ : Angle between diffracted electrons and the sample normal

a : Lattice constant

n : Order of the maximum

For a two dimensional lattice, the lattice constant a is replaced by the row distance d_{hk} in direction of the Miller indices (hk) . If the primary electrons with a kinetic energy E (in eV) hit the surface at perpendicular incidence, then the angle dependent maxima of the interference of the backscattered electrons is given by [101, 102]:

$$\sin \phi = \frac{n}{d_{hk}} \sqrt{\frac{150}{E}} \quad (3.15)$$

For the LEED measurements in this work the electrons were emitted from a lanthan-hexaboride-filament. These electrons were accelerated between filament and sample by a

variable voltage. The angular dependent maxima of the interferences of the wave functions of the backscattered electrons were detected on a transparent screen which is covered with a material with high electroluminescence (like phosphor). The LEED pattern is recorded with a camera. As inelastically scattered electrons would reduce the quality of the LEED measurements there are two additional grids between sample and phosphoresced screen. The first one is grounded and the second one is at a variable negative voltage. A positive voltage of some kV is applied at the phosphoresced screen. By adjusting the potential of the grid the diffuse background of inelastically scattered electrons is reduced.

3.1.3 Auger Electron Spectroscopy (AES)

When electrons in energy range of $2 \sim 50$ keV are irradiated on a surface, atom gets ionized by emitting core shell electrons. The resulting hole in the core shell is filled by an electron from a shallower level along with emission of energy. This energy may appear as kinetic energy transferred to another electron which is loosely bound to atom, and hence results in an Auger electron. This energy is independent of the energy of the primary electrons. This effect is known as Auger effect. The Auger electron carries a characteristic information about the material [95, 97].

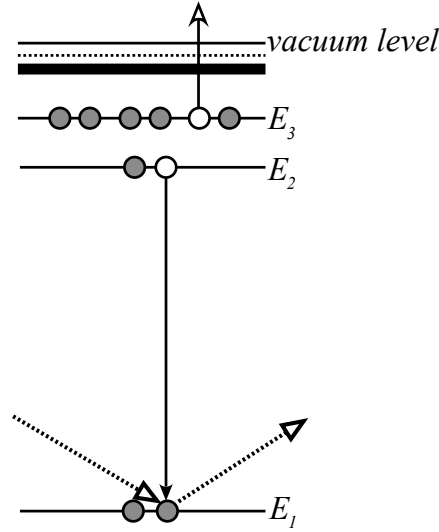


Figure 3.5: Energy level diagram of an Auger process. Electron from E_2 drops into the E_1 level with the emission of an E_3 electron [95, 97].

The kinetic energy of the ejected Auger electron is given by eq. 3.16.

$$E_{Auger} = E_1 - (E_2 + E_3) \quad (3.16)$$

E_{Auger} : Kinetic energy of the Auger electron

E_1 : Binding energy of the electron ejected from the core level

E_2 : Binding energy of the filling electron

E_3 : Binding energy of the Auger electron

Conventionally, the binding energies are taken positive with respect to the vacuum level as zero. The depth sensitivity of AES process is mainly dependent on the inelastic mean free path (IMFP) of the Auger electrons. As these electrons have typically energies of \sim hundred eV, the average escape depth is about 10 Å. Therefore AES is sensitive to the few uppermost layers.

Normally, the Auger signal is a rather small peak compared to the background signal from inelastic backscattered primary electrons. Therefore, the recorded continuous spectrum is differentiated to subtract the continuous background and to enhance the visibility of weak peaks. The minima of the peaks in the derivative of the original spectrum are the energies given for the Auger electrons and the intensity of the peaks is measured by the distance between the minimum and maximum of the respective peaks (Auger Peak to Peak Height - APPH) [95].

In this work AES is used to check the cleanliness of surfaces after cleaning and to check the chemical composition of the surface. For these measurements ratios of the APPH of the investigated element with the APPH of the substrate are used (e.g. $C_{273} / (Fe_{703} + Cu_{920})$ or $O_{515} / (Fe_{703} + Cu_{920})$).

AES spectra were taken with a CMA (Cylindrical Mirror Analyzer) with a concentric electron gun. The primary electrons were emitted from a tungsten cathode, accelerated by a voltage of 3 keV and focused to an incident beam of about 0.5 mm beam diameter. The angle between the axis of the analyser and the surface normal is 30° in the STM and 0° in the SMOKE system.

3.2 Surface magneto-optic effect

To investigate the magnetic properties of the transformed films [fcc (paramagnetic) to bcc (ferromagnetic)] presented in this thesis, we used the surface magneto-optic Kerr effect (SMOKE) measurement technique. In material science, the standard method used for measuring magnetization curves is by Kerr effect called MOKE (Magneto-optic Kerr Effect) and for thin magnetic films it is called SMOKE (surface magneto-optic effect) invented in 1985 [103, 104]. Also Kerr microscopy is used for Imaging magnetic domains [105, 106].

3.2.1 Kerr Effect

When a linearly polarized light interacts with a surface of a magnetized material, it results in the rotation of the outgoing polarized light, as well as gives rise to ellipticity. If the light is transmitted from the magnetized sample, it is called Faraday effect and for reflected light, it is known as Kerr effect (Fig. 3.6). As we have used only Kerr effect for measuring the magnetic properties in the presented work, we only focus on the Kerr effect. The Kerr effect can be described by complex angle ϕ_F which is proportional to the magnetization of the sample.

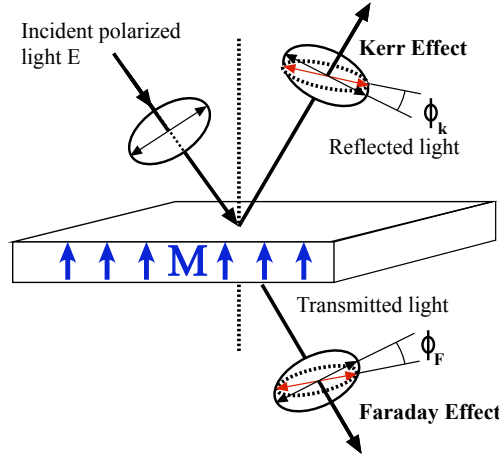


Figure 3.6: Schematic view of the Faraday (transmitted-light) and Kerr (reflected-light) effects.

The angle consists of the real part θ which describes the direction of rotation of polarization and the imaginary part ε describes the ellipticity. Fig. 3.7 shows both components i.e. the rotation angle and ellipticity. As the linearly polarized incident light can be described as left circular or right circular polarized light, therefore, different absorptions for the right and the left circularly polarized light gives rise to ellipticity. And different phase shifts for the right and the left circularly polarized light gives rise to rotation.

The Kerr rotation θ_k and the Kerr ellipticity ϵ_k for the s- and p- polarized light are given as [57, 107]:

$$\phi_s = \theta_s + i\epsilon_s = \frac{r_{ps}}{r_s} \quad (3.17)$$

$$\phi_p = \theta_p + i\epsilon_p = \frac{r_{sp}}{r_p} \quad (3.18)$$

Where r is the reflection coefficient and subscripts s and p stand for the s- and p-polarized light. (r_{ps} : reflection coefficient from an incident p-polarized light to a reflected s-polarized

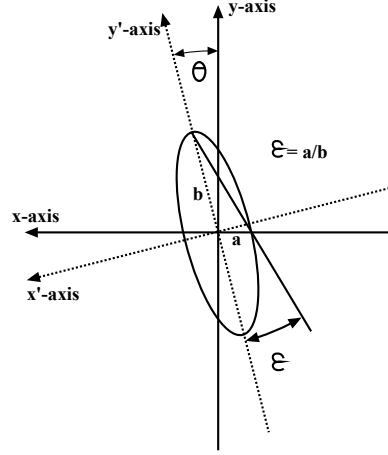


Figure 3.7: Geometrical representation of Kerr angle ' θ ' (the real part of complex angle) and the ellipticity ' ϵ ' (the imaginary part of the complex angles). ' θ ' is related to the major axis of the ellipse whereas ' ϵ ' is related to the minor to major axis ratio.

light and vice versa for r_{sp})

For ultrathin films where the overall thickness is much smaller than the wavelength of the light wave ($\sum_i n_i d_i \ll \lambda$, where n is the refractive index, d is the thickness, and also $\lambda = 632.8$ nm for He-Ne laser) [104], then the following equations are valid:

$$r_s = \frac{n_i \cos \theta_i - n_f \cos \theta_f}{n_i \cos \theta_i + n_f \cos \theta_f} \quad (3.19)$$

$$r_p = \frac{n_f \cos \theta_i - n_i \cos \theta_f}{n_f \cos \theta_i + n_i \cos \theta_f} \quad (3.20)$$

$$r_{ps} = -\frac{4\pi}{\lambda} \frac{n_i \cos \alpha}{(n_i \cos \alpha + n_f \cos \beta)(n_f \cos \alpha + n_i \cos \beta)} \cdot (\cos \beta \sum_m d_m n_m^2 Q_z^{(m)} - n_f n_i \sin \alpha \sum_m d_m Q_y^{(m)}) \quad (3.21)$$

$$r_{sp} = -\frac{4\pi}{\lambda} \frac{n_i \cos \alpha}{(n_i \cos \alpha + n_f \cos \beta)(n_f \cos \alpha + n_i \cos \beta)} \cdot (\cos \beta \sum_m d_m n_m^2 Q_z^{(m)} + n_f n_i \sin \alpha \sum_m d_m Q_y^{(m)}) \quad (3.22)$$

In these equations n_i , θ_i and n_f , θ_f are the refraction indices and the incident angles of the topmost layer (i) and the lowest layer (f) which can be substrate. The z represent the surface normal and y represents the plane of incidence. The parameter m is the number of

layer, and d_m is the thickness of layers. Further more, Q_y and Q_z are Voight vectors which is proportional to the magnetization of the film [57].

The equations from 3.19 to 3.22 show that the total Kerr angle is the sum of the single Kerr signal of the magnetization of single layers and is independent of the single non-magnetic layer in a multi layer system. For thicker layers this is not valid due to the absorption.

Further, the coefficients responsible for the reflected polarized wave depend strongly on the direction of the sample. This leads to three different geometries shown in Fig. 3.8. They are different in the direction of magnetization \vec{M} related to the incident plane of light. One gets the complex Kerr angle in longitudinal and polar geometry. In transversal geometry, the reflectivity changes due to the reversal of the magnetic field. Here, only the polar Kerr effect is computed to show the mathematical scheme. For further details one can consult literature [108].

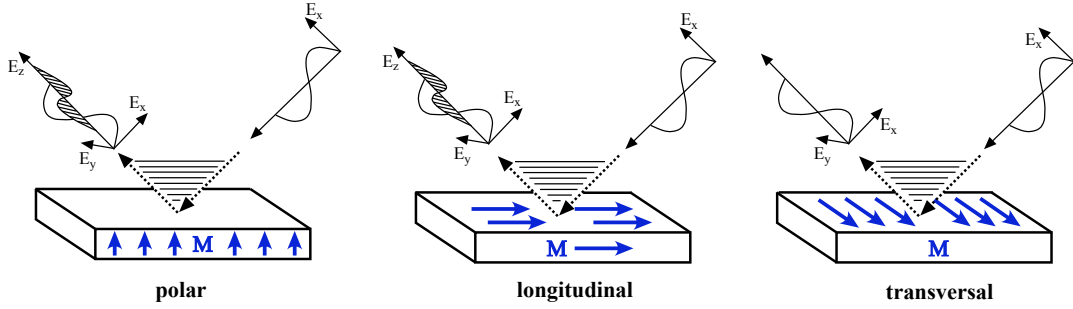


Figure 3.8: (a) Polar: \vec{M} perpendicular to sample plane and parallel to plane of incidence, (b) Longitudinal: \vec{M} parallel to sample plane and plane of incidence, (c) Transversal: \vec{M} parallel to sample plane and perpendicular to the plane of incidence

Chapter 4

Experimental setup

4.1 UHV system

This chapter describes the experimental set-up and the procedures of the samples preparation in the study.

4.2 Experimental set-up

Maintaining surface cleanliness over a period of experiment time (several minutes to several hours) is a fundamental problem of surface science. Assuming 1 to be the sticking coefficient of a particle (residual gas molecule) striking the surface, with a pressure of 1×10^{-6} mbar, it takes ≈ 1 second to form 1 ML (monolayer) of adsorbed particles. For studying clean surfaces, pressures in the UHV (ultra high vacuum) range ($p < 10^{-10}$ mbar) are inevitable for measurements. The measurements done in this thesis were conducted in two different UHV-systems, one focusing on structural analysis and the other focusing on magnetic properties.

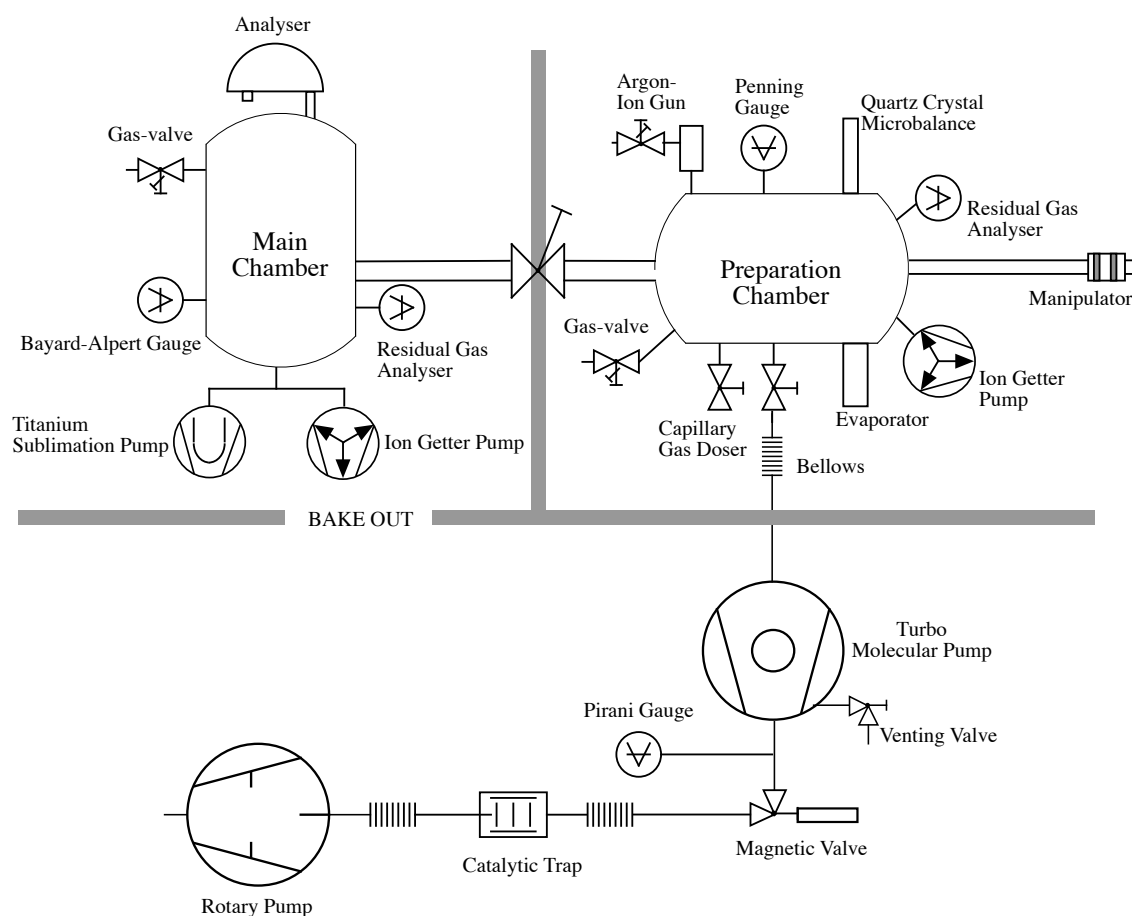


Figure 4.1: Schematic view of the RT-STM [102].

4.2.1 The RT-STM (Room Temperature Scanning Tunneling Microscopy) system

The structural analysis/RT-STM UHV setup comprises two chambers, the preparation chamber and the analysis chamber. Typical base pressure in the preparation chamber was below 1×10^{-10} mbar, measured by a Penning gauge. The UHV in the preparation chamber is maintained by an ion pump, a turbo molecular pump and a rotary vane pre-vacuum pump. Samples are transferred between the chambers with a magnetically coupled transfer rod. The preparation chamber contains of an Ar^+ ion source, a capillary doser, electron beam evaporators, a quartz crystal microbalance, a gas cracker and a quadrupole mass spectrometer. The crystal surfaces were cleaned in the preparation chamber by sputtering (Ar^+ ion bombardment) and annealing by electron beam heating of the sample plate. The surfaces were then coated with metals from evaporators. Surface analysis was done in the

analysis chamber with a base pressure typically below 4×10^{-10} mbar, measured by a Bayard Alpert gauge. The UHV pressure in the main chamber is maintained by an ion getter pump and a liquid-nitrogen cooled Ti sublimation pump. The analysis chamber houses a customized commercial STM (Omicron μ -STM) operated in constant current mode with an electrochemically etched W tip. It also contains instrumentation for low energy ion scattering (LEIS), low energy electron diffraction (LEED), quadrupole mass spectrometer (QMS), Auger electron spectroscopy (AES) and x-ray photo spectroscopy (XPS). The quadrupole mass spectrometer mounted on both chambers was used to measure residual gas composition. To obtain atomic resolution, it was inevitable to minimize the vibrations (vibrations from the building are in μm range) during STM measurements. This was carried out by suspending the RT-UHV system on five springs. The ion source used for the fcc-bcc transformation was scanning the sample at an incidence angle of 20° with respect to the sample normal.

4.2.2 The setup for ion irradiation through a mask

The RT-STM UHV system was used for conducting the masked experiments. For that purpose the analysis chamber was modified by replacing the LEED instrumentation by an ion-source (VG AG-6), which was mounted so that it was perpendicular to the mask and the sample surface. The SiN mask was manufactured by FIB in Hamburg [109, 110]. The entire mask (membrane plus carrier) is 5×5 mm large and the SiN membrane (100 nm thick plus 30 nm gold coating) is $500 \mu\text{m} \times 500 \mu\text{m}$. It has 80-nm wide holes, forming a square lattice with $1 \mu\text{m}$ spacing and $100 \mu\text{m} \times 100 \mu\text{m}$ size. The whole mask contains 3×3 such hole arrays [Fig. 4.2]. The SiN mask was glued to the bottom of a Cu cone having a 2 mm hole in the center. Fig. 4.3(a) shows a schematic view of the experimental setup in the vacuum: the cone [Fig. 4.3(b)-(c)] is lowered until the mask touches the surface of the Fe-coated Cu crystal. As the holes were eroded by the FIB from the side facing the Fe/Cu sample, the sidewalls of the holes, if not perfectly parallel, are overhanging. Thus, the Ar ion beam in our experiment cannot impinge on the sidewalls, which means that the sample cannot be contaminated by sputtered mask material. Also, the copper cone holding the mask was designed such that sputtered material from it cannot reach the sample.

The mask is not in perfect contact with the film surface at every point on the Cu crystal due to uneven crystal surface, which is due to roughness remaining after the polishing and defects in the crystal introduced by many annealing cycles. Assuming typical values, $10 \mu\text{m}$ distance between the mask and the sample and collimation of the beam within 0.2° , the beam gets widened by 35 nm on the Fe/Cu surface. At a pressure of 10^{-6} mbar, the mean free path of the ions is approximately 300 m until a deflection between 0.2 and 3° occurs. Only a small fraction of the ions scattered by the gas atoms in this angle range will actually hit the mask. Thus, the fraction of ions (or atoms, if neutralized in the collision) passing the mask with an angle differing from that of the well-collimated beam due to scattering will be low, below 10^{-3} .

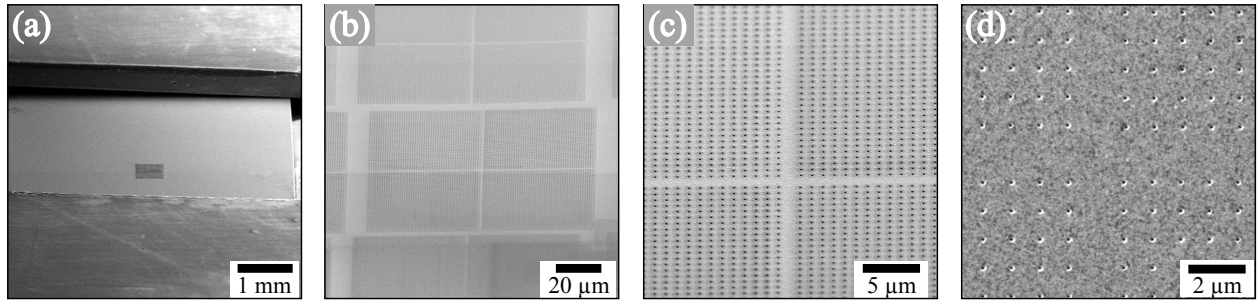


Figure 4.2: Scanning electron micrographs showing the mask with different magnifications. Frame (a) shows the carrier; the membrane appears dark in the center of the image.

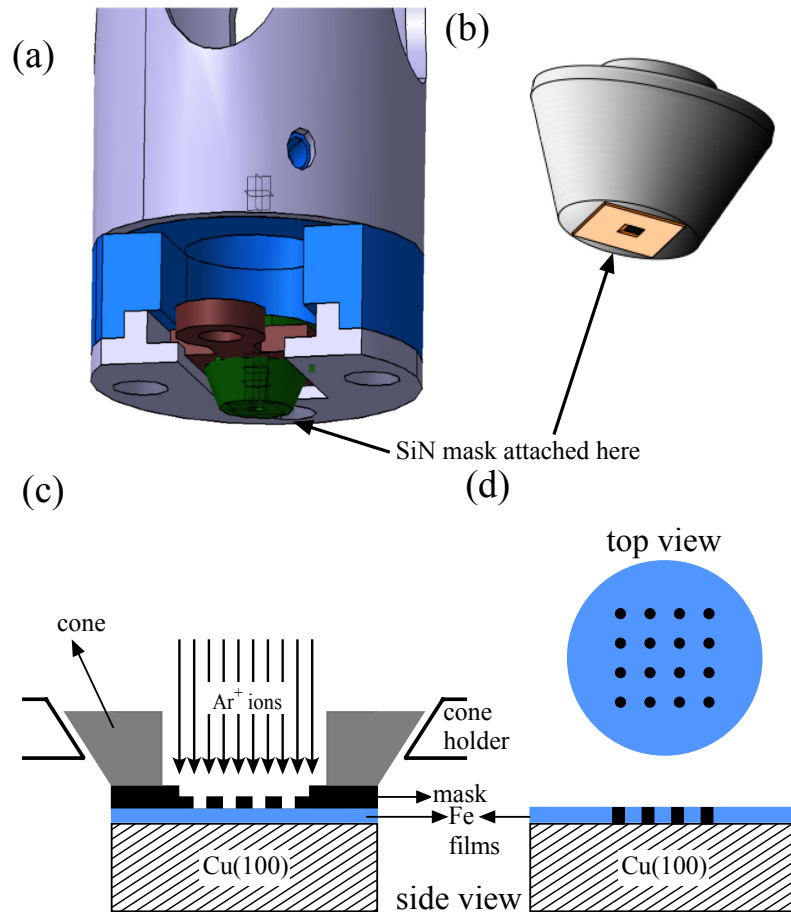


Figure 4.3: (a) Schematic view of the experimental set-up for patterning. (b) view of the cone with mask glued at the lower side (c) the cone plus mask placed on the fcc Fe/Cu(100) film and bombarded with Ar^+ ions. (d) the patterned film after removing the mask.

As the mask is much smaller than the Cu crystal, we irradiated the crystal in two rows, with 5-7 positions in each row (rows and irradiation positions within the rows were separated by 0.5 mm distance) to increase the probability to find the irradiated area by STM. Nevertheless, the total ion dose on the mask was low enough to prevent significant damage of the mask; we estimate that 30 nm (estimated dose: $\approx 1.3 \times 10^{17}$ ions/cm², sputter yield: 2 [111, 112]) SiN was sputtered over the course of all our experiments, much less than the thickness of the SiN layer (100 nm). Finally, the irradiated nano-patterned fcc Fe film, schematically shown in Fig. 4.3(d), was transferred to the STM position.

The ion beam for the fcc-bcc transformation was created by a VG AG-6 ion source and directed at the mask and sample at perpendicular incidence. Due to the small source size (ionization volume < 1 mm³) and large distance (≈ 430 mm) from the focusing lens to the sample, the ion beam at the sample surface is highly collimated. During ion bombardment, the Ar pressure in the chamber was 9×10^{-7} mbar, so we have to consider scattering of Ar ions by Ar gas atoms. We assume that scattering by an angle of less than 0.2° has not much influence on the beam quality because this angle is only barely above the angular spread of the beam. We can also neglect large scattering angles (above $\approx 3^\circ$) because this would require scattering close to the mask (low scattering probability within this short distance) and the cross section decreases with increasing scattering angle.

The time-averaged ion flux was measured with a Faraday cup biased at +27 V to eliminate the influence of secondary electrons on the current measurement. The typical ion flux was $\approx 10^{12}$ ions/cm²/s.

4.2.3 The SMOKE setup (Surface Magneto-Optical Kerr Effect)

The other UHV setup is a single chamber consisting of almost same facilities as for the sample preparation and characterization mentioned before in section 4.2.1, except for STM and XPS. The base pressure in this chamber was below 5×10^{-11} mbar (Bayard Alpert gauge). In this system, we used a SMOKE system to measure hysteresis curves using a He-Ne laser (632.8 nm) and a photo elastic modulator. The laser beam is linearly polarized at an angle of 45° w.r.t. the plane of incidence and modulated before it enters the vacuum chamber; the angle of incidence on the sample is 60° w.r.t. the surface normal. In the present study, the polarization analyzer was set to select the p-polarized light. The magnetic field was parallel to the surface (longitudinal SMOKE).

The ion source used for the fcc-bcc transformation was scanning the sample at perpendicular incidence. Typical current densities were $\approx 10^{12}$ ions/cm²/s.

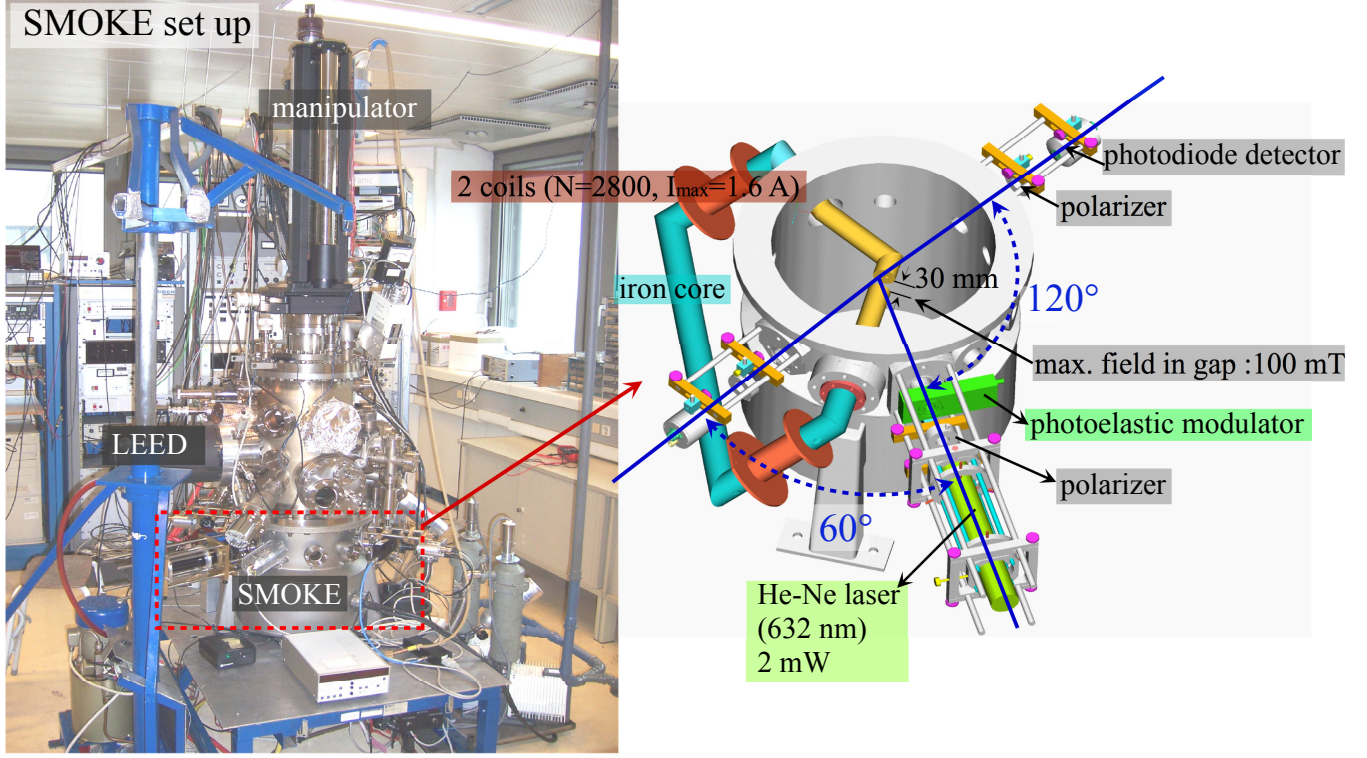


Figure 4.4: Schematic view of the Smoke Setup [57].

4.2.4 Sample preparation

The Cu(100) crystal was cleaned by sputtering using 2 keV Ar^+ ions ($I_{\text{sample}} = 2 \mu\text{A}$, typically 30 min) and annealing (520°C , 10 minutes). A few sputtering/annealing cycles resulted in large flat Cu terraces with widths around 100 nm and a clean surface was determined by AES.

Fe films were evaporated from tips of Fe rods (2 mm thick, purity 99.99+%) heated by electron bombardment. The deposition rate of 1 ML/min was calibrated by placing a quartz crystal microbalance at the sample position. For clean 8 ML fcc Fe films, Fe rods annealed in hydrogen were used to minimize the oxygen content in the films which might influence the rate of transformation of the films. For thicker fcc Fe films, oxygen was not a problem as we wanted oxygen to diffuse to surface and contribute to the surface stability of films. During evaporation of Fe (and $\text{Fe}_{64}\text{Ni}_{36}$) from rods, we applied a retarding voltage of +1.5 kV to a cylindrical electrode in the orifice of the evaporator (the so-called “flux monitor” electrode). This is in order to suppress the high-energy ions bombarding the growing film on Cu(100) crystal surface which may modify the growth mode of the films [113].

4.2.5 Ion current measurement and neutralization problems

In the ion sources (in RT-STM), a significant fraction of the fast Ar^+ ions gets neutralized by Ar atoms in the gas (charge transfer is a resonant process and thus has a high cross section). These neutrals are not affected by the deflection plates and electrostatic lenses, only collimated by the apertures. To achieve well-defined ion doses, we found it essential to place the sample in a position where the area used for later analysis is outside the impact area of the neutrals, i.e., outside the axis of the ion source. The time-averaged ion flux was measured with a Faraday cup, biased at +27 V to eliminate the influence of secondary electrons on the current measurement. In the STM system, where some Faraday-cup measurements were inaccurate due to secondary electrons reaching the wiring of the Faraday cup, we have also used measurements of the sample current (corrected for secondary electrons by putting the sample on positive bias) and the irradiated area.

In the SMOKE setup, the ion source used for fcc to bcc transformation was equipped with a wien-filter taking care of the neutralization problem, and hence no contribution from neutrals. Therefore, only the Faraday cup biased at +27 V sufficed the required ion flux during ion irradiation of the sample.

The effect of the ions at the two angles of incidence used in two systems (cf. 4.2.1 and 4.2.3), should be almost identical at ion energies up to 1 keV, where channeling is almost negligible. At higher ion energies, perpendicular incidence will lead to a somewhat higher penetration depth of the ions.

Chapter 5

8 ML Fe films on Cu(100)

5.1 Introduction

This chapter presents a comparison of the STM measurements conducted on 8 ML fcc Fe films in the current work to the SMOKE measurements done on the same system by Rupp et al. [57]. The main issue addressed in this chapter is the effect of type and energy of noble gas ions on the efficiency of the fcc \rightarrow bcc transformation of 8 ML fcc Fe films. Also we explored the transformation of a Au coated 8-ML Fe film with Ar^+ ion irradiation.

In this study, two UHV chambers; SMOKE (see section 4.2.3) and STM (see section 4.2.1) systems were used. In both chambers, 8 ML fcc Fe films were prepared by standard preparation method described in section 4.2.4. The as-prepared 8 ML fcc Fe film surface was then irradiated with different noble gas ions, in both chambers.

5.2 SMOKE measurements

In this section, SMOKE results for the 8 ML fcc Fe films irradiated with the noble gas ions i.e. He^+ , Ne^+ , Kr^+ and Xe^+ ions at different energies are presented. We carried out SRIM calculations for this system to estimate the involved number of atoms N_m [91] using eq. 2.17 (discussed in detail in section 6.8). These calculations provide a better base for understanding experimental results of this system.

Fig. 5.1 shows N_m as a function of increasing ion energy for different ions. The relative fraction of Fe (squares) and Cu (triangles) atoms in the melt is plotted along with their sum

(circles). Small schematic diagrams for Fe/Cu(100) bombarded by high and low energy ions are shown to the right and left of the graph respectively. Following key points can be inferred from the Fig. 5.1:

- For the lightest ions, i.e. for He^+ ions, we observe negligible fraction of Fe atoms in the melt as seen in Fig. 5.1(a). Already at 1 keV, almost all He^+ ions lose their energy to the Cu substrate. This means hardly any collision takes place in the Fe film. This trend continues for higher energies due to increase in penetration depth for He^+ ions with increasing ion energy.

For all other ions, i.e. Ne^+ , Ar^+ , Kr^+ and Xe^+ ions:

- Let's name the point where the fraction of Fe and Cu atoms in the melt is equal, as the 'crossing point'. For all ions below the crossing point, the fraction of Fe atoms in the melt is higher than the Cu atoms. The energy of crossing point increases with the increase in the mass of the noble gas ion. For Ne^+ , Ar^+ , Kr^+ and Xe^+ ions, this point is ~ 1 keV, 2 keV, 4 keV and 5.5 keV (extrapolating the data) respectively [see Fig. 5.1(b-e)].
- For higher ion energies above the crossing point, the relative fraction of Cu content in the melt increases. This trend continues for higher ion energies [see Fig. 5.1(b-e)].

Fig. 5.2 shows the longitudinal Kerr ellipticity at saturation value, ε_{sat} , and the coercive field H_c as a function of ion dose and ions/surface atom for different ions with different ion energies. As the SMOKE measurements conducted with He^+ ions at different energies showed no fcc-bcc transformation, therefore they were not included here. The main observations from the Fig. 5.2(a-d) are summarized below:

- Generally, the ellipticity ε_{sat} curve starts at a threshold dose and then increases with the increase in ion dose. After reaching a saturation point, the ellipticity value starts decreasing. This magnetic evolution trend is generally true for all ions at all energies. The maximum ellipticity value obtained for all ions is close to $\sim 150 \mu\text{rad}$. For Ne^+ and Ar^+ ions, the transformation curves at different energies are quite distinct i.e. each curve has a unique saturation value, whereas for Kr^+ and Xe^+ ions, they share same saturation value for almost all energies [compare Fig. 5.2(a,b) to (c,d)]. The typical value of threshold ion dose is $< 1.0 \times 10^{14}$ ions/cm² for all ions.
- The coercive field H_c being higher in the start of the ion irradiation drops down quickly with increasing ion dose. This is also true in general for all ions. For Ne^+ and Ar^+ ions, the typical value of coercive field at the threshold dose is typically ~ 300 Oe. For Kr^+ and Xe^+ at higher ion energies (above 1 keV), it is close to ~ 100 Oe.

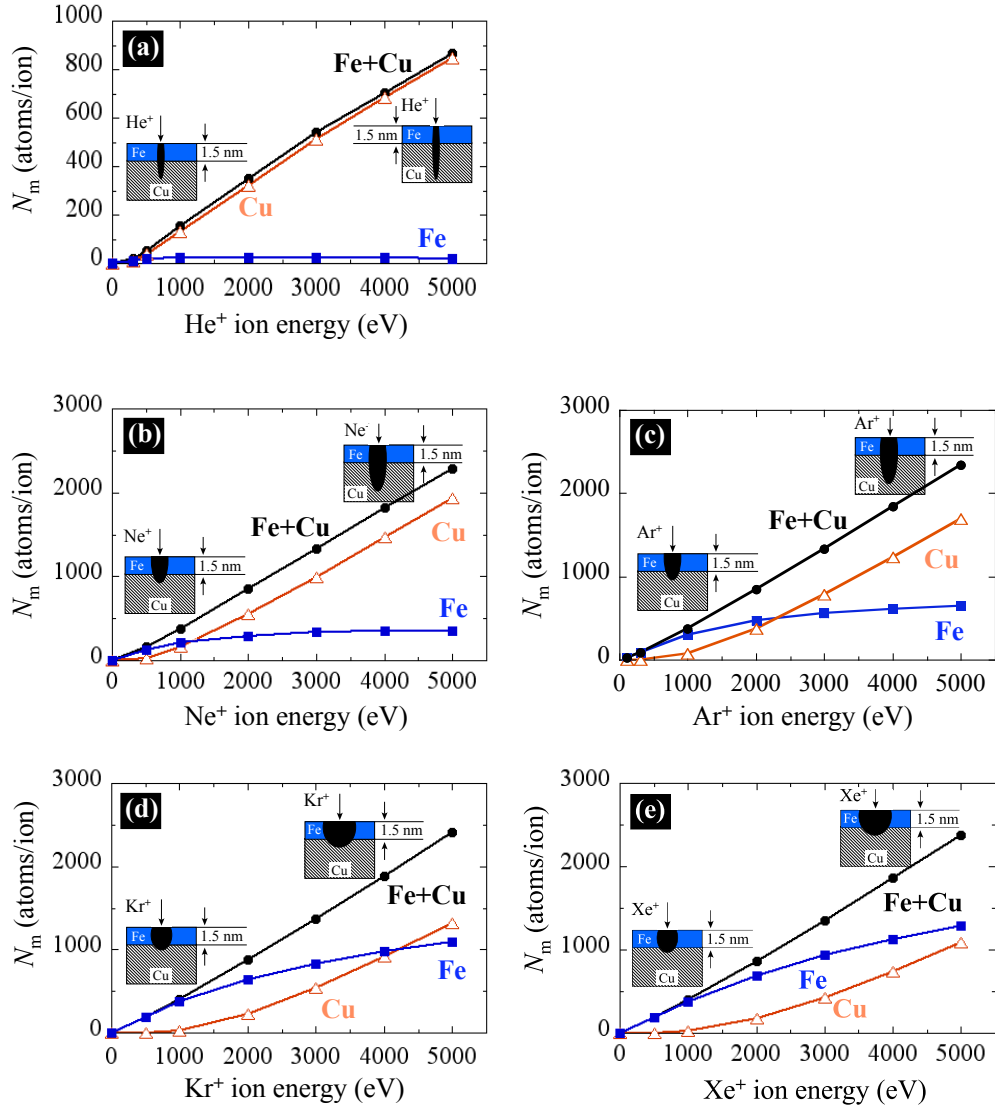


Figure 5.1: Calculated number of involved atoms N_m in molten volume as a function of ion energy for 8-ML-thick fcc Fe film on Cu-substrate for different ions: (a) He^+ , (b) Ne^+ , (c) Ar^+ , (d) Kr^+ , (e) Xe^+ ions. Each graph is marked with small schematic diagrams for low and high ion energies showing the size and penetration depth for respective ions at respective energies.

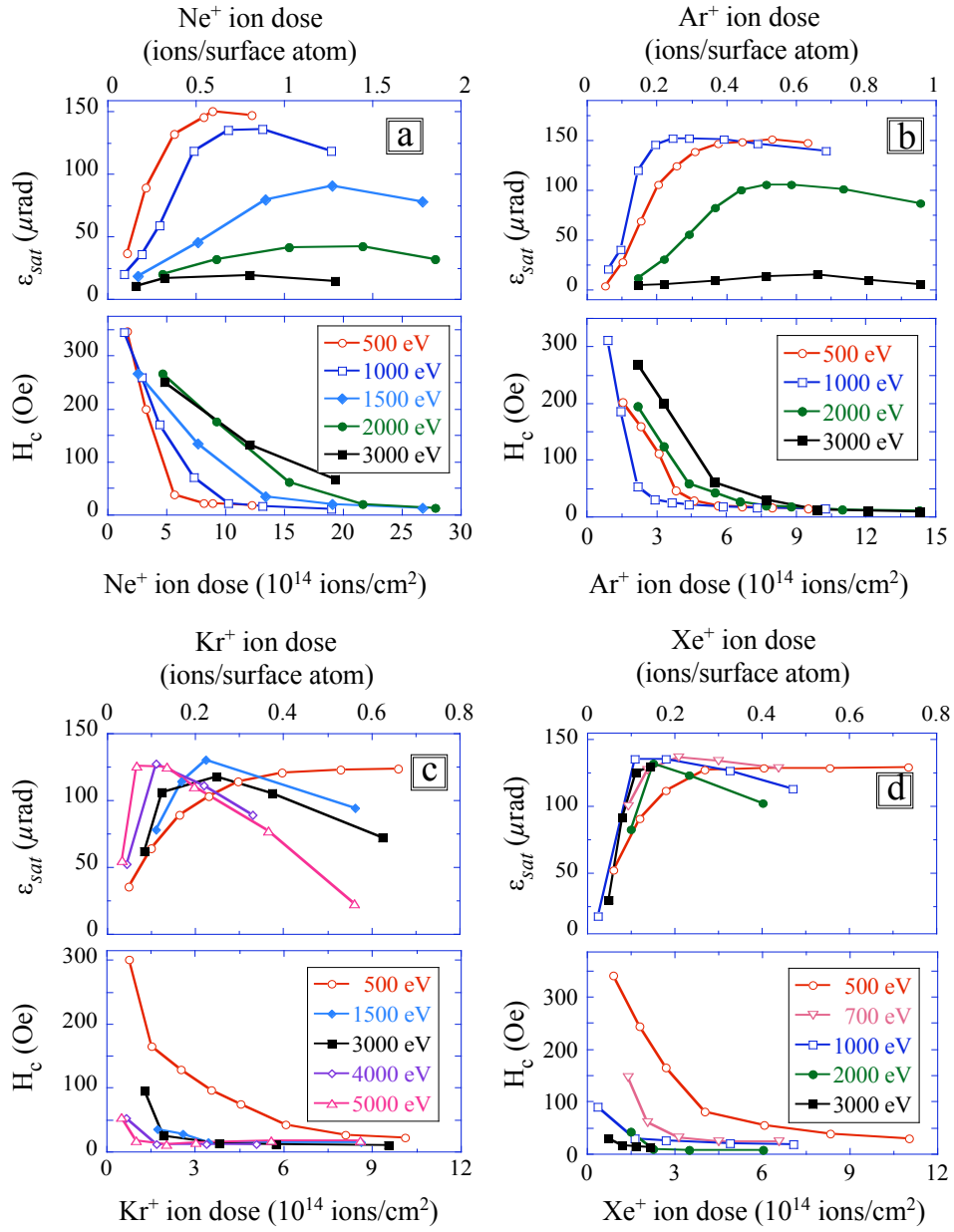


Figure 5.2: Longitudinal Kerr ellipticity at saturation value, ϵ_{sat} , and coercive field H_c are plotted as a function of ion dose for 8-ML thick fcc Fe film grown on Cu(100) and irradiated with: (a) Ne⁺, (b) Ar⁺, (c) Kr⁺, and (d) Xe⁺ ions. Data from Ref. [57]

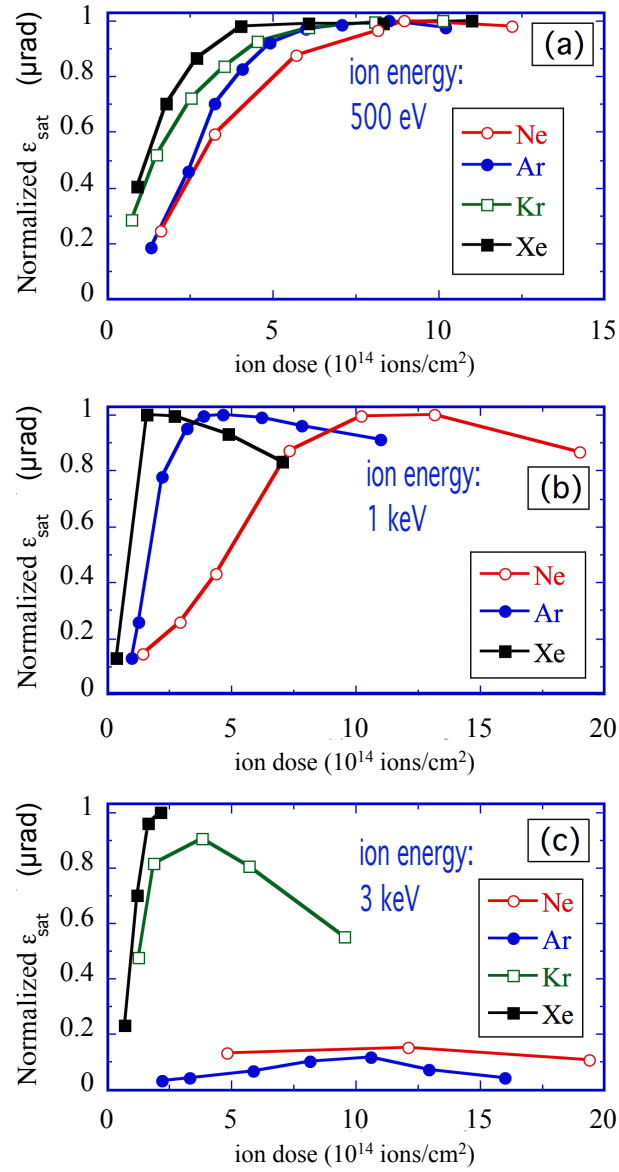


Figure 5.3: Normalized longitudinal Kerr ellipticity signal at saturation value, ϵ_{sat} , as a function of ion dose for different gases at (a) 500 eV, (b) 1 keV, and (c) 3 keV. Data from Ref. [57, 64]

- The best transformation results obtained for Ne^+ , Ar^+ , Kr^+ and Xe^+ ions are at 500 eV, 1 keV, 5 keV and 1 keV respectively. The 5 keV (Kr^+) and 1 keV (Xe^+) best transformation energies show the experimental uncertainty. At least, one can note that there is no significant difference between the high ion energies for Kr^+ and Xe^+ ions. The respective ion doses required to reach the maximum ellipticity value for

the best transformation results of Ne^+ and Ar^+ ions are $\sim 9 \times 10^{14}$ ions/cm² (500 eV) and 4×10^{14} ions/cm² (1 keV) respectively. This value for Kr^+ (5 keV) and Xe^+ (1 keV) ions is $\sim 1 \times 10^{14}$ ions/cm² and 2×10^{14} ions/cm².

- The slowest transformation results obtained for Ne^+ and Ar^+ are at 3 keV, and for Kr^+ and Xe^+ ions at 500 eV ion energy.

Fig. 5.3 shows the normalized value of longitudinal Kerr ellipticity at saturation value ' ϵ_{sat} ' as a function of ion dose for different ions at different ion energies. This is basically the replot of the Fig. 5.2, so as to compare the efficiency of lighter ions to the heavier ones at a particular energy. The main observations from the Fig. 5.3(a-c) are summarized below:

- The best transformation results are obtained for heavier ions at all energies. Xe^+ ions are most efficient in carrying out fcc-bcc transformation of 8-ML Fe films, followed by Kr^+ ions. The Xe^+ ion dose to achieve saturation value is $\sim 5 \times 10^{14}$ ions/cm² for 500 eV and is $\sim 2 \times 10^{14}$ ions/cm² for 1 and 3 keV ion energies. The typical threshold dose at which transformation starts is below $\sim 1 \times 10^{14}$ ions/cm² for Xe^+ ions at all energies. The lighter ions are most slow in carrying out transformation.
- Ne^+ ions being the slowest for 500 eV and 1 keV ion energies; for both it reach the same saturation value [at ion dose: $\sim 10 \times 10^{14}$ ions/cm² (for 500 and 1 keV) as with Xe^+ ions. For 3 keV ion energy, Ne^+ and Ar^+ ions show lowest ellipticity values
- The transformation curve for Xe^+ ions is much steeper at 2 and 3 keV ion energies than at 500 eV where a gradual increase is observed.

5.3 STM measurements

As we already have developed a general understanding for the trend of ions in the 8 ML fcc Fe film from SRIM calculations and SMOKE measurements, therefore now we present specific STM measurements with different ions at particular energies to provide a supporting evidence for the presented SMOKE data. The ion doses presented here for Ne^+ , Ar^+ and Xe^+ ions are estimated from the sample target current during ion irradiation, scaled to the same scan size.

Fig. 5.4(a) shows an STM image of the as-prepared clean 8 ML fcc Fe film grown on Cu(100). It manifests layer-by-layer growth with no bcc needles which is a typical for the 8 ML film surface as reported by Rupp et al. [57, 64]. This surface after irradiation with an Ar^+ ion dose of 2.3×10^{14} cm⁻² at 500 eV Ar^+ ion energy, shows very few bcc needles growing in low index crystallographic directions [Fig. 5.4(b)]. The bcc needles are recognized as bright needles due to 5-10% larger interlayer distance between fcc(100) Fe

and bcc(110) Fe. These needles are few tens of nm in length. At an Ar^+ ion dose of $4.5 \times 10^{14} \text{ cm}^{-2}$, the bcc needles are seen to grow in length and width [Fig. 5.4(c)]. With further ion irradiation at $6.8 \times 10^{14} \text{ cm}^{-2}$, the film is found to be close to complete transformation as shown in Fig. 5.4(d).

The STM images of the as-prepared 8 ML fcc Fe film [Fig. 5.5(a)], irradiated with 500 eV Xe^+ ions are presented. The Xe^+ ion dose of $3.9 \times 10^{13} \text{ cm}^{-2}$ is the onset of the bcc nucleation. Only a very few bcc needles are seen with a typical length between few tens of nm to few hundred nm [Fig. 5.5(b)]. After a Xe^+ ion dose of $7.8 \times 10^{13} \text{ cm}^{-2}$, a slight increase in the bcc nucleation sites with the increase in the length and width of the already existing needles is observed [Fig. 5.5(c)]. With further ion irradiation of $1.2 \times 10^{14} \text{ cm}^{-2}$, a clear increase in the width of needles is noticed with a typical width of about tens of nm [Fig. 5.5(d)]. At a dose of $1.56 \times 10^{14} \text{ cm}^{-2}$ the bcc needles are seen to grow and merge and at $1.95 \times 10^{14} \text{ cm}^{-2}$ ion dose, most of the film is observed to be transformed as shown in Fig. 5.5(e-f).

The structural evolution of the as-prepared 8 ML fcc Fe film [Fig. 5.6(a)], irradiated with 3 keV Ar^+ ions are presented by STM. At an Ar^+ ion dose of $1.9 \times 10^{14} \text{ cm}^{-2}$, rare bcc needles could be observed. One such bcc needle with a length of few hundred nm and width of few nm is shown in [Fig. 5.6(b)]. After an Ar^+ ion irradiation of $4.7 \times 10^{14} \text{ cm}^{-2}$, few wide bcc needles could be identified [Fig. 5.6(c)]. And at ion dose of $9.5 \times 10^{14} \text{ cm}^{-2}$, the bcc needles are hardly visible due to increased roughness due to prolonged irradiation. Even at this poor image quality, we can recognize bcc areas as few wide interconnected features [Fig. 5.6(d)].

Fig. 5.7 shows the structural evolution of the as-prepared 8 ML fcc Fe film (a) at 3 keV Xe^+ ions. At a Xe^+ ion dose of $5 \times 10^{13} \text{ cm}^{-2}$, few bcc needles are seen along the crystallographic directions $[011]$ and $[0\bar{1}1]$ on the surface [Fig. 5.7(b)]. With an increase in the Xe^+ ion dose to $7.8 \times 10^{13} \text{ cm}^{-2}$, there is slight increase in the length of needles [Fig. 5.7(c)]. Although at a dose of $1.1 \times 10^{14} \text{ cm}^{-2}$ Xe^+ ions, the increased surface roughness makes it hard to see clearly the bcc needles, elongated features parallel to the crystallographic directions can be easily recognized [Fig. 5.7(d)].

Fig. 5.8 shows ion irradiation of the as-prepared (a) 8 ML fcc Fe film at 2 keV Ne^+ ions. At an ion dose of $1 \times 10^{15} \text{ cm}^{-2}$, with an increased surface corrugation no bcc needles could be recognized [Fig. 5.8(b)]. With an increased ion dose of $2 \times 10^{15} \text{ cm}^{-2}$, the surface roughness further increases. Only careful inspection reveals very few linear features, which are bcc needles as shown in Fig. 5.8(c).

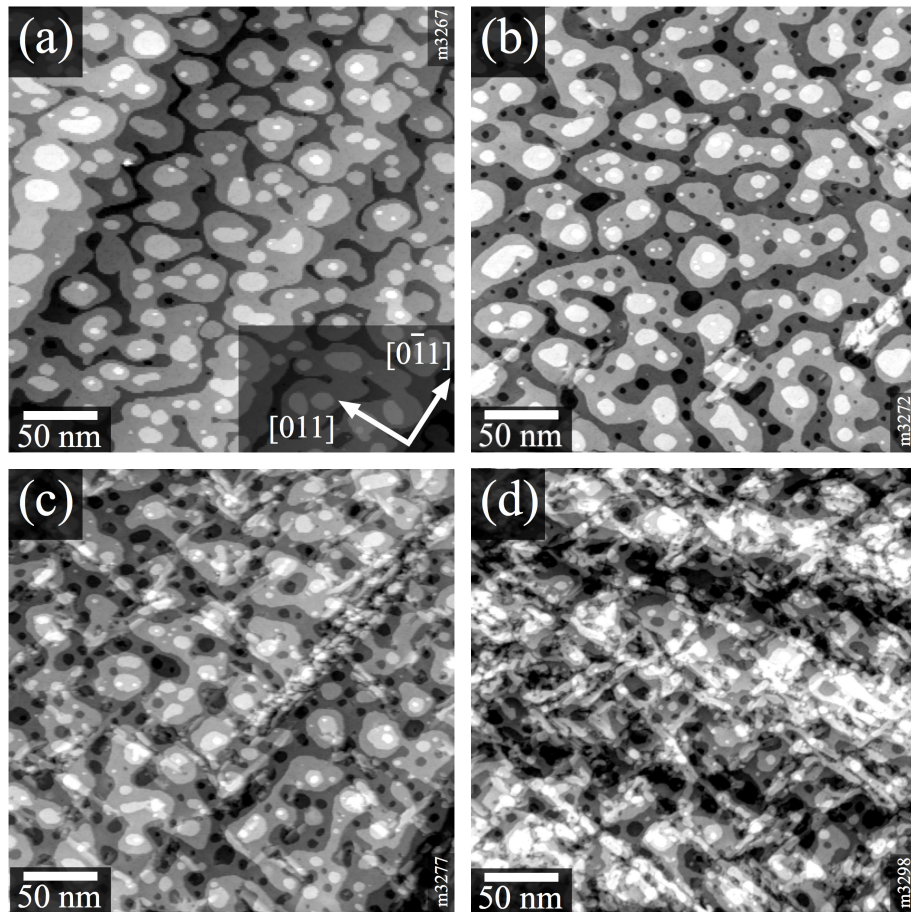


Figure 5.4: STM images of 8 ML fcc Fe film irradiated with 500 eV Ar^+ ion energy with doses of: (a) as-prepared film, (b) $2.3 \times 10^{14} \text{ cm}^{-2}$ (c) $4.5 \times 10^{14} \text{ cm}^{-2}$, (d) $6.8 \times 10^{14} \text{ cm}^{-2}$.

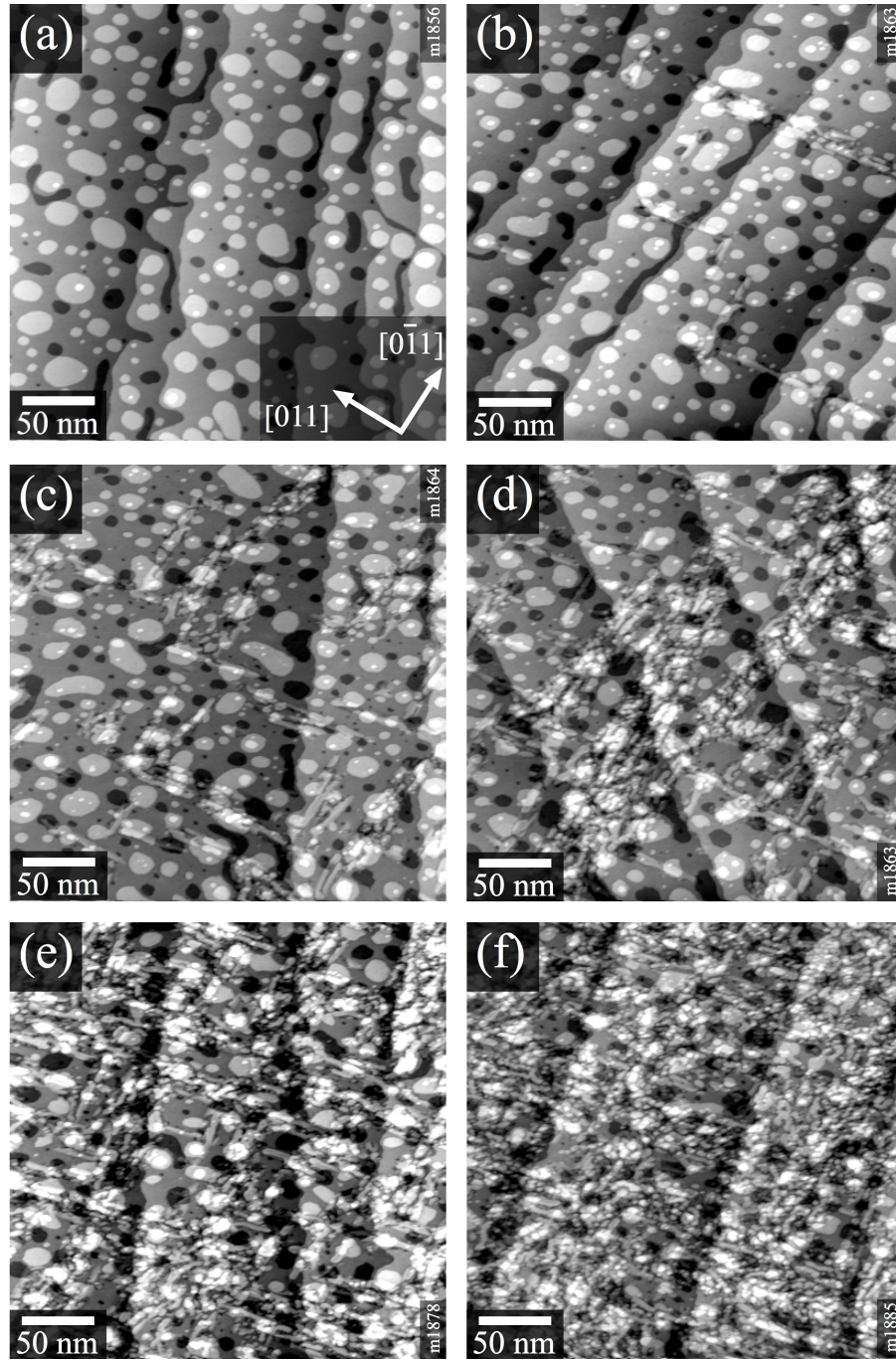


Figure 5.5: STM images of 8 ML fcc Fe film irradiated with 500 eV Xe⁺ ion energy with doses of (a) as-prepared film, (b) $3.9 \times 10^{13} \text{ cm}^{-2}$, (c) $7.8 \times 10^{13} \text{ cm}^{-2}$, (d) $1.2 \times 10^{14} \text{ cm}^{-2}$, (e) $1.56 \times 10^{14} \text{ cm}^{-2}$, (f) $1.95 \times 10^{14} \text{ cm}^{-2}$.

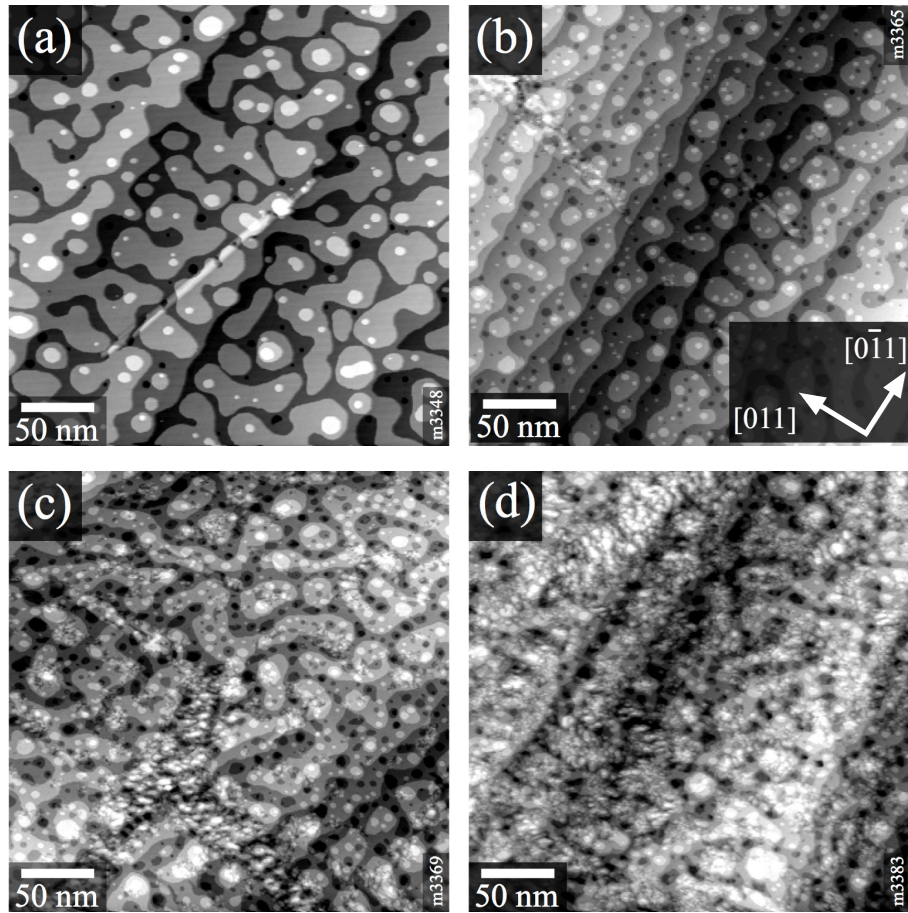


Figure 5.6: STM images of 8 ML fcc Fe film (a) irradiated with 3 keV Ar^+ ion energy with doses of: (b) $1.9 \times 10^{14} \text{ cm}^{-2}$, (c) $4.7 \times 10^{14} \text{ cm}^{-2}$, (d) $9.5 \times 10^{14} \text{ cm}^{-2}$.

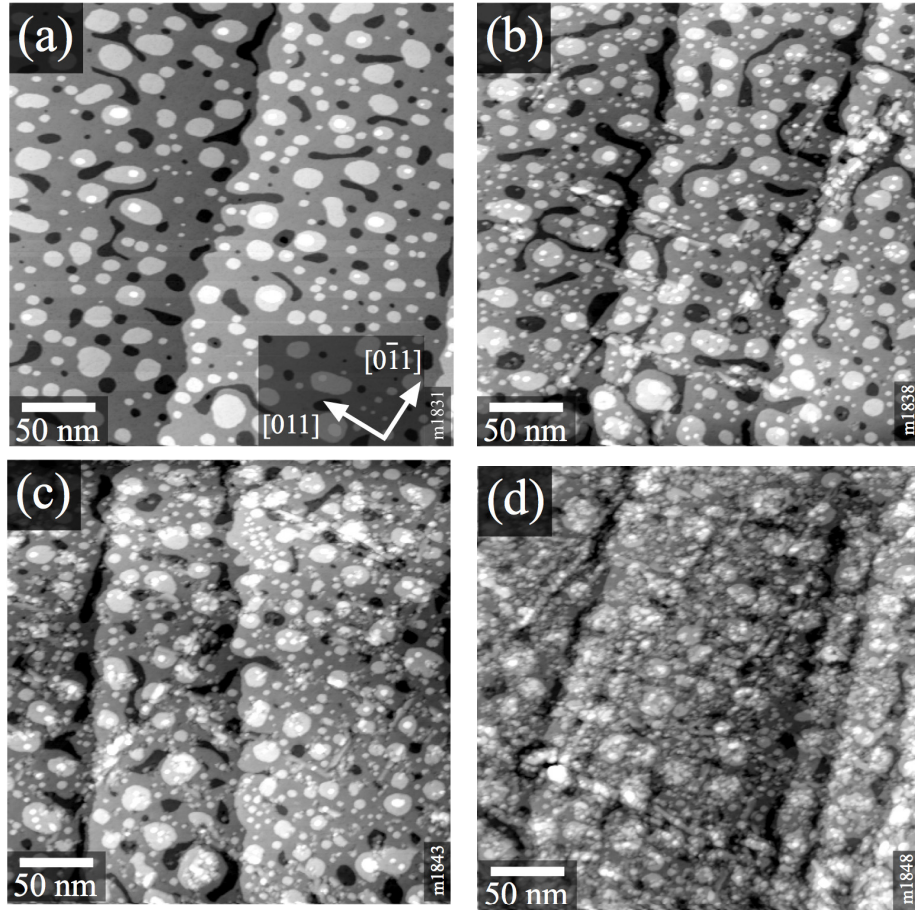


Figure 5.7: STM images of 8 ML fcc Fe film irradiated with 3 keV Xe^+ ion energy with doses of (a) as-prepared film, (b) $5 \times 10^{13} \text{ cm}^{-2}$, (c) $7.8 \times 10^{13} \text{ cm}^{-2}$, (d) $1.1 \times 10^{14} \text{ cm}^{-2}$.

5.4 Discussion

The absence of a transformation for the 8 ML fcc Fe films with He^+ ions at different energies can be explained as following: He^+ ions being the lightest lose all their energy to Cu-substrate, therefore, hardly any collision takes place in the Fe film which could be due to larger penetration depths for He^+ ions. This agrees well with the SRIM calculation, which shows negligible fraction of Fe atoms in the melt [see Fig. 5.1(a)].

For all ellipticity curves in Fig. 5.2, the initial rise is obviously proportional to the increased magnetism in the Fe films due to $\text{fcc} \rightarrow \text{bcc}$ transformation; increase in the number/size of bcc needles (ferromagnetic) contributes to the increased ellipticity signal. Almost all efficient ions show the saturation ellipticity value close to $\sim 150 \mu\text{rad}$, indicating complete transformation of 8 ML Fe films. The removal of Fe layers after prolonged irradiation

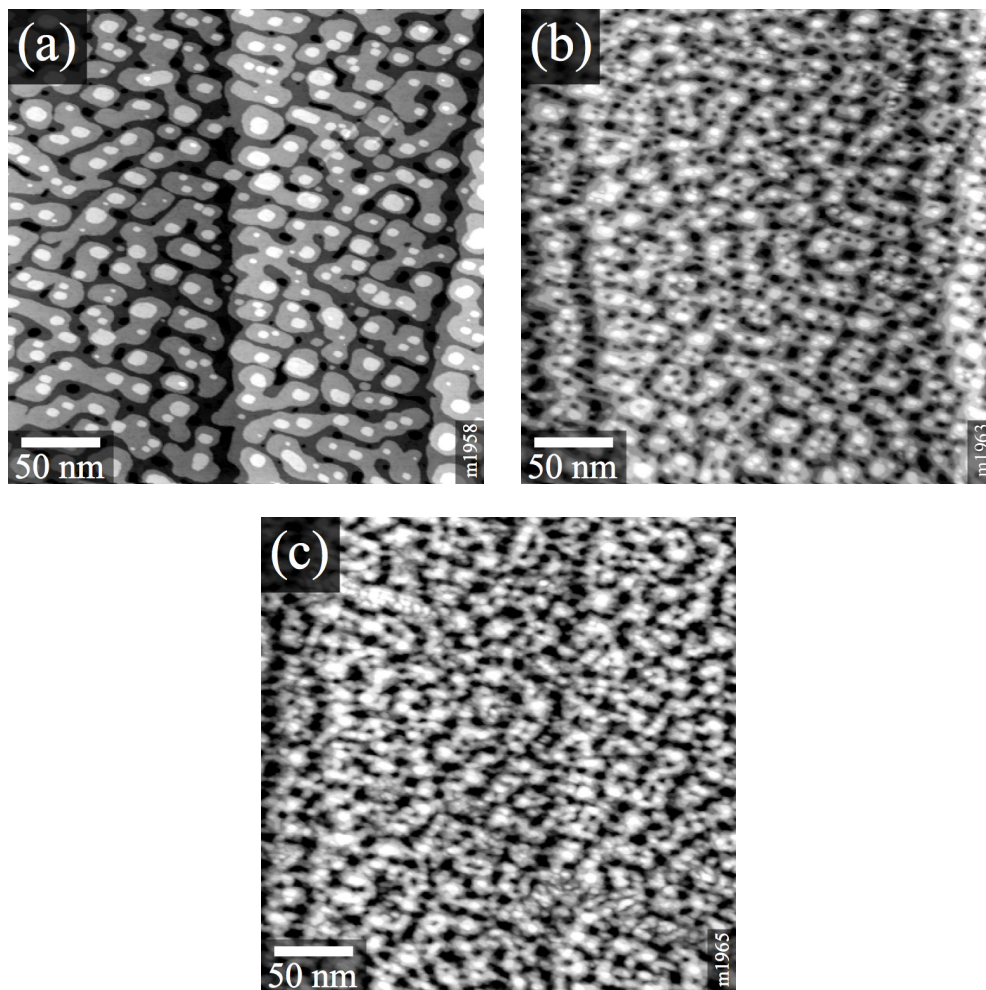


Figure 5.8: STM images of 8 ML fcc Fe film irradiated with 2 keV Ne^+ ion energy with doses of (a) as-prepared film, (b) $1 \times 10^{15} \text{ cm}^{-2}$, (c) $2 \times 10^{15} \text{ cm}^{-2}$.

with ions after reaching the maximum saturation value results in a decreasing trend in saturation magnetization.

The high value of the coercive field H_c [Fig. 5.2] at the threshold ion dose for all noble gas ions can be explained by magnetically decoupled needles which are separate to one another, with a large length-to-width ratio as already explained by Rupp et al. in Ref. [64]. These needles may have some anisotropy due to residual strain. As these bcc needles grow in size and become connected with increase ion dose, result in the decrease in coercive field value with increase in ion dose.

The following relationships can be established by comparing the SMOKE experimental results [Fig. 5.2] and SRIM calculations [Fig. 5.1]:

The best transformation results obtained for Ne^+ ions were at 500 eV ion energy which agree well with the SRIM prediction [cf. Fig. 5.2(a) and Fig. 5.1(b)]. In Fig. 5.1(b), we see that at 500 eV ion energy, most of the Ne^+ ions lose their energy to the Fe atoms, hence inducing the fcc-bcc transformation. For Ar^+ ions, this energy was found to be 1 keV (well below the crossing point) again in agreement with SRIM predication [cf. Fig. 5.2(b) and Fig. 5.1(c)].

For heavier ions i.e., Kr^+ and Xe^+ ions, the SMOKE measurements show best transformation curves at 5 keV and 1 keV respectively. For both ions, one expects the best transformation energy to be below and close to crossing point, as was with lighter gases. But 5 keV energy for Kr^+ is higher than the crossing point (4 keV), whereas 1 keV for Xe^+ ions is very low then 5.5 keV. One can explain this inconsistency by keeping in consideration the experimental scatter for these measurements [cf. Fig. 5.2(c,d) and Fig. 5.1(d,e)]. It is well known that these films at a thickness of ≈ 10 ML are transformed to bcc (so we are already close to the transformation limit) [63]. As we prepare 8 ML (± 0.5 ML) metastable fcc Fe films, therefore, slight increase/or decrease (say 7.5 ML or 8.5 ML) in the thickness of the fcc Fe films may have pronounced effect on the fcc-to-bcc transformation. Also there might be small impurities in the Fe films which may additionally contribute to this deviation.

For Ne^+ and Ar^+ ion irradiation, distinct transformation curves with gradual rise in ellipticity values are observed at different ion energies whereas for heavier gases i.e. Kr^+ and Xe^+ ions, we observe steep rise in ellipticity with same saturation value for almost all energies [Fig. 5.2]. This can be explained as following:

The energy deposition in the Fe films is much faster for heavier ions due to higher nuclear stopping (larger size of penetration depths) [90], which results in larger number of thermal spikes during ion irradiation (one may explain it, each ion-impact creates one thermal spike). Hence, resulting in increased probability to form bcc nuclei in the fcc Fe film. As the lighter ions have deeper ion penetration depths, they lose their energy by collisions on the way through the Fe film before coming to rest. Hence, these ions do not provide enough energy to Fe atoms to initiate transformation. This low probability for bcc nucleation for lighter ions prevails with increasing ion dose at a particular ion energy, hence resulting in gradual rise in magnetic signal. And the high probability for bcc nucleation for heavier ions results in steep magnetization. Above the crossing point (1 keV for Ne and 2 keV for Ar) for lighter gases, most of these ions reach the Fe-Cu interface, causing intermixing which results in reduction of the ellipticity signal. For Ne^+ and Ar^+ ions, at 3 keV the ellipticity signal is very low due to high penetration of ions, hence imparting all energy to Cu substrate [cf. Fig. 5.1 and 5.2].

Comparing the fastest transformation curves of Ne^+ with those of Ar^+ , Kr^+ and Xe^+ bombardment, we see that more dose is required for full transformation of the Fe film with Ne^+ ion irradiation at 500 eV as compared to Ar^+ , Kr^+ and Xe^+ ions [Fig. 5.2]. This dose is only $\sim 4 \times 10^{14}$ ions/cm² for Ar^+ (1 keV), $\sim 2 \times 10^{14}$ ions/cm² for Kr^+ (5 keV) and Xe^+ (1 keV) ions. This could be explained using the same reasoning as presented above,

i.e. due to low probability for bcc nucleation for Ne^+ ions, more dose is required to carry out complete transformation of film than required for the heavier ions (i.e. Ar^+ , Kr^+ and Xe^+).

For heavier ions (Kr^+ and Xe^+) at higher energies (above 1 keV) high transformation efficiency is observed (see Fig. 5.2), whereas the SRIM calculations show considerable fraction of Cu in the melt at these energies which should impede the transformation, i.e., the transformation efficiency should be low (see Fig. 5.1). Also for Kr^+ ions at 5 keV, we observe the best transformation curve whereas the SRIM calculations at this energy indicate larger fraction of Cu than Fe in the melt. Thus, according to SRIM we should not expect efficient transformation, but SMOKE measurements show otherwise. This discrepancy indicates that either the SRIM calculations are less reliable for heavier ions at higher energies (may be some additional parameters are required for better accuracy for heavier ions, because for lighter ions the SRIM results and SMOKE data are in good agreement) or there might be some influence of experimental scatter in the SMOKE measurements.

Comparing the STM images for Ar^+ and Xe^+ ions for 500 eV, we can clearly see that Xe ions are more efficient than Ar ions [cf. Fig. 5.4 and Fig. 5.5]. This could be explained as: Xe^+ ions being heavier in mass face higher nuclear stopping than lighter ions [90, 91], and deposit large energies to the target Fe atoms, eventually resulting in increased number of bcc nuclei. This general trend of higher efficiency for heavier ions is also supported by SMOKE measurements, where Xe^+ ions are seen to be most efficient for 500 eV [see Fig. 5.3(a)].

In Fig. 5.5, for Xe^+ ions at an ion dose of $1.95 \times 10^{14} \text{ cm}^{-2}$ more than $\approx 70\%$ of the film is transformed which looks close to the value seen in Fig. 5.3(a). And for Ar^+ ions at an ion dose of $6.8 \times 10^{14} \text{ cm}^{-2}$, it is almost $\approx 65\text{--}70\%$ which is lower than the one in Fig. 5.3(a). This difference in the STM and SMOKE data for Ar^+ ions can be explained on the basis of experimental scatter of the measurements explained above. Also, it should be noted that two different chambers were used for these measurements. Therefore, the residual gas pressure may also effect the results, i.e., during Fe evaporation some impurities from the residual gas got incorporated in the film and hence result in deviation in measurements.

Comparing Ar^+ and Xe^+ ions for 3 keV ion energy, STM images suggest better transformation with Xe^+ ions [cf. Fig. 5.6 and Fig. 5.7]. At 3 keV ion energy, Xe^+ ions impart more energy to the Fe film, resulting in increased efficiency in forming bcc nuclei, in agreement with SMOKE data [Fig. 5.3(c)]. For Xe^+ ions STM images show increase in ion dose, results in increasing bcc area in the film [see Fig. 5.7(b,c)]. At Xe^+ ion dose of $1.1 \times 10^{14} \text{ cm}^{-2}$, few long bcc needles are better visible [see Fig. 5.7(d)]. On closer inspection, we could also identify faint linear features parallel to the crystallographic directions $[011]$ and $[0\bar{1}1]$ which indicate bcc needles, hardly visible due to high surface corrugation for Xe^+ ion at 3 keV. At this dose the bcc area is obviously higher than for Ar^+ ions at $9.5 \times 10^{14} \text{ cm}^{-2}$ at 3 keV [cf. Fig. 5.6(d) and Fig. 5.7(d)]. At the Xe^+ ion dose of $1.1 \times 10^{14} \text{ cm}^{-2}$, the transformed bcc area (although very difficult) could be roughly estimated to be $\approx 50\%$, which is in agreement to the SMOKE data shown in Fig. 5.3(c). Analyzing

the STM images for Ar^+ ions show that very few wide bcc needles at a dose of $4.7 \times 10^{14} \text{ cm}^{-2}$ could be seen, one such bcc needle is shown in Fig. 5.6(c). Although further ion irradiation makes the surface quite rough, but still one can recognize no prominent change in bcc areas as shown in Fig. 5.6(d). This poor efficiency for Ar^+ ions is understood as a consequence of Fe-Cu intermixing at high energies, hence impeding the transformation for lighter ions at high energies. Thus, at 3 keV, Ar^+ ions lose almost all energy to the Cu substrate. This is in agreement to the SMOKE data [see Fig. 5.3(c)], where Ar ions at 3 keV are least efficient in carrying out transformation.

Comparing the data for Xe^+ ions at 500 eV and 3 keV ion energy suggest better efficiency at 3 keV. STM images of Xe^+ ions at 500 eV show that almost $\approx 70\%$ of the film is transformed for ion dose of $1.95 \times 10^{14} \text{ cm}^{-2}$ and for 3 keV energy at $1.1 \times 10^{14} \text{ cm}^{-2}$ ion dose reveal $\approx 50\%$ transformation agreeing with SMOKE data [cf. Fig. 5.5(f), Fig. 5.7(d) and Fig. 5.3(a,c)]. The better efficiency of Xe^+ ions at high energy is due to the fact that at higher energy the Xe^+ ions have higher probability for bcc nucleation in comparison to lower energy.

Comparing the data for Ar^+ ions at 500 eV and 3 keV ion energy suggest better efficiency at 1 keV. STM images of Ar^+ ions at 500 eV show that almost $\approx 65\text{-}70\%$ of the film is transformed for ion dose of $6.8 \times 10^{14} \text{ cm}^{-2}$ and for 3 keV energy at $9.5 \times 10^{14} \text{ cm}^{-2}$ ion dose reveal only very few wide bcc features [cf. Fig. 5.4(d), Fig. 5.6(d) and Fig. 5.3(a,c)]. The better efficiency of Ar^+ ions at low energy is due to the fact that the sputter yield increases a lot with increasing ion energy [$Y = 1.1$ (500 eV) and $Y = 2.8$ (3 keV) [111, 112]], whereas the transformation efficiency does not.

STM images for Ne^+ ions at 2 keV show almost negligible transformation at a dose of $2 \times 10^{15} \text{ cm}^{-2}$ which agrees with the SMOKE data [cf. Fig. 5.8(c) and Fig. 5.2(a)]. This could be due to high penetration depths for lighter ions, which further increases for high energies. Hence, Ne^+ ions impart almost all energy to the Cu substrate. Also let's take a look at the AES signal for Fe film thickness with the ion dose to have a better insight. The Fe/Cu ratio [estimated from Auger-Peak-Height (APPH) of AES signal] is 471 (7.9 ML as grown). At an ion dose of $1 \times 10^{15} \text{ cm}^{-2}$, this ratio reduces to 308 (6.3 ML) and at $2 \times 10^{15} \text{ cm}^{-2}$, we have 212 (5 ML). Therefore, irradiation with Ne^+ ions at 2 keV suggest ≈ 3 ML removed by sputtering. At 2 keV with high sputtering yield ($Y = 1.7$ [111, 112]), Ne^+ ions sputter the Fe films with increasing ion dose.

5.4.1 Au coated 8-ML Fe films

In Ref. [64], 8-ML Fe films were coated with 2 nm (10-ML) Au and then taken to an MFM facility for nano-patterning. The questions which remained unaddressed were following: how does Au layers grow on the 8-ML Fe film? Is it possible to find any evidence for fcc-bcc transformation in Au coated Fe films by STM? Therefore, to explore these areas we conducted following experiment with Au coated Fe film.

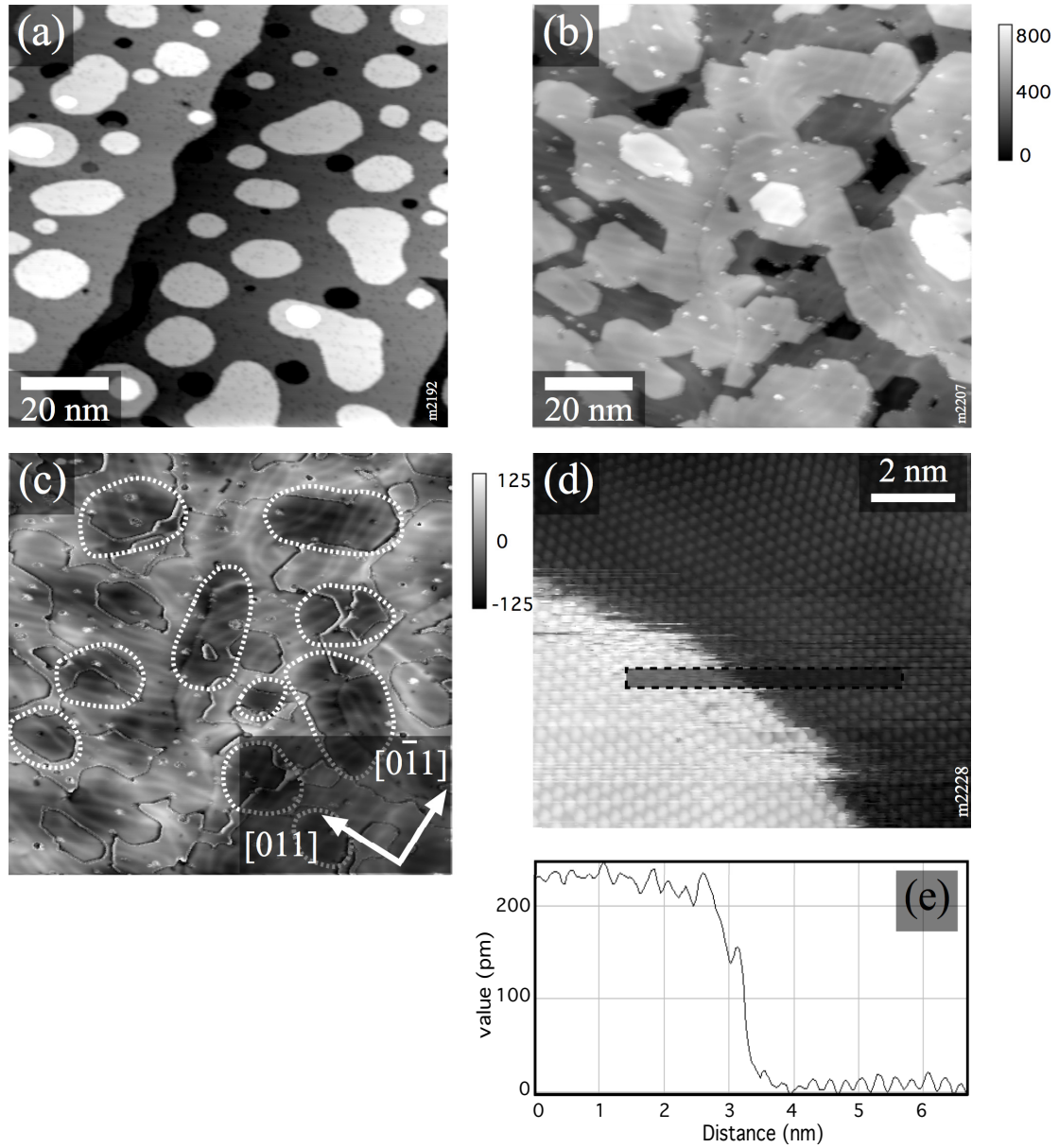


Figure 5.9: (a) STM image of the 8 ML Fe film, (b) Au coated 8 ML Fe film surface, (c) frame (b) after processing shows the underlying fcc islands marked by dotted ellipsoids as well as Au herringbone structures, (d) Atomically resolved Au surface showing Au(111), (e) the section profile over the marked area in (d) reveals a step height of ≈ 235 pm.

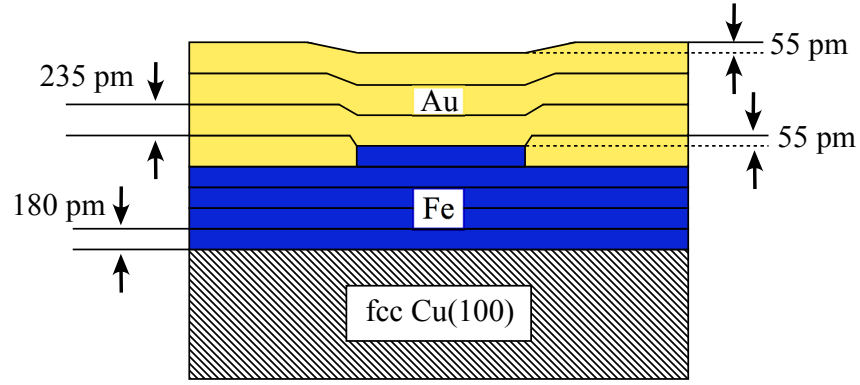


Figure 5.10: Schematic view of the Au layers on Fe/Cu(100) to show the underlying Fe islands. The difference of ~ 55 pm between Au and Fe layers is maintained up to the top Au layer.

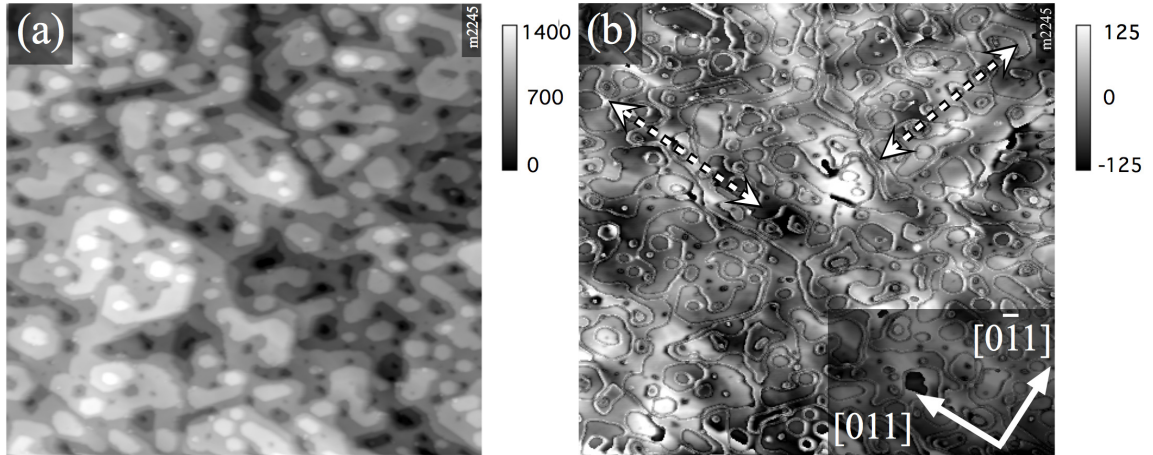


Figure 5.11: (a) STM image of the Au surface after Ar^+ ion dose of 3.5×10^{14} ions/cm² at 3 keV, (b) frame (a) after processing (Au layers and noise subtracted) shows stripes along the marked crystallographic directions, pointing towards the transformation of the Au coated Fe film.

The surface of 8 ML (1.4 nm) fcc Fe film grown on Cu(100) is shown in Fig. 5.9(a), showing a typical 8 ML fcc Fe surface with rounded islands and no bcc needles [64]. Fig. 5.9(b) shows the surface of the Fe film coated with 2 nm Au [corresponding to ≈ 10 ML Au(111)]. The STM image reveals layer-by-layer growth. Atomically resolved image shows that Au grows with Au(111) reconstruction on Fe (Fig. 5.9(d)), the Au step height corresponds to that of Au(111), i.e., 235 pm [Fig. 5.9(e)].

Fig. 5.9(c) is the same (b) with image processing (Au layers and noise subtracted). Looking carefully, we can easily recognize the ellipsoidal structures marked by dotted lines in 5.9(c). They can be easily related to the underlying fcc Fe(100) islands, which were almost impossible to detect in the unprocessed image. This can be understood with the help of the following Fig. 5.10, which shows a schematic view of the Au layers (235 pm) growing on the Fe island (180 pm). The first Au layer grows side by side with the Fe island and has a sharp step edge between the Fe and Au surfaces with a difference of 55 pm. This sharp edge smoothens out with increasing number of Au layers, but still maintains the same height difference. This difference maintained up to the top Au layer is detected as a dark patch in STM which could be realized only in processed images as shown in Fig. 5.9(c).

As the Au(111) exhibits a threefold symmetry with equal probability. Thus the regions between different reconstructions form domain boundaries and also the so called herringbone structure for Au(111) [114] are clearly seen in Fig. 5.9(c). These herringbone structures are quite sensitive to defects like e.g. step edges.

Now this Au coated 8-ML Fe film is exposed to Ar^+ ion irradiation with a dose of 3.5×10^{14} ions/cm² at 3 keV. STM images show a sputtered surface as seen in Fig. 5.11(a), with no atomic resolution possible on such a rough surface. After employing image processing (Au layers and noise subtracted) to this image, bright stripes parallel to the crystallographic directions [011] and $[0\bar{1}1]$ can be distinguished in the image [see Fig. 5.11(b)]. As the bcc needles in 8-ML fcc Fe films are oriented along the crystallographic directions [011] and $[0\bar{1}1]$, we can state with confidence that although the surface of the Au coated film gives no direct information about the transformation of the underlying Fe film after Ar^+ ion irradiation, but the appearance of bright stripes after image processing is a clear indication of such a transformation (cf. Fig. 5.11(b) and Fig. 5.4(d)).

Also, the 3 keV Ar^+ ion energy used to carry out the transformation is lower than the Fe-Cu intermixing limit (in accordance with SRIM calculation, see Fig. 5.12). Fig. 5.12 shows the number of atoms N_m in the molten volume for a 1.4 nm Fe film coated with 2 nm Au. This experiment not only presents the structure of Au film but also suggests the underlying transformation of the Au coated Fe film which was hard to detect in thicker (22 ML) film due to surface roughness both before and after ion irradiation [cf. Fig. 5.11 and Fig. 6.17].

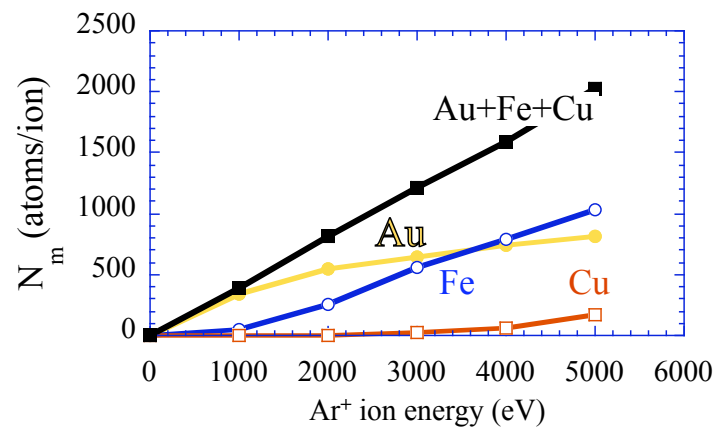


Figure 5.12: Calculated number of atoms N_m in the molten volume for a 1.4 nm Fe film coated with 2 nm Au. The fraction of Cu atoms in the melt is negligible up to 1 keV and increases with the increasing ion energy.

Chapter 6

CO-stabilized 22 ML Fe films on Cu(100)

6.1 Introduction

Although studying the behavior and response of thicker films is interesting enough. However, for some applications like in magnetic flux guides (yokes of an electromagnet etc.), the films must be thick so that the integrated flux is high enough (see [64]). Therefore, we desire to grow fcc Fe films thicker than 8 ML. For our studies, we selected a thickness of 22 ML (4-nm) to be grown on Cu(100). This chapter gives a complete in detail study of the stability and growth of these thicker fcc Fe films. The mechanism behind the ion-beam induced transformation (fcc \rightarrow bcc) of these films is discussed.

These films were prepared in two different UHV systems. For structural properties of 22 ML fcc Fe films, the RT-STM (section 4.2.1) was used for carrying out STM, LEED, and AES, whereas we used the SMOKE set-up for magnetic measurements (section 4.2.3). The film preparation method was same for both chambers. Finally, for conducting the nano-patterning on these metastable films, the set up is described in (section 4.2.2).

6.2 Film growth and stability factors

In this section we present an in detail view of the growth and factors contributing to the stability of the 22 ML fcc Fe film.

As mentioned earlier in section 4.2.3, Fe films on Cu(100) grow with an fcc structure only below 10 ML, and above that it attains the bcc phase at RT. So, primarily we need an additive in the Fe film which may stabilize the fcc phase for thickness larger than 10 ML. At this point, literature review on this subject suggested many possibilities. Based on investigations by STM, LEED and MEED, it was reported that up to 60 ML of the metastable fcc Fe film can be grown [47, 48]. In these articles Kirilyuk et al. reports that such films can be obtained by growth in the presence of gases containing carbon like methane (CH_4), ethylene (C_2H_4), acetylene (C_2H_2), CO and their combinations. Therefore, we selected one of the described methods, introducing CO in the chamber at a fixed background pressure during evaporation of the Fe films [47, 48]. It turned out that the correct value of the CO pressure is very important as it is the key stabilizing parameter, and the exact value seems to depend on details of the vacuum chamber (possibly related to the different pressure gauge, geometries of the gas valves, and sample). Therefore it was necessary to optimize the value of the CO pressure for obtaining a stable fcc Fe film for our setup. For that purpose, we conducted a series of experiments at different CO pressures. For experiments conducted in RT-STM system, we got the best results with 7.5×10^{-10} mbar, and for SMOKE system we found that 3×10^{-9} mbar CO was suitable for growing a 22-ML thick fcc Fe film.

Fig. 6.1 presents a graph that offers a clear explanation of the growth process in the presence of CO. Here, the concentrations of oxygen and carbon in the fcc Fe film are plotted as a function of different CO pressures during evaporation (Data taken from the RT-STM system). We found that with increasing CO pressure during the film growth, the normalized Auger peak-to-peak height (APPH) signal of carbon $\text{C}_{273}/(\text{Fe}_{703}+\text{Cu}_{920})$ drops down, whereas the oxygen $\text{O}_{514}/(\text{Fe}_{703}+\text{Cu}_{920})$ signal is seen to rise. Also, at high CO pressures (above 2×10^{-9} mbar), STM shows that the film grows as bcc Fe i.e., the stabilizing agent is insufficient to hold the fcc structure. At lower CO pressures (below 1×10^{-9} mbar), the films are seen to grow with fcc Fe structure. This observation is in agreement with Ref. [48], which can be explained in the following way: During the growth of Fe films on Cu(100) in the presence of CO pressure, the CO molecules dissociate into carbon and oxygen atoms at the surface of the growing Fe film. The carbon atoms occupy the interstitial sites in the Fe lattice, and contribute to the bulk stability of the thicker fcc film. The oxygen atoms remain at the top of the film, and contribute to surface stability of the fcc lattice. This process ends when the oxygen coverage on the surface is high enough to block the adsorption and dissociation of CO molecules (see Fig. 6.2). If the CO pressure is too high, then CO dissociation/adsorption gets blocked before the desirable film thickness is achieved. This results in an Fe film with final layers having very low carbon concentration, too low to stabilize the fcc structure. Now, consider the same Fe evaporation rate as for the former case, if the CO pressure is too low, then the concentration of carbon atoms in the interstitial sites of the Fe lattice is too low in all layers. Therefore, the carbon atoms cannot sufficiently stabilize the fcc structure for thicker films. Hence, the film will again transform to bcc before the final thickness is reached. Thus, the optimum value of the CO pressure for the stability of fcc Fe film is just below the value that would lead to

saturation of the surface with oxygen at the end of the growth process.

For our experiments this value is found to be 7.5×10^{-10} mbar marked by an arrow showing ‘stable fcc’ in Fig. 6.1.

6.3 Surface morphology of 22 ML fcc Fe films

The surface morphology of the films is strongly related to the CO pressure as mentioned in the last section. Now we explore the surface structure with unstable CO pressure. If the CO pressure is outside the range which leads to the growth of homogeneous fcc Fe film, then bcc crystallites can be observed in the 22 ML fcc films. Fig. 6.3 shows the surface obtained in one such experiment, where the CO pressure of 7.5×10^{-10} mbar was not stable during film growth. This instability in the CO pressure could be due to slow response of the CO gas valve (a problem that was solved in the later experiments). We see that most of the film surface is fcc and rather flat showing layer-by-layer growth. The bcc areas are easily recognizable by their rough appearance and larger average height due to 5-10% larger interlayer distance of bcc Fe(110) compared to fcc Fe(100) [62, 64]. They have a wavy structure with lengths of typically few tens of nm to 100 nm and widths of ≈ 10 -20 nm. Figs. 6.3(b-d) provide higher magnification (zoom-in at the dotted area) of Fig. 6.3(a). The surface of the bcc area is quite rough compared to the fcc regions. In Fig. 6.3(d), oxygen atoms are present as dark spots on fcc Fe (better visible in Fig. 6.4), forming a $c(2 \times 2)$ lattice. Oxygen is disordered on the bcc areas.

In pure Fe films, the bcc structure nucleates in straight, narrow crystallites (“needles”) oriented along the $[011]$ and $[0\bar{1}1]$ directions; this is true for the spontaneous bcc needle formed during growth due to higher film thickness [62] as well as ion-induced transformation from fcc-to-bcc [64]. Here, we have carbon in the interstitial sites of Fe film offering bulk stability. We consider it very likely that carbon hinders the formation of straight needles in thicker films, thus the initial bcc nucleation site does not grow as a straight needle but takes a shape (wavy path) other than straight. This may be either due to a slightly inhomogeneous carbon concentration or due to carbon pileup in case that some carbon atoms diffuse out of the bcc regions into the more favorable fcc regions. Similarly, oxygen on the surface may also push the bcc needle away from straight line to wavy path. The flower-shaped bcc areas [e.g. at the right edge of Fig. 6.3(c)] must also be considered a consequence of carbon and/or oxygen as these shapes are not found on the clean films [64]. All these structures (bright) with wavy, flower like structures are bright bcc areas.

Besides the differently shaped bright bcc needles protruding from the fcc surface, we also find areas that are lower than the fcc surroundings. Fig. 6.3(e) shows an STM image including such an area (below the bright needle). A linescan across the trough and the needle (averaged over the frame) is shown in Fig. 6.3(f). These troughs have a typical width of ≈ 10 nm and can reach a depth of ≈ 0.5 nm below the fcc surface. They are

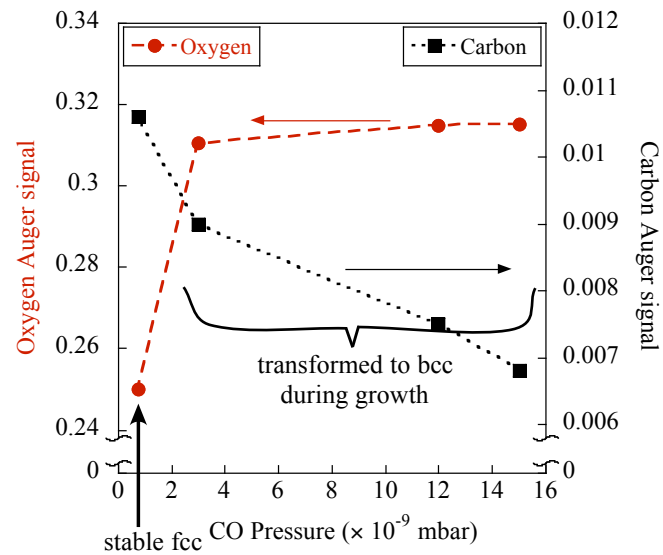


Figure 6.1: Normalized Auger peak-to-peak heights of carbon and oxygen signals for 22 ML Fe films as a function of CO pressure during evaporation for RT-STM.

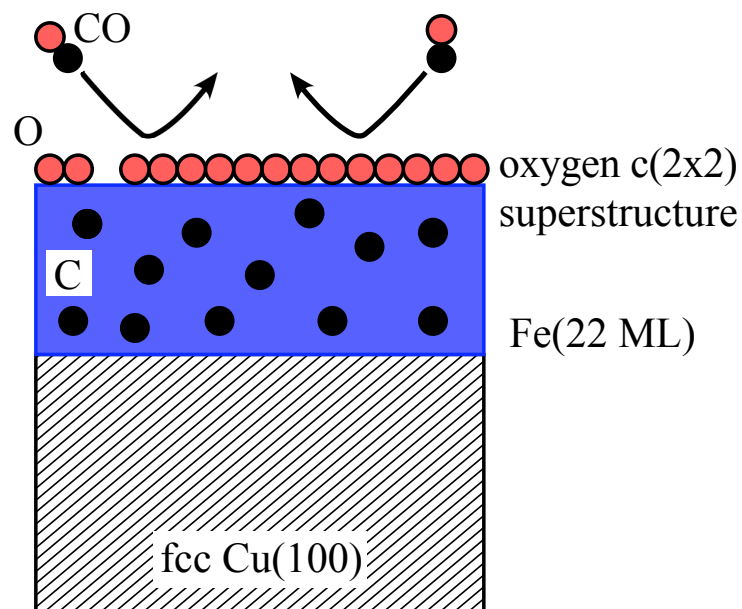


Figure 6.2: Schematic view of the film growth process in the presence of CO.

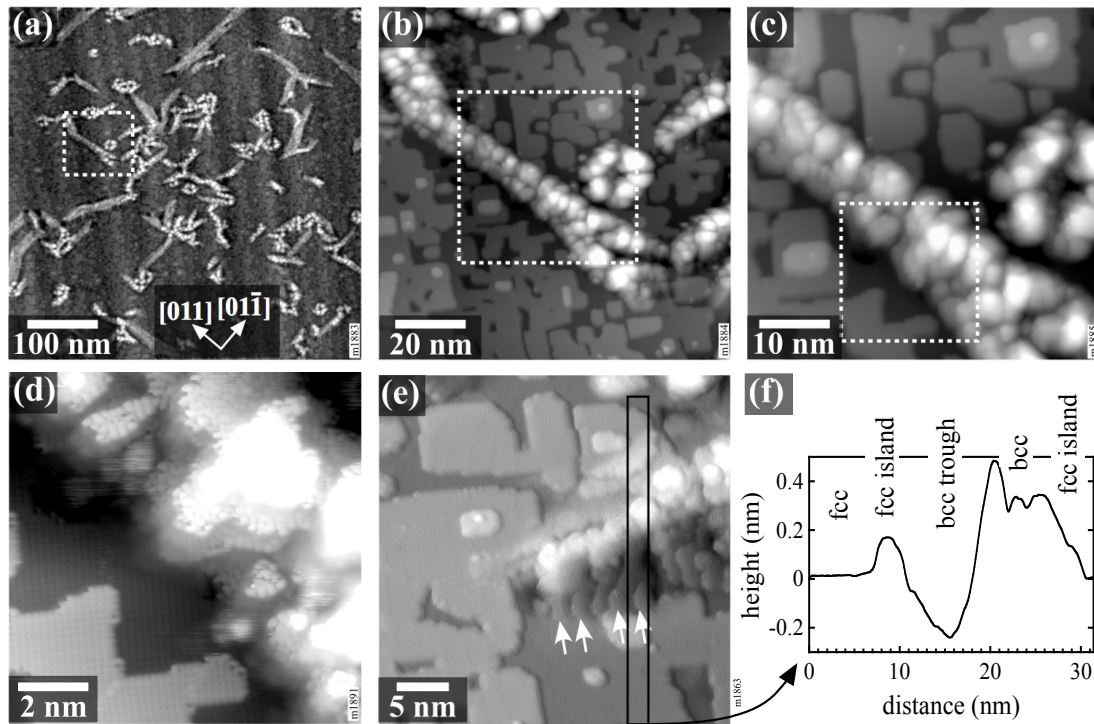


Figure 6.3: STM images of a 22 ML Fe film grown with unstable CO pressure during the experiment, leading to a surface with bcc crystallites (bright). Frames (a)-(d) show the same area with increasing magnification. (e) bcc area with an adjacent trough (image shown as if illuminated from the left). The inclined bcc wedges in the trough are indicated with arrows. The section profile (f) over the vertical frame in (e) shows the bcc trough next to the needle.

always found at the sides of bright (high) needles and characterized by elongated wedge-like terraces perpendicular to the needle direction. These terraces are tilted by angles between 3° and 5° marked by arrows in Fig. 6.3(e). This shape and tilt angle is a characteristic for the Pitsch orientation of bcc crystallites as reported by Kalki et al. [33]. In this orientation, one set of fcc{100} and bcc{110} planes are parallel to each other, and also one of the fcc<001> nearest neighbor directions matches a bcc<111> nearest neighbor direction in that plane. Therefore, also these troughs must be bcc areas, and, we can identify the similar dark areas adjacent to bright needles as bcc, even in images with lower resolution. In summary, 1. the bcc areas are found as bright bcc structures (different shapes) in thicker films and 2. the dark areas next to the bright bcc are also bcc.

The depth of these bcc troughs, lower than the fcc areas can be explained as follows: formation of a bcc needle attached to the fcc lattice at its sides is accompanied by tensile strain [39, 62]. To attain a relaxed state, the needle shrinks in width, deforming the fcc film on its sides. Obviously, the fcc film adjacent to the needle transforms to bcc due to the stress [7, 39, 47, 62] and due to the lateral expansion it has to reduce its height. The atomic volume increases by only 3.5% by the fcc \rightarrow bcc transformation in the bcc regions next to the island, but the tensile strain of the needle amounts to 9% and 3% in the directions parallel and perpendicular to the needle, respectively. Thus we find an overall reduction of the height in the “trough” areas next to the bright bcc needles.

Fig. 6.4(a) shows the surface of a 22-ML-thick fcc Fe film grown with an optimized CO pressure of 7.5×10^{-10} mbar. We find almost perfect layer-by-layer growth with rectangular shaped islands rounded at their corners. This surface structure is slightly different from the surface of 8 ML films grown without CO shown in Fig. 6.4(b)(for reference), where the islands are larger and more circular. No bcc crystallites (needles) were observed in the as-prepared film; it means that the CO pressure and growth time perfectly matched to result in an fcc Fe film free of any bcc crystallites. The inset in Fig. 6.4(a) shows a $c(2 \times 2)$ superstructure of oxygen on fcc Fe, with the primitive superstructure cell highlighted by a white square. The white spot (marked by a white circle) in the inset is probably a missing oxygen atom.

One interesting feature related to the shape of the islands (comparing 22 ML and 8 ML) is the fact that the steps of the 22 ML film grown in CO are not aligned in the close-packed <011> directions, but rather along <010>. This must be seen as a consequence of the $c(2 \times 2)$ oxygen overlayer, which obviously stabilizes the steps running parallel to the oxygen rows. Fig. 6.5 shows the structure model for the Fe steps grown in the CO. The uppermost Fe atoms (grey) orient parallel to oxygen rows, hence along <010> directions. Not every island edge strictly follows the <010> directions which could be due to absent oxygen atoms in that surface, but the majority of the islands do follow this pattern.

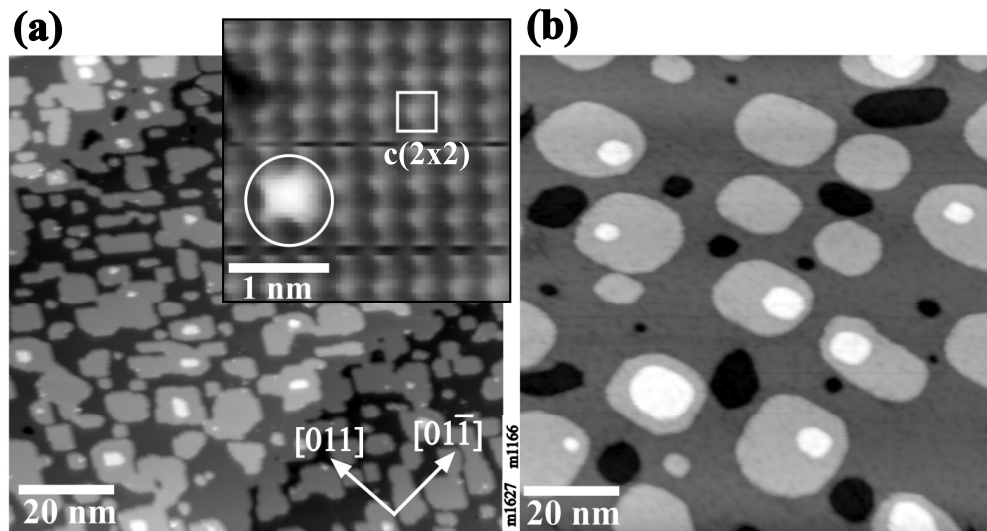


Figure 6.4: STM image of the as-grown 22 ML Fe film in the presence of CO. (a) The inset shows the oxygen $c(2 \times 2)$ superstructure highlighted by a white square. The white spot in the inset is probably the missing oxygen atom (white circle). (b) The surface of an 8 ML Fe film grown without CO (shown here for comparison)

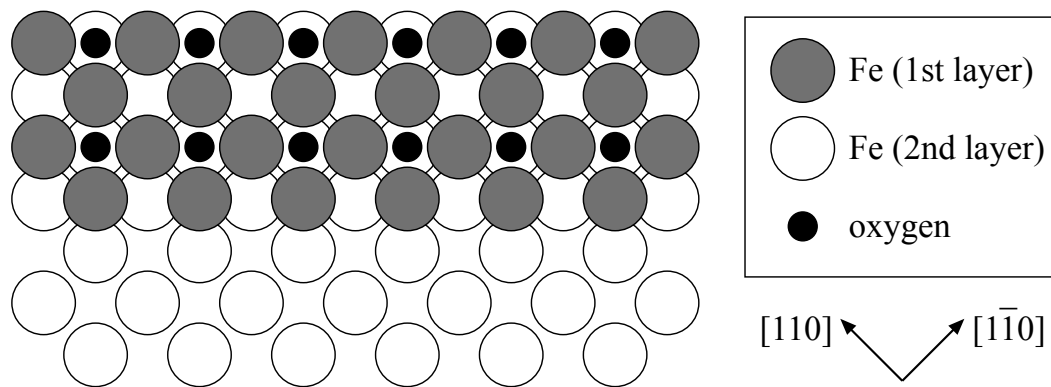


Figure 6.5: Structure model for the Fe steps of the films grown in CO (top view). The $c(2 \times 2)$ oxygen superstructure is shown only in the upper layer.

6.4 oxygen removal

As we mentioned in section 6.2, carbon and oxygen both are important for the overall stability of the fcc Fe films. We pointed out the effect of too high or too low a CO pressure during film growth on the carbon, without emphasizing the contribution of oxygen. Therefore, we planned an experiment to remove oxygen from the surface of the 22 ML fcc Fe film. For this we used atomic hydrogen to remove surface oxygen without ion bombardment. We prepared a slightly thicker Fe film in CO, with a thickness of 23-24 ML according to the AES (quantification was based on the average AES signals of 22-ML films and the decay of the copper signal with film thickness calculated with the SESSA code) [91]. The slightly larger thickness was chosen to increase the sensitivity towards any factors promoting the fcc to bcc transformation (because a slightly thicker film would react much strongly as the film is already at the verge of collapsing to bcc). Fig. 6.6(a) shows the STM image of the as-grown fcc film, which is already partially transformed, thus really at the stability limit of fcc films. This surface shows long bcc crystallites covering about 50% of the surface. The initial $O_{514}/(Fe_{703}+Cu_{920})$ APPH ratio was 0.34 which is roughly the same as for all the films, hence the surface has a closed $c(2 \times 2)$ overlayer. Oxygen was removed by exposing the fcc Fe surface to atomic hydrogen using a hot-tube gas cracker. We have used a pressure of 2×10^{-6} mbar H_2 for 1 hour and a heating power of 55 W, which should correspond to a dose of atomic hydrogen of $> 10^{18} \text{ cm}^{-2}$. After dosing atomic H, the AES signal shows an APPH ratio of $O_{514}/(Fe_{703}+Cu_{920})$ of 0.06, i.e., more than 80% of the initial oxygen was removed from the surface. The STM image in Fig. 6.6(b) shows the surface of the film after oxygen removal. The transformed area has now increased to $\approx 90\%$. Still some untransformed patches of $\approx 100 \text{ nm}$ size can be seen. It is interesting to know that this transformation occurs only by removal of oxygen from the surface due to adsorption of hydrogen. In this experiment, we cannot exclude some influence of energetic ions created in the gas cracker and accelerated onto the surface (the hot tube is at +1 kV). As the effect of hydrogen destabilizing the fcc structure must be considered rather small (cf. Refs. [58] and [60]), this experiment confirms the role of oxygen on the surface for the stability of the thick fcc Fe films, but it also allows us to compare the effect of oxygen removal with other ion-induced effects. Anyhow, we can securely state that for growing thicker fcc Fe films both oxygen and carbon are equally important.

Finally, we should note that a surface like that in Fig. 6.3 will still exhibit strong oscillations of the diffraction signals during growth, thus it would be still considered an fcc surface in MEED (medium-energy electron diffraction) experiments like those performed in Refs. [47, 48]. Nevertheless, such a surface already containing (ferromagnetic) bcc nuclei as in Fig. 6.3 is not useful for nanopatterning, because a regular pattern cannot be obtained if the film has spontaneously transformed bcc areas, which are randomly distributed in the film. This means that the practical limit of the Fe thickness for such experiments is somewhere around the 22 ML thickness which is studied in this work, not at 30-35 ML, where the oscillations indicating growth of fcc Fe stabilized by CO die out [47, 48].

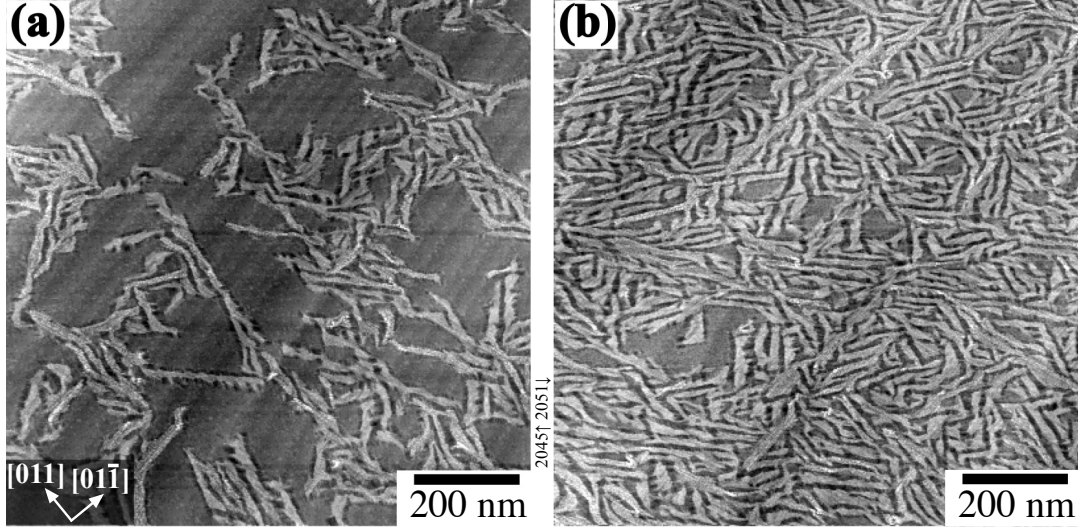


Figure 6.6: Fe film (≈ 23 to 24 ML) grown in CO. (a) STM image of the as-grown surface with partially transformed areas (bright). (b) After dosing atomic hydrogen to remove the surface oxygen.

6.5 Ion beam induced Transformation

Now we present the results obtained due to structural change of the 22-ML-fcc Fe films by Ar^+ ion irradiation; using the STM and LEED measurements.

6.5.1 STM

Fig. 6.7 shows the surface transformation of a 22 ML fcc Fe film prepared in 7.5×10^{-10} mbar CO after bombardment with Ar^+ ions at 500 eV. The as-grown film surface showed the fcc structure, having rectangular shaped islands, and no bcc areas over a large scan area as shown in inset of Fig. 6.7(a). This film is then irradiated with an Ar^+ ion dose of 1.3×10^{15} ions cm^{-2} . At this dose, bcc crystallites start appearing on the fcc film surface [Fig. 6.7(b)]. As mentioned above, this can be easily recognized due to the fact that the bcc regions appear brighter than the rest of the surface because of the larger interlayer distance. The bcc regions are typically 100-200 nm long and 10-25 nm wide. There are only a very few sites where the fcc-to-bcc transformation has nucleated, and the transformation spreads out from these sites, which is similar to the results for ion bombardment of clean 8-ML Fe films [64]. Zooming in on the surface shows slightly increased roughness also in the untransformed areas because the surface was sputtered [compare inset of Fig. 6.7(a) and Fig. 6.7(b)]. Again exposing this slightly transformed film to further ion irradiation, we find

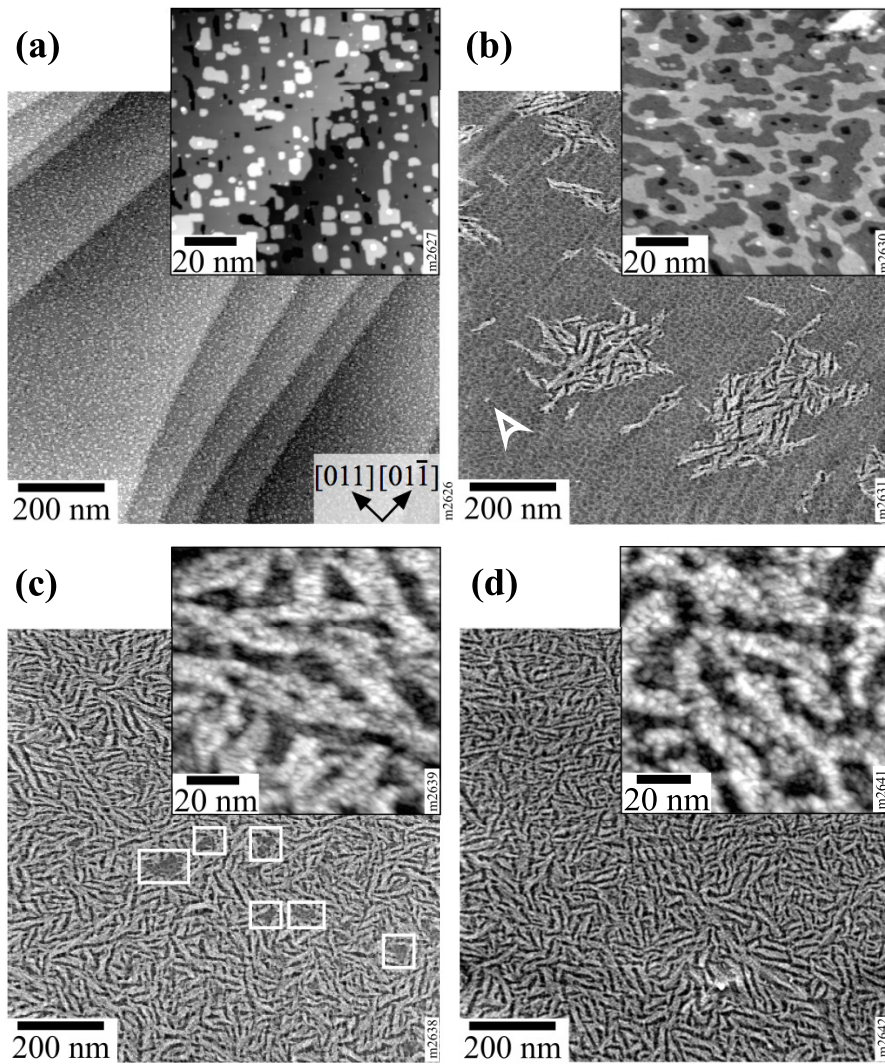


Figure 6.7: STM images of a 22 ML Fe film prepared in 7.5×10^{-10} mbar CO. (a) as-grown film, and after 500 eV Ar^+ ion irradiation with ion doses of (b) $1.3 \times 10^{15} \text{ cm}^{-2}$, (c) $1.8 \times 10^{15} \text{ cm}^{-2}$, and (d) $2.4 \times 10^{15} \text{ cm}^{-2}$. Overview images (b)-(d) are high-passfiltered to make the bcc needles more visible in spite of steps in the substrate.

that at an Ar^+ ion dose of 1.8×10^{15} ions cm^{-2} , most of the film surface gets transformed with wavy bcc needles shown in Fig. 6.7(c). Only a few regions wider than 50-100 nm remain untransformed (marked with white boxes for visual guidance). A magnification of the transformed regions in the inset of Fig. 6.7(c) shows randomly oriented bcc needles (wavy) with the surrounding areas quite rough. With further irradiation of this film, at an ion Ar^+ dose of 2.4×10^{15} cm^{-2} , the fcc to bcc transformation reaches saturation, as shown in Fig. 6.7(d). The inset shows increased roughness of the transformed areas with sputtering. From Fig. 6.7(d), we estimate the fraction of the bright areas to be $\approx 60\text{-}70\%$ of the film.

It is found that the number of bcc nucleation sites [Ar^+ ion dose of 1.3×10^{15} ions cm^{-2} for 500 eV, [Fig. 6.7(b)] is found to be roughly between 15 to 20 for a $1000 \text{ nm} \times 1000 \text{ nm}$ scan images ($\sim 2.3 \times 10^{-6}$ nuclei per ion impact). Immediately after nucleation, the bcc areas are not elongated but appear almost pointlike, as shown by the arrow at the left lower edge of Fig. 6.7(b). Obviously, such a nucleus later grows into a wavy structure (seen as small bright wavy structures of few tens of nm) by further ion irradiation. As formation of the bcc nuclei is a rare process in general, the initial number of the nuclei depends on the ion dose, ion energy and thickness [slightly thicker (or thinner) will have more (or less) nuclei for same ion energy irradiation]. We also see two large transformed areas of $\approx 200 \text{ nm} \times 200 \text{ nm}$; they must have grown from one point bcc nuclei with ion irradiation.

Although these needles have wavy structure, having a careful look at images reveal that they have a general growth inclination towards crystallographic directions marked as $[011]$ and $[01\bar{1}]$ (see Fig. 6.7(b)-(d)). In clean 8-ML fcc Fe films, the bcc needles orient along the $[011]$ and $[01\bar{1}]$ directions as already explained in section 6.3 [64]. This deviation is understood as a consequence of oxygen and carbon.

As it is already mentioned before in section 6.3, where the dark bcc troughs are shown next to the bright bcc; an apparent height below that of the bcc needles does not necessarily indicate an fcc structure of the dark regions. A detailed inspection of these dark regions in the STM images rather show that bcc troughs and other areas with wedge-like bcc structure extending from the bright needles are much more common in the ion-irradiated films than in the as-grown films. In irradiated films, isolated bright bcc needles are often flanked by bcc troughs, with a total trough width sometimes comparable to the width of the bright needle [see Fig. 6.3(f)]. At higher ion doses like in Fig. 6.7(c), the surface is too rough to see facets; there we can only rely on the height information to discriminate between fcc and bcc. We find that the bright needles are typically 0.3 to 0.4 nm higher than the fcc areas, while the areas in-between the needles are typically lower than the fcc regions, in the same height range as reported for the wedge-type bcc areas observed on unirradiated samples. Also this indicates that the areas between the bright needles are bcc. Thus, the film shown in Fig. 6.7(d) must be considered fully transformed to bcc.

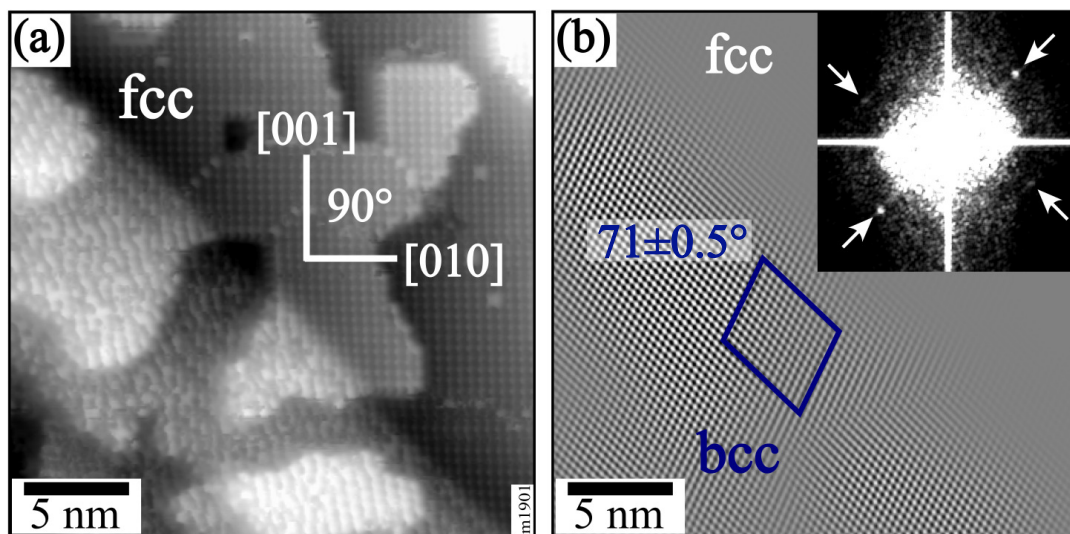


Figure 6.8: High-resolution STM image of the film in Fig. 6.3 after bombardment with 1 keV Ar^+ ions (dose: $3 \times 10^{14} \text{ cm}^{-2}$). (a) The bcc area in the lower left shows to poorly ordered oxygen while the well-ordered $c(2 \times 2)$ -O structure with its 90° bond angle is clearly seen in the bcc areas. (b) Filtering in the Fourier domain (spots marked in the inset) clearly shows the bcc lattice with a bond angle of $71 \pm 0.5^\circ$.

Structure of the bcc areas

Until this point, we have only inferred the bcc structure of the bright areas in the fcc film from their height. At ion doses like the one shown in Fig. 6.7(b), we encountered problems to atomically resolve the crystallographic structure of the bcc crystallites by STM, which could be due to the high step density induced by sputtering. Nevertheless, to get a confirmation about our argument, we took a film surface [Fig. 6.3] with pre-existing bcc areas where a mild sputtering with an ion dose of $3 \times 10^{14} \text{ cm}^{-2}$ was sufficient to significantly increase the bcc area fraction. Here the dose is four times less than in Fig. 6.3(b), but it is also a different ion energy, i.e. 1 keV. We did not obtain atomic resolution of the Fe lattice but rather see the oxygen superstructure. As shown in Fig. 6.8(a), the fcc Fe surface with its $c(2 \times 2)$ overlayer and the 90° angle between the [010] and [001] directions can be seen very clearly. The structure of the bcc area in the lower left of the image is less clear because the oxygen adatoms are randomly distributed in this area. To examine the structure of the needle, we have removed drift-induced distortion of the image [taking the $c(2 \times 2)$ area as a reference] and analyzed the bcc area in the Fourier domain. We found peaks corresponding to bcc(110), obviously caused by a partial occupation of the bcc(110) lattice with oxygen atoms in equivalent sites. This is shown in the inset of Fig. 6.8(b), bcc spots are marked by arrows. A backtransform of these Fourier components

shows the full bcc(110) lattice with a bond angle of $71 \pm 0.5^\circ$ [Fig. 6.8(b)]. This nicely agrees with the bond angle 70.5° in bulk bcc Fe, whereas a bond angle of 75° is observed in thin (5 to 8 ML) Fe films where the Fe film remains commensurate with the underlying Cu(100) substrate [7, 62]. Thus, this helps us to create a confident statement that these bcc crystallites in the 22 ML Fe films have a bulklike bcc structure as expected for such a thick film.

Different ion energies

This section explores the effect of different ion energies on the saturation state of the 22 ML fcc Fe film. Fig. 6.9 shows a comparison of the surfaces of the 22 ML fcc Fe films irradiated with different Ar^+ ion energies, (a) 500 eV, (b) 2000 eV and (c) 4000 eV. These images show saturation where the transformed area does not increase with further ion dose. The ion doses presented here are well below twice the saturation dose, however. Due to the high ion doses needed to achieve saturation, the surface becomes too rough to discriminate between fcc and bcc areas by their morphology. Therefore, we have high pass filtered the images to remove the underlying substrate steps and obtained height histograms. These histograms show a bimodal distribution, confirming the visual impression of bright bcc needles and darker areas. Fitting the histograms with a sum of two Gaussians, we can determine the fraction of the bright bcc needles. For the three ion energies in Fig. 6.9, we obtain values of 60, 52 and 44% which clearly indicate a decrease in the bright bcc transformed area for high ion energies. Also the bright bcc needles/regions for 500 and 2000 eV are more connected in comparison to 4000 eV. Assuming that the ratio between the bright and dark bcc areas is constant, the lower area fraction of bright needles observed at high ion energies would indicate some untransformed (fcc) areas. One should rather expect that any untransformed areas form larger patches like in Fig. 6.7(white squares). This is not observed at least at 2000 eV, and for 4000 eV, we may have some untransformed areas. For all ion energies the bcc needles are seen to deviate far from the crystallographic directions $[011]$ and $[01\bar{1}]$ directions marked in Fig. 6.9.

The images presented in Fig. 6.9 also show different length scales of the bright areas for different ion energies. We found that for experiments with slightly different thickness of the Fe film irradiated with the same Ar^+ ion energy show that the typical size of the bright patches does not depend so much on the ion energy but is a sensitive function of the film thickness. We therefore present a comparison of two experiments with same preparation but slightly different thicknesses. Fig. 6.10 shows saturated surface of the 22 ML film bombarded with 4 keV Ar^+ ion energy. The APPH signal shows that oxygen $\text{O}_{514}/(\text{Fe}_{703} + \text{Cu}_{920})$ signal before ion irradiation is close to 0.33 which is typical value for closed oxygen covered layer for both thicknesses. However, carbon $\text{C}_{273}/(\text{Fe}_{703} + \text{Cu}_{920})$ signal value for two presented preparations is slightly different; (a) 1.5 and (b) 1.11. However, the Fe/Cu signal shows that film (b) is thinner by $\approx 3\%$ (for film (a), $\text{Fe}/\text{Cu} = 7679$ and for film (b), $\text{Fe}/\text{Cu} = 7415$). We see that larger bcc patches (particularly thicker widths)

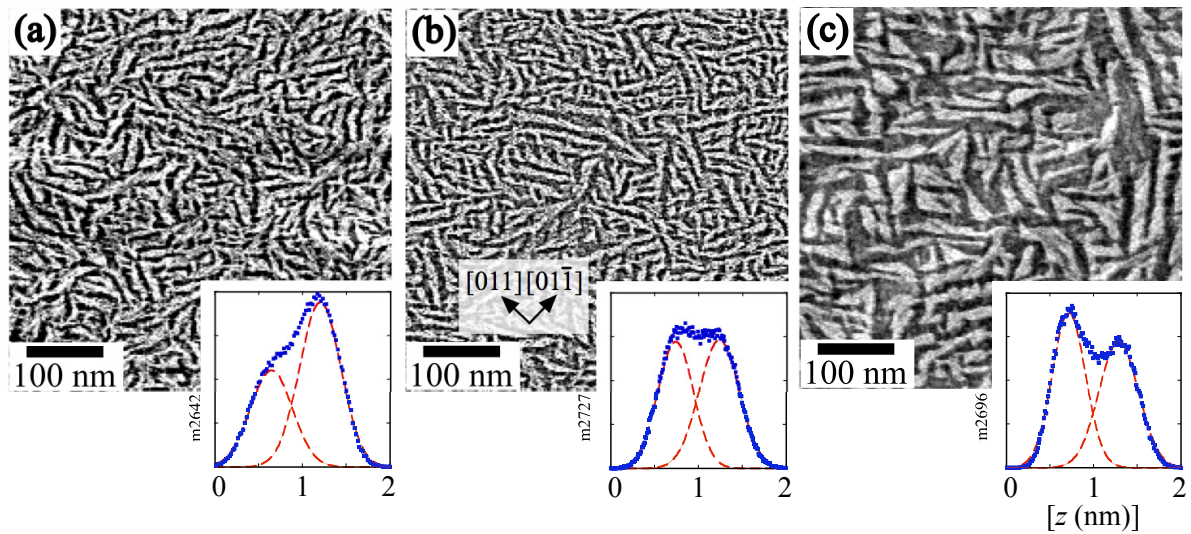


Figure 6.9: STM images of the 22 ML Fe film irradiated with different Ar^+ ion energies. (a) 500 eV (dose: $9.5 \times 10^{14} \text{ cm}^{-2}$), (b) 2000 eV (dose: $4 \times 10^{14} \text{ cm}^{-2}$), and (c) 4000 eV (dose: $3.6 \times 10^{14} \text{ cm}^{-2}$). Height histograms are shown at the bottom right.

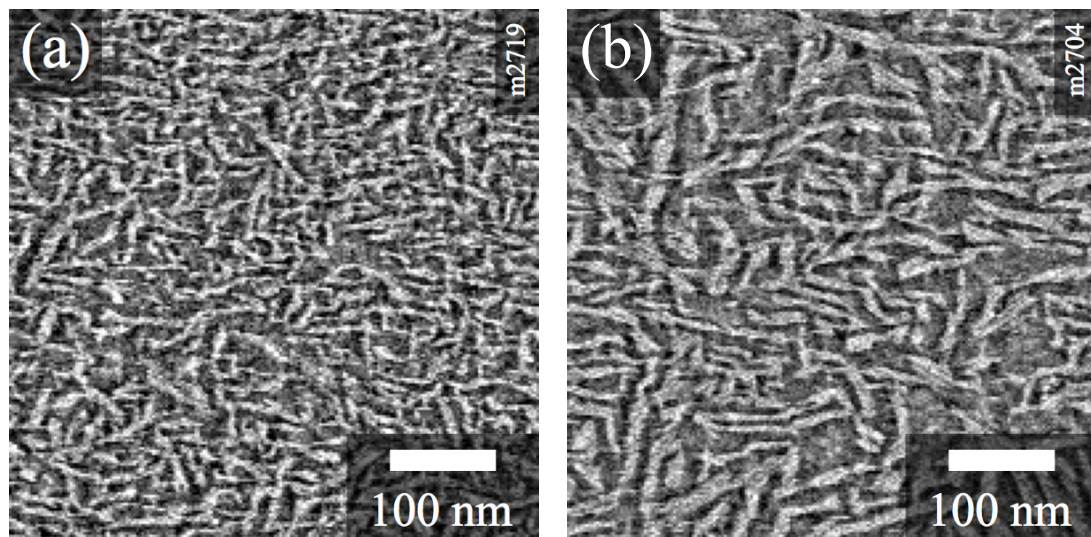


Figure 6.10: STM images of the 22 ML Fe film irradiated with 4000 eV Ar^+ ion energy with ion dose of $8 \times 10^{14} \text{ cm}^{-2}$ for slightly different thicknesses of ≈ 22 ML fcc Fe films; film (a) is slightly thicker than the film (b).

are common in films (b), where as in films (a), smaller and narrower needles are seen [compare (a) to (b) in Fig. 6.10]. Also, there is larger carbon content in (a) than in (b). It is very difficult to offer a precise explanation, but we assume that this variation in the needle outlook for same ion energy is primarily a consequence of the combined effect of carbon/or oxygen content and/or thickness. Thus, the same preparations with slightly different thicknesses could result in different transformed surfaces.

6.6 LEED

To confirm the structural analysis of the 22 ML films by STM, we conducted LEED measurements on the CO-grown 22 ML Fe film before and after irradiation with Ar^+ ions. Fig. 6.11(a) shows the LEED image at 120 eV of the as-grown film with fcc(100) spots indicated. The spots at $(1/2, 1/2)$ are caused by the $c(2 \times 2)$ oxygen superstructure at the surface of the fcc film. Except for the superstructure spots, this LEED pattern is the same as for the 8 ML Fe films grown without CO. After Ar^+ ion irradiation at 500 eV with a dose of $2.4 \times 10^{15} \text{ cm}^{-2}$, the pattern becomes blurred and bcc(110) spots become visible [Fig. 6.11(b)]. One out of four bcc domains is indicated by a rectangle in the Fig. 6.11(b). The other three domains can be obtained by 90° rotation and mirroring along the fcc(1,0) or (0,1) direction. The bcc LEED spots are strongly elongated, with the spots close to the positions of the former fcc(0,1) spots blurred mainly in the radial direction and the other two spots [upper and lower corner of the rectangle in Fig. 6.11(b)] being elongated in a parallel direction. We attribute this elongation to the tilting of the bcc areas mentioned previously; not only the low-lying areas next to the bcc needles but also the needle surfaces themselves are often tilted in a direction that would explain this kind of blurring. The blurring perpendicular to the direction of elongation is probably due to the increased roughness of the sputtered surface.

6.7 SMOKE

SMOKE measurements conducted on 22 ML fcc Fe films grown in CO on Cu(100) were carried out in a different UHV setup than the STM and LEED investigations presented above (section 4.2.3). For this setup, again we optimized the CO pressure for stabilizing the fcc phase for 22 ML Fe films; the optimum pressure was 3×10^{-9} mbar. As no STM facility is available in this chamber to see whether the as-grown film surface is fcc/bcc or partially transformed, we relied on SMOKE signals to see if the film is paramagnetic (indicating fcc) or it has changed to ferromagnetic (indicating transformation to bcc). Within the CO pressure range leading to fcc growth, the as-grown film is found to be paramagnetic at RT (curve labeled “0” in Fig. 6.12). The films undergo a transformation from paramagnetic to

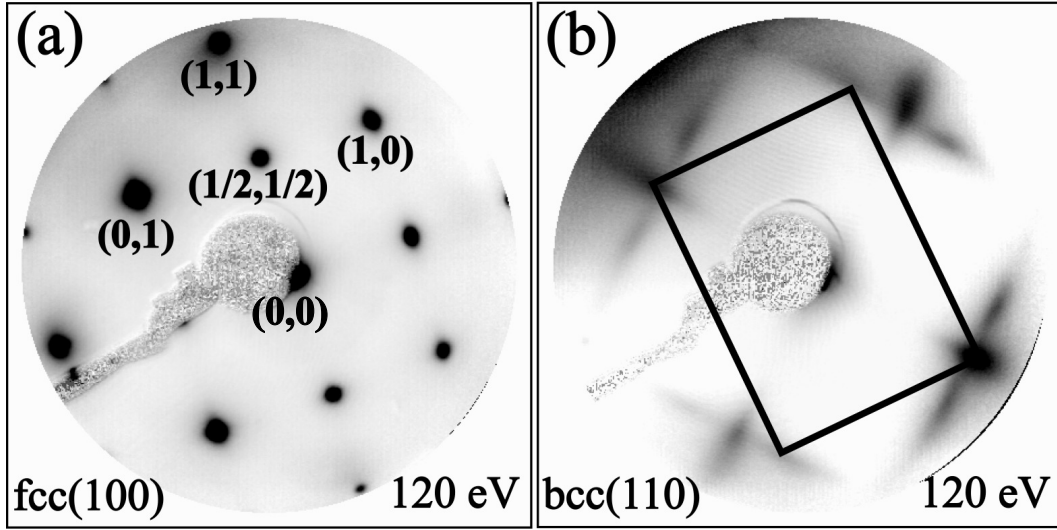


Figure 6.11: (a) LEED image of the as-grown 22 ML Fe film, showing fcc(100) and oxygen $c(2 \times 2)$ spots. (b) After Ar^+ irradiation of $2.4 \times 10^{15} \text{ cm}^{-2}$ at 500 eV, diffuse bcc satellites are visible [the rectangular bcc(110) unit cell is indicated].

ferromagnetic when irradiated with Ar^+ ions.

Fig. 6.12 shows the longitudinal Kerr ellipticity ' ε ' as a function of applied magnetic field for the 22 ML fcc Fe film, bombarded with 2 keV Ar^+ ions. After a fluence of $3 \times 10^{14} \text{ cm}^{-2}$, the magnetic behavior of the film changes to ferromagnetism with an in-plane easy axis. With increasing the Ar^+ ion fluence, the Kerr signal and, hence, the magnetization increases and reaches a maximum (saturation) at a fluence of $6 \times 10^{14} \text{ cm}^{-2}$. For lower ion dose the width of the hysteresis loop (coercive field) is larger, which becomes narrower with increasing ion fluence.

The longitudinal Kerr ellipticity at magnetic saturation ε_{sat} as a function of Ar^+ ion dose for different ion energies is shown in Fig. 6.13(a). For ion energies up to 2 keV, the transformation gets faster with increasing ion energy, i.e., the ions become more efficient in transforming the film from fcc to the bcc phase. For 4 keV Ar^+ ion energy, the transformation was slower than for 2 keV and the maximum magnetization reached is lower than for lower ion energies. A similar behavior was already observed for pure 8 ML Fe films [64], but with a decrease in the saturation magnetization at much lower ion energies (highest efficiency at 1 keV). In all curves, there is a slight decrease of the magnetization after reaching the saturation value, which is attributed to the sputter removal of Fe after prolonged irradiation with Ar^+ ions.

The maximum saturation value of the longitudinal Kerr ellipticity ε_{sat} is $320 \mu\text{rad}$, which is higher than for the pure 8-ML Fe film, where a maximum value of $150 \mu\text{rad}$ at 1 keV

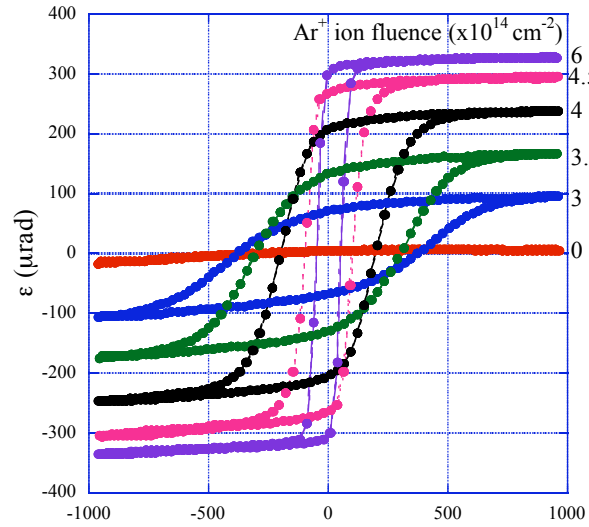


Figure 6.12: Hysteresis loops of the 22-ML Fe films irradiated with 2 keV Ar^+ ions, showing longitudinal Kerr ellipticity ε as a function of magnetic field H . The transformation from paramagnetic (ion dose: 0) to ferromagnetic with increasing ion fluence can be seen.

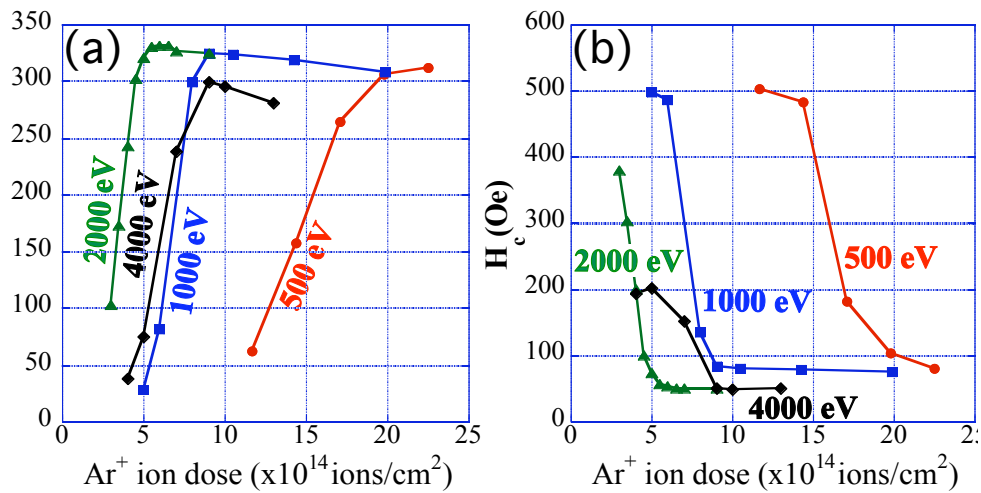


Figure 6.13: (a) Saturation value of longitudinal Kerr ellipticity ε_{sat} as a function of Ar^+ ion dose for different ion energies and (b) coercive field H_c as a function of Ar^+ ion dose.

Ar^+ ion energy was found [64]. For a completely transformed 22 ML film we might expect the maximum saturation value to be roughly 22/8 times the value for 8 ML film, i.e., 412 μrad . This calculation ignores the decay of the light's electric field with increased film thickness, however. The optical skin depth is about 24 nm, only 6 times the thickness of the film, which would yield a decrease of the Kerr angle to $\approx 350 \mu\text{rad}$ at perpendicular incidence. As we are measuring at a more grazing incidence (60°), we attribute the lower value found to a faster decay with thickness at this angle.

Fig. 6.13(b) shows the coercive field H_c as a function of Ar^+ ion dose. The coercive field is obtained from the hysteresis graphs for the respective Ar^+ ion fluences. The coercivity is high in the beginning of ion irradiation for all energies and sharply drops with increasing ion dose. As in Ref. [61], we can explain this by separate (magnetically decoupled) needles with a large length-to-width ratio in the early stages of transformation [see Fig. 6.7(b)]. These needles have a high shape anisotropy and possibly also some magnetocrystalline anisotropy due to residual strain. The initial coercive field is similar from 500 eV to 2 keV ion energy, but is clearly lower for 4 keV. For 4 keV the transformation is also less efficient as mentioned earlier.

6.8 Mechanism of the Ion-Induced Transformation

As we mentioned earlier, this system is stabilized in the fcc phase by two agents; carbon contributing to bulk and oxygen to surface stability of fcc Fe film. There has to be a critical balance between them for stable fcc, absence of either results in the transformation. So, the question is: is the oxygen removal by sputtering during ion irradiation the main stimulating factor for the ion-induced transformation or is it the energetic ions imparting energy in the Fe films, hence causing transformation? Therefore, discussing the mechanism of the ion-induced transformation, we should first analyze whether mere removal of oxygen from the surface by sputtering could cause the transformation. We have shown already that removal of more than 80% of the adsorbed oxygen is required for a transformation of much of the film surface, but still leaves a few untransformed patches [Fig. 6.6(b)]. This state of surface is similar to transformation by ion bombardment before saturation is reached [Fig. 6.7(c)]. At this stage of ion bombardment, the APPH $\text{O}_{514}/(\text{Fe}_{703}+\text{Cu}_{920})$ ratio has decreased to 72% of its initial value, i.e., less than 30% of the oxygen has been removed. Thus, we can say that the removal of oxygen alone by sputtering is insufficient to explain the ion-induced fcc-bcc transformation.

For a better idea about the number of the atoms present in the molten volume, we have employed binary collision cascade simulations with the SRIM code [91] to calculate the energy transferred to the target, E_{nucl} . For this we used a 4 nm thick Fe layer on a 100 nm thick Cu as substrate layer, which was irradiated with 10,000 Ar^+ ions at perpendicular incidence. This was done for different Ar ion energies. The E_{nucl} transferred to Fe atoms

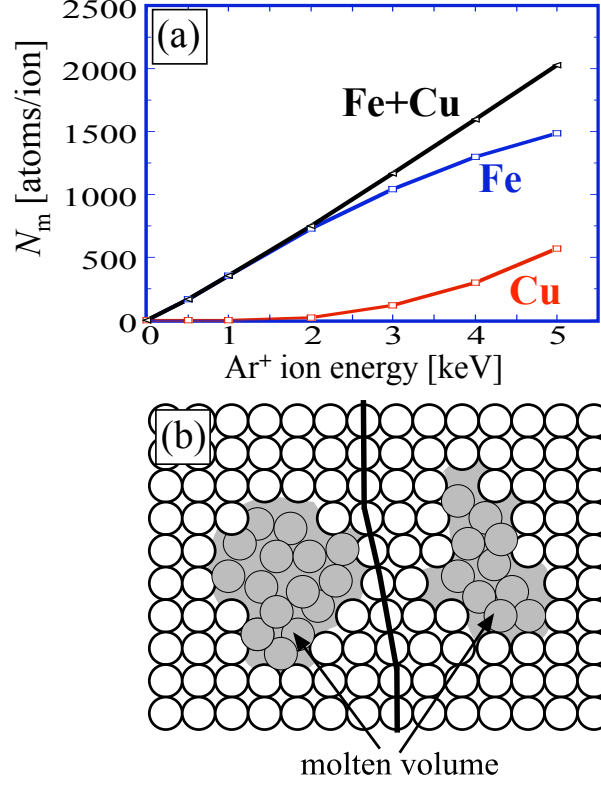


Figure 6.14: (a) Calculated number of atoms N_m in the molten volume for a 22-ML-thick fcc Fe film. The fraction of Cu atoms in the melt is negligible up to 2 keV and increases with increasing ion energy (b) Schematic view of an arrangement leading to a sheared structure during recrystallization, a possible bcc nucleus.

and Cu atoms can be separately obtained from the simulation files. According to Ref. [78], the number of atoms in the melt can be estimated using eq. 2.17.

With increasing Ar^+ ion energy, the number of atoms in the melt increases, but above an energy of ≈ 2 keV the collision cascade also reaches the Cu substrate and intermixing between Fe and Cu occurs shown in Fig. 6.14(a). With Cu favoring the fcc structure, mixing will be detrimental for the fcc-bcc transformation. This result nicely explains the reduced transformation efficiency at an ion energy of 4 keV, leading to a lower bcc fraction after the transformation, seen in both STM (Fig. 6.9) and the magnetization data [Fig. 6.13(a)]. Intermixing might also explain the lower coercivity of the films transformed by 4 keV Ar^+ [Fig. 6.13(b)]. The importance of intermixing is supported by comparison with

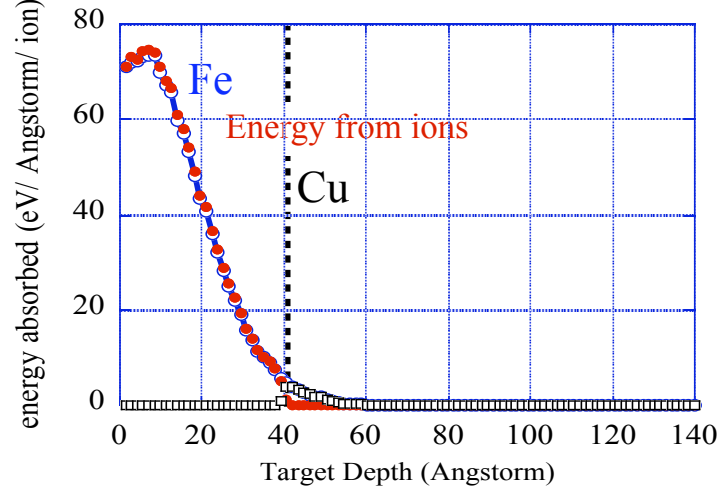


Figure 6.15: SRIM output file for a 2 keV Ar^+ ion energy showing ion-energy-absorption profile as a function of target depth with 22-ML Fe (closed circles) and Cu (open circles) atoms.

the data for 8-ML films in Ref. [64], where the maximum efficiency of the transformation was observed at 1 keV, again just before the collision cascade reaches the substrate and intermixing can occur. In the SMOKE system we have perpendicular incidence of Ar^+ on the sample. This may possibly lead to channeling and, thus, even deeper collision cascades at high energies.

Fig. 6.15 shows an output file for the SRIM calculations where the ion-energy absorption profile for 2 keV Ar ions is plotted as a function of target depth (which is 40 Å Fe film on 100 Å Cu substrate). The units of absorbed energy along y-axis are ‘eV/Å/ion’. We see most of the Ar ions lose their energies to the Fe atoms, only a negligible fraction could reach the Fe-Cu interface. This plot can be generated by requesting the E2RECOIL plot from the active SRIM screen. From this plot we can easily infer that most of the energy from the incident Ar ions is imparted in the Fe atoms. Only a very small fraction which is negligible could reach Fe-Cu interface. This agrees well with the STM and SMOKE measurements. We have also used the plot in Fig. 6.15 to estimate the number of atoms in the melt shown in Figures. 6.14(a) and 6.18.

In Ref. [64], the mechanism of the ion-induced transformation is already explained on the basis of the so-called “thermal spike model” [84, 85] in sputtering. As discussed in section 2.3 “thermal spike” means that impact of an energetic single ion strongly heats the target material in a small volume to such an extent that it melts down the material in that small volume. While the thermal spike model does not explain sputtering of metals by Ar^+ ions

in the energy range under consideration (sputtering is caused by the collision cascade) [115], the existence of a molten volume after an ion impact is established by computer simulations as well as by the outflow of material from that volume [89, 90]. A few picoseconds after the impact, the material is rapidly cooled down by heat exchange to the surrounding regions and crystallizes. Usually, crystallization will be pseudomorphic to the surrounding lattice, but it is easily conceivable that various crystallographic defects can be created by rapid quenching of the molten volume. Especially in case of a collision cascade with two or more hot spots (created by fast recoils), the resolidification front will be non-spherical and it may happen that crystallization from two opposite sides results in a sheared structure, which may form the nucleus of a bcc crystallite. Fig. 6.14(b) shows schematic view for such an arrangement resulting in possible bcc nuclei. Creation of a stable bcc nucleus must be a rather rare process, as evidenced by the low number of nuclei observed in the STM images [$\approx 3 \times 10^{-5} \text{ nm}^{-2}$ in Fig. 6.7(b), i.e., $\approx 2 \times 10^{-6}$ per impinging ion]. As soon as a bcc crystallite is formed, it may grow by further ion impacts, either through recrystallization from the melt or by defects that make it possible to shear a larger area into its stable bcc arrangement (cf. Refs. [7] and [62]).

6.9 22 ML Fe film coated by Pd and Au

Exposing the samples to ambient conditions is needed when transferring the Fe-coated Cu crystal to a focused ion beam facility for nano-patterning or for some other analysis. Also for any technological applications, the films must be covered with a protective layer to prevent oxidation. Therefore, we present the 22 ML fcc Fe film prepared in CO and covered with two metals, Pd and Au. In contrast to the pure Fe films having no or negligible oxygen on the surface investigated in Ref. [64], these films have oxygen layer at the top, therefore, we have to examine whether oxygen at the surface of the Fe films prevents wetting by the overlayer material. It is also interesting to explore whether the fcc-bcc transformation can be still detected by STM after coating.

Fig. 6.16 shows the surface of a 22 ML fcc Fe film prepared in CO and covered with 2.25 nm Pd [this corresponds to 10 ML Pd(111) or 10 ML of a hypothetical pseudomorphic overlayer on Cu(100)]. The STM images (a,b) show a continuous film with no dewetting. But the film does not observe a layer-by-layer growth. Although the images are not perfect and also distorted, we clearly see that part of the film shows a Pd(100) surface (black arrows in Fig. 6.16(a)), while the other areas are predominantly Pd(111) (white arrows in Fig. 6.16(a)). Fig. 6.16(b) shows an area that is predominantly Pd(111) but also here we observe different azimuthal orientations of the Pd film. Some crystallites have a size of only a few nm. It is likely that grain-boundary diffusion of oxygen would occur through the Pd film, thus we do not consider Pd a good protective overlayer.

The second metal used for film coating is Au. Fig. 6.17(a) shows an STM image of the

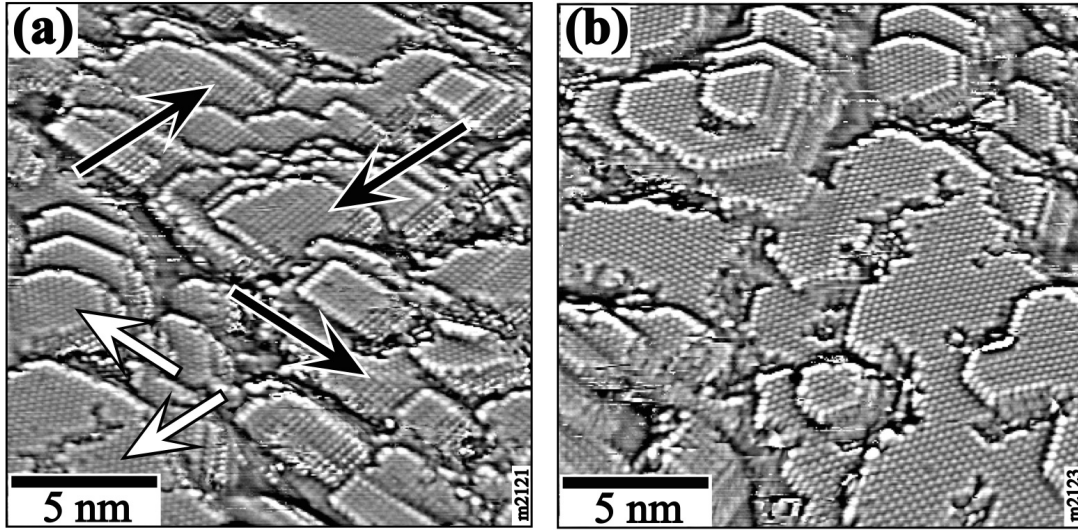


Figure 6.16: STM images (strongly high-pass filtered) of the 22 ML fcc Fe film covered with 2.25 nm Pd. (a) Pd grows in (100) orientation in the regions indicated with black arrows and as (111) indicated with white arrows. (b) Most of this area shows (111) growth.

as-prepared surface of the 22 ML fcc Fe film, showing a few bcc needles in the large scan of $1000 \text{ nm} \times 1000 \text{ nm}$. It is then covered by 0.52 nm [corresponding to 2.2 ML Au(111)] indicating almost perfect layer-by-layer growth shown in Fig. 6.17(b). This film was further coated with 1.48 nm [in total: 2 nm Au, corresponding to 8.5 ML Au(111)] see Fig. 6.17(c). Also the 2-nm Au film exhibits good layer-by-layer growth. The lattice matching between bcc Fe(110) and Au(111) is much better than that between fcc Fe(100) and Au(111), therefore, we have suggested previously that a Au overlayer could facilitate the fcc-bcc transformation (Rupp et al. [64]). We have therefore grown a film on the verge of the fcc-bcc transformation to check for any Au-induced transformation [compare Fig. 6.17(a) and (c)]. We found only a small increase of the bcc area fraction by Au deposition.

Finally, to investigate whether it is possible to see the transformation of the Au coated Fe film by STM, we irradiated this Au/Fe/Cu(100) metastable film with Ar^+ ions at 3 keV. Fig. 6.17(d) shows that most of the film was transformed with an ion dose of $9 \times 10^{14} \text{ cm}^{-2}$. We cannot detect any untransformed areas in the film. Atomic resolution of this transformed system was difficult due to increased roughness of the surface.

We should also mention here that the Ar ion energy of 3 keV would be sufficient to cause some Fe-Cu intermixing in the uncoated 22 ML Fe films. But for films coated with 2 nm Au, the Fe-Cu interface is out of reach for the ions (as calculated by SRIM [91]). Thus, no Fe-Cu intermixing will impede the fcc-bcc transformation. On the other hand, lower energies as preferred for the uncoated films would be insufficient to penetrate through

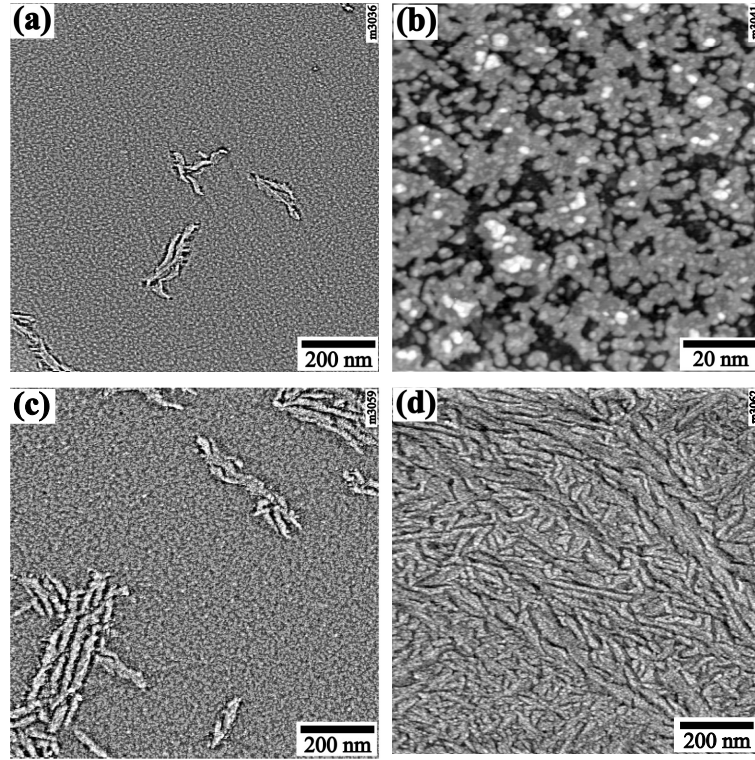


Figure 6.17: High-pass filtered STM images of the 22 ML fcc Fe film (a) as prepared in 7.5×10^{-10} mbar CO pressure and after deposition of (b) 0.52 nm and (c) 2 nm Au. (d) Surface covered with 2 nm Au after irradiation with $9 \times 10^{14} \text{ cm}^{-2}$ Ar^+ ions at 3 keV.

the Au capping layer. It is interesting to note that Au-Fe intermixing, though certainly occurring, seems to have no negative influence on the fcc to bcc transformation of the 22 ML fcc Fe film.

For Au coated Fe films, we employed SRIM calculations to estimate the energy of the Ar^+ ions, as to avoid the intermixing of the Fe-Cu interface for carrying out the fcc \rightarrow bcc transformation of the Fe films. The SRIM calculation for 22 ML Fe on Cu coated with 2 nm Au layer clearly shows that below 4 keV Ar^+ ion energy, almost all of the energy is dissipated in the Au and Fe film [see Fig. 6.18]. The total energy transferred to the Au target atoms is 1048 eV/ion (E_{nuc} for Au) and to Fe atoms is 1242 eV/ion (E_{nuc} for Fe), see Fig. 6.18. Therefore, low Ar^+ ion energies, i.e., 3 keV Ar^+ ion energy used above does not cause Fe-Cu intermixing which might impede the transformation process.

For uncoated 22 ML films, complete transformation was observed below a dose of ~ 1 ML Ar ion irradiation for all energies (compare Figs. 6.9 and 6.13). And for 2 nm Au coated 22 ML Fe film, complete transformation was observed for 3 keV Ar ion energy at a dose of ~ 1 ML. We don't have transformation evolution data for the Au coated film, as the

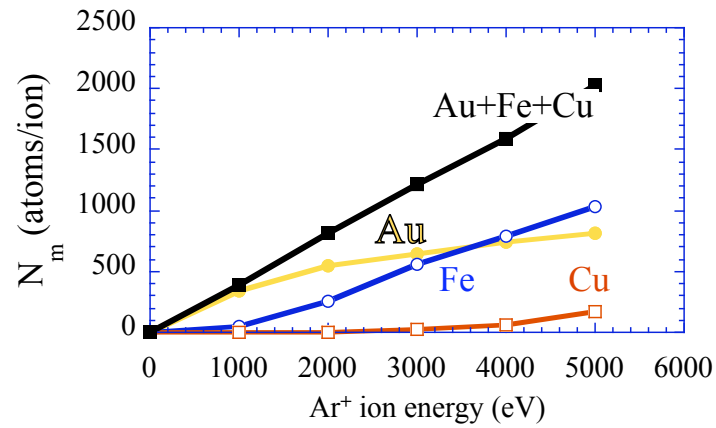


Figure 6.18: The calculated number of atoms in the molten volume for 22 ML (4 nm) Fe films coated with 10 ML (2nm) Au for different ion energies.

main task of this experiment was to observe whether we see transformation through the Au coated film or not. And we showed that although atomically resolved images were not possible, but transformation could be seen in these films.

Chapter 7

44 ML $\text{Fe}_x\text{Ni}_{1-x}$ films on Cu(100)

7.1 Introduction

The properties and transformation of CO-stabilized 22-ML fcc Fe films have been presented in detail in chapter 6. In the current chapter, we present the stability and growth of even thicker fcc Fe films stabilized by alloying with nickel. We will reach a thickness of 44 ML (8 nm). We also present the ion-induced fcc-bcc transformation of these metastable films. The structural analysis was conducted using STM and the concentration of Ni was analyzed using AES.

7.2 Film Growth and Properties of 44 ML fcc Fe film

As mentioned earlier, stabilization of thicker Fe films grown on Cu(100) requires some stabilizing agent. Nickel has an fcc structure and is comparable in atomic size to Fe, therefore, its incorporation in the Fe films would not effect the fcc nature of the as prepared films. Now, to address the obvious question as to how much of the Ni is needed to grow metastable fcc Fe films of particular thickness, let's take a look at the phase diagram of $\text{Fe}_x\text{Ni}_{1-x}$ shown in Fig. 7.1 [116, 117], where Curie temperature T_c for the γ (fcc-Fe phase) is marked with an arrow pointing at 0% Fe. Invar with Ni concentration close to about $\approx 36\%$ is fcc ferromagnetic and is close to the phase boundary between fcc and bcc marked by a small hatched section in Fig. 7.1 [118, 119]. At close to this concentration several physical properties like magnetic moment and Curie temperature has sharp dependence on Ni concentration [118]. The Curie temperature for $\text{Fe}_{64}\text{Ni}_{36}$ is 553 K. The '*Invar*' region

is marked as hatched region for concentrations between ~ 50 -65 at.% Fe, close to the structural transformation $\gamma \rightarrow \alpha$ region [116]. We achieved the desired thickness of 44 ML Fe films using Invar $\text{Fe}_{64}\text{Ni}_{36}$ and Fe which has an advantage that small differences in the evaporation rates would lead to lower variations in the Fe/Ni concentration ratio in the film.

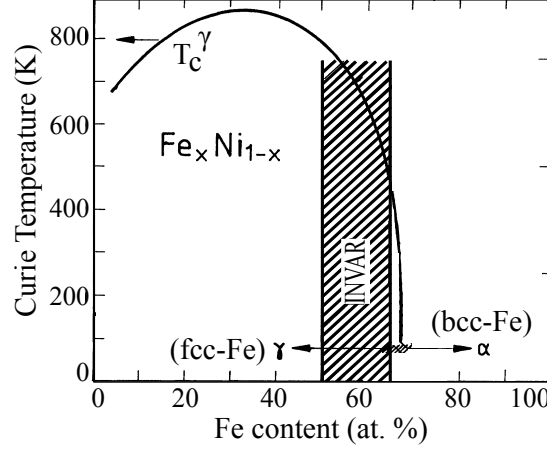


Figure 7.1: The magnetic phase diagram of $\text{Fe}_x\text{Ni}_{1-x}$ [116].

Therefore, the technique used to stabilize thicker fcc Fe film i.e. 44 ML, at RT was by co-evaporation of Fe and Invar ($\text{Fe}_{64}\text{Ni}_{36}$) on the Cu(100) single crystal in UHV. Here, Ni is the main component contributing to the stability of fcc Fe film. Fe films were evaporated on a Cu(100) single crystal simultaneously from the tips of Fe and Invar ($\text{Fe}_{64}\text{Ni}_{36}$) rods as explained in section 4.2.4. The deposition rates were calibrated separately for Fe and Invar using quartz crystal microbalance. The total time t_{tot} , required to evaporate 44 ML fcc Fe film was estimated from the trivial equation:

$$t_{tot} = 44 \left[\frac{1}{R_{Fe} + R_{Invar}} \right] \quad (7.1)$$

where R_{Fe} is the deposition rate (ML/sec) for Fe and R_{Invar} is the rate for Invar. The concentration of Ni denoted by C_{Ni} can be easily calculated from deposition rates of Fe and Invar as following:

$$C_{Ni} = \frac{36 \times R_{Invar}}{R_{Fe} + R_{Invar}} \quad (7.2)$$

During evaporation, obviously the relative deposition rates of Fe and Invar dictate the final concentration of Ni in the Fe film, which is the only stabilizing agent in these thicker metastable films.

7.3 STM measurements

The summary of the Fe-Invar co-evaporation experiments is presented in the table 7.1. The Ni concentration $C1_{Ni}$ is calculated from eq. 7.2. The other Ni concentration $C2_{Ni}$ is estimated from the AES data, by using:

$$C_x = \frac{\frac{I_x}{S_x}}{\sum \frac{I_i}{S_i}} \quad (7.3)$$

where C_x is the atomic concentration of the required material, I_x is its intensity from the Auger signal and S_x is the relative sensitivity for pure material [97]. The summation is for all the corresponding ratios of all other elements in the sample. Here, the required element is $x = \text{Ni}$ with $S_{Ni} = 0.27$ and sensitivity factor for Fe is $S_{Fe} = 0.2$ [97]. The last column in table 7.1 shows the structure of the prepared film as observed in the STM for corresponding Ni concentrations. In table 7.1 for experiments from 1-3; the evaporation rates for the Fe and Invar rods were same. The Ni concentration value $C1_{Ni}$ shows 18% Ni concentration in the film for experiments 1-3, but concentration $C2_{Ni}$ estimated from AES was always less than 18%. Thus, the value $C2_{Ni}$ was observed to be different for all experiments with same deposition rates.

No.	$C1_{Ni}$	$C2_{Ni}$	STM
1	18%	11.9%	bcc
2	18%	13.1%	bcc
3	18%	15.1%	fcc
4	22%	20.7%	fcc

Table 7.1: Measurement overview for the Fe-Invar experiments

Based on these observations, we divide our experimental results into three sections depending on the concentration of Ni in the fcc film estimated from AES. In this section we present the STM measurements for different Ni concentrations and explore which one is most suitable Ni concentration offering metastable 44 ML fcc Fe films.

With Ni concentrations at and below $\approx 13.1\%$, the STM images show that the surface of the as-grown 44 ML Fe film is already transformed to bcc (experiment 1 and 2 in table 7.1) with same Fe and Invar Fe₆₄Ni₃₆ evaporation rates. Fig. 7.2 shows STM image of the as-grown 44 ML Fe film with $\approx 13.1\%$ Ni concentration. The transformed bcc areas are different from 8 ML Fe films (cf. Fig. 7.2 and 6.9). Most of the film is observed to be transformed with few untransformed regions (see bottom of Fig. 7.2). These bcc transformed areas have a complex shape with ridges having a typical width of 10-20 nm and length extended over

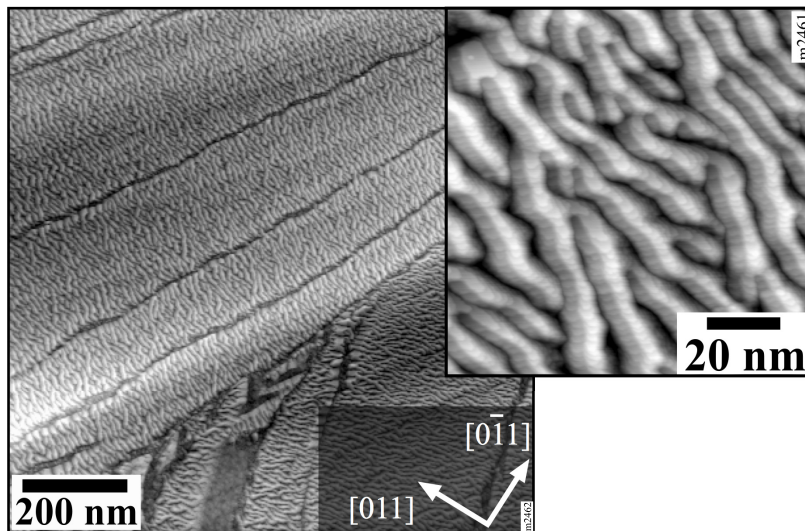


Figure 7.2: STM image of the as-grown 44-ML fcc Fe film with less than 13.1% Ni. The film is already transformed to bcc. The inset shows the complex shape of the bcc areas.

several hundred of nanometers. They are wavy and have branched root like structures as seen in the overview image as well as shown in inset of Fig. 7.2.

For Ni concentration at about $\approx 15.1\%$, we found that the 44 ML fcc Fe film grows as an fcc Fe film with very few bcc needles as shown in Fig. 7.3. Fig. 7.3(a) shows an STM image of the as grown 44 ML fcc Fe film at 15.1% Ni concentration which was achieved with same evaporation rates of Fe and Invar (see table 7.1: experiment 3). The inset of the image reveals that this Fe film follows a layer-by-layer growth with few monoatomic islands, resembling the 8-ML fcc Fe film surface [cf. Fig. 7.3(a) and Fig. 6.4].

For Ni concentration at $\approx 20.7\%$, 44 ML Fe film is seen to stabilize in fcc phase as shown in Fig. 7.4. This is achieved for $\approx 33\%$ faster Invar $\text{Fe}_{64}\text{Ni}_{36}$ evaporation rate (table 7.1 experiment 4). The surface of the as grown film shows layer-by-layer growth [inset Fig. 7.4(a)], with no bcc areas.

7.4 Ion beam induced Transformation

The ion beam induced transformation is carried out after a successful attempt in stabilizing the 44 ML fcc Fe film for two Ni concentration experiments i.e. 15.1% and 20.7% [experiment 3 and 4 in table 7.1].

For 15.1% Ni concentration, this film is then exposed to Ar^+ ion irradiation to explore its

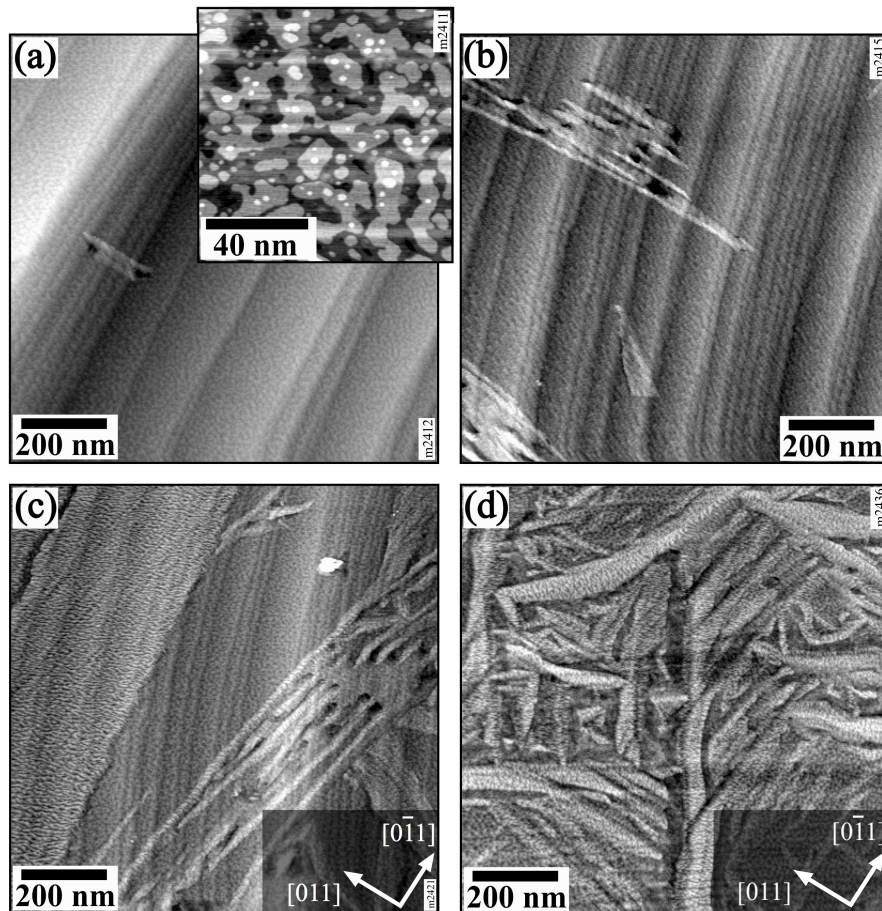


Figure 7.3: STM images of the 44-ML fcc Fe film with 15.1% Ni concentration irradiated with 2 keV Ar^+ ion energy. (a) As grown 44 ML fcc film, with very few bcc areas. Inset of the image shows layer-by-layer growth. (b) After an Ar^+ ion irradiation of 2.0×10^{14} ions/cm², few areas undergo fcc to bcc transformation. (c) The surface of the 44 ML fcc Fe film after Ar^+ ion dose of 6.5×10^{14} ions cm². (d) The film transforms to bcc after an Ar^+ ion dose of 3×10^{15} ions/cm² with a few patches still fcc.

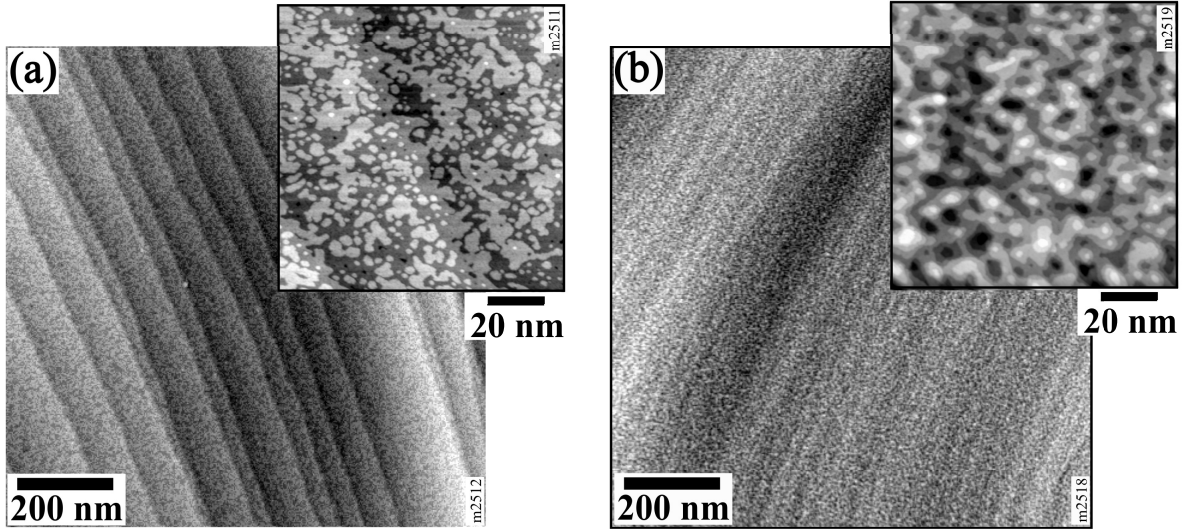


Figure 7.4: STM images of the 44 ML fcc Fe film with more than 20.7% Ni concentration. (a) The film grows as fcc with no bcc areas. The inset shows layer-by-layer growth of the film. (b) After Ar^+ ion irradiation of 2.8×10^{15} ions/ cm^2 at 2 keV, no transformation is observed. The inset shows the sputtered fcc surface after prolonged irradiation.

effect on the fcc to bcc transformation. Fig. 7.3(b) shows the surface of the film after an Ar^+ ion irradiation of 2×10^{14} ions/ cm^2 at 2 keV. The bcc transformed areas could be identified as large patches having bunch of needle like structures. Again, the bright bcc needles could be identified as bright due to the 5-10% larger interlayer distance between fcc(100) Fe and bcc(110) Fe. These bcc-needle like structures are seen to have typical width of 10-20 nm and length of several hundred nanometers. With increasing Ar^+ ion dose, at 6.5×10^{14} ions/ cm^2 , we observed an increase in the length and width of bcc areas, becoming random and complex as shown in fig. 7.2(c). With further, Ar^+ ion dose to 3×10^{15} ions/ cm^2 [Fig. 7.3(d)], the film transforms to bcc with different shapes and sizes.

Ar^+ ion irradiation was also carried out on a 44 ML film surface with 20.7% Ni concentration. Fig. 7.4(b) shows the surface of the film after Ar^+ ion irradiation of 2.8×10^{15} ions cm^{-2} at 2 keV. It shows no signs of transformation to bcc. The inset in Fig. 7.4(b) shows an increased surface roughness due to prolonged irradiation.

7.5 Discussion

The variation in the concentration of the Ni in the film is the main and only factor which dictates the stability of 44 ML thick fcc Fe films grown on Cu(100) at RT. For Ni concentration at and less than 13.1%, the STM image [Fig. 7.2] suggest that the Ni concentration is too low to stabilize film as fcc. Therefore, the film is seen to grow as already transformed which can be explained as follows: the Ni content present in the film, is not high enough to provide stability but is still enough to hinder the shape of bcc needles and push them in different directions and hence result in the shapes we see in Fig. 7.2. This feature of deviation from straight needles (a character of bcc crystallites in 8 ML fcc Fe film) is also common in as grown 22 ML CO-stabilized films as well as in Ni stabilized 44 ML Fe films after irradiation [cross refer Fig. 8.2(c) to Fig. 6.3(a) and Fig. 7.2]. Although single needles (or group of needles) formed in the early stages of transformation in the 44 ML fcc films are straight before coalescence at higher doses (Fig. 7.3(b,c)).

For 15.1% Ni concentration, the stable 44 ML fcc Fe film surface suggests a suitable Ni concentration. This film is later irradiated with different Ar^+ ion doses. The film gets transformed to bcc areas, forming different shapes oriented along random directions. Again, Ni being only stabilizing agent in the film is pushed due to (linear) bcc needles formed with initial doses and starts accumulating. With further ion dose these accumulated Ni in the film hinders further growth of bcc needles and pushes them away in random directions resulting in different shapes.

The films with 20.7% Ni concentration, show a very stable surface [Fig.7.4] which could not be transformed to bcc even after prolonged Ar^+ ion bombardment. For 15.1% Ni concentration, almost complete transformation was observed at 3×10^{15} ions/cm² Ar^+ ion dose, whereas for 20.7% Ni concentration, no transformation is observed at almost same dose [2.8×10^{15} ions/cm²]. Therefore, we conclude that transformation is not possible for a 44 ML fcc film for 20.7% Ni concentration or more due to the fact that Ni concentration is too high.

The Ar^+ ion induced transformation of the 44 ML fcc Fe film (with 15.1% Ni) is carried out with 2 keV, which is an energy too low to cause any Fe-Cu intermixing as can be seen in section 6.8. Therefore, at 2 keV Ar^+ ion energy, no Cu is introduced in the film which might impede the fcc-to-bcc transformation.

At this point, it is worth comparing the number of bcc nucleation sites for clean 8 ML, CO-stabilized 22 ML and 44 ML Fe films. For 8 ML clean Fe films, the number of bcc nucleation sites [Ar^+ ion dose of 2.3×10^{14} ions cm² for 500 eV, (Fig. 5.4)] are found to be ≈ 7 for a 300 nm \times 300 nm scan images ($\approx 3.4 \times 10^{-5}$ nuclei per ion impact). For CO-stabilized 22 ML films, we have 15-20 bcc nucleation sites ($\approx 2.3 \times 10^{-6}$ nuclei per ion impact) as mentioned in detail in section 6.5. And for 44 ML Fe films, we found ≈ 2 bcc nucleation sites ($\approx 1 \times 10^{-6}$ nuclei per ion impact) [Ar^+ ion dose of 2×10^{14} ions cm² for 2 keV] for a 1000 nm \times 1000 nm scan images [Fig. 7.3(b)]. This leads to the fact that

bcc nucleation is a rare process in fcc Fe films for all thickness by ion irradiation. The bcc nucleation sites suggests that 8 ML Fe films have better probability for bcc nucleation in comparison to thicker films. This number of course depends on the selection of ion energy for a particular thickness.

The mechanism of the fcc \rightarrow bcc transformation by ion irradiation is explained in detail in section 6.8 on the basis of “Thermal Spike” model.

The Ni concentration $C_{2\text{Ni}}$ estimated from AES was found to be lower than the calculated concentration from evaporation rates $C_{1\text{Ni}}$. This could be due to the fact that as the evaporation times were typically ≈ 22 min, the deposition rates for both Fe and Invar deviated from the initial settings calibrated using quartz crystal microbalance. Monitoring the deposition rates at all times during evaporation was not possible, as the flux monitor electrode was connected to 1-1.2 keV to suppress high energy ions. Therefore, the final Ni concentration was hard to predict.

Although, we faced a problem in controlling the concentration of Ni in these experiments (as mentioned above) due to longer evaporation times, we managed to roughly estimate, the concentrations of Ni in the 44 ML fcc Fe films. Monitoring carefully the rates of evaporation of Invar and Fe during evaporation, this technique promises even thicker films. Anyhow, these experiments could be helpful for any future research on this system.

Chapter 8

Nanopatterning by irradiation through a mask

8.1 Introduction

Recent technological advancements have driven a remarkable interest in synthesis and patterning techniques of magnetic materials at nanoscale. Additionally, it offers unprecedented opportunities to manipulate the size dependent properties of these materials [120–124]. They can find potential applications in recording media and integrated magneto electronics [125–127]. With increasing demand for areal density in recording media, nano-patterned magnetic segments can offer a reasonable method to enhance the areal densities of magnetic spacers and the non-magnetic media separating them would ensure minimum interaction between them; the so-called “cross talk” minimization.

Reproducibility of these nano-structures is of fundamental importance. Two general modes followed for the synthesis are: Bottom-up and Top-down methods. Bottom-up methods are based on self organization of structures at the nanoscale [121, 128, 129] or at defect lattices which serve as templates [130, 131]. They have the advantage of simplicity and fast (parallel) patterning of large areas, and a drawback that they are not suitable for most devices, as the control over the structures is very limited. In contrast to Bottom-up methods, the Top-down approach offers writing arbitrary structures and long range order, which is an obvious requirement for designing devices. Top-down techniques include optical (ultraviolet) or electron beam lithography and focused-ion-beam (FIB) methods [132, 133]. The lithography techniques have the disadvantage of a rather complex multistep process (coating, exposure, developing, and resist removal after the processing step), while the

conventional focused-ion-beam techniques have the disadvantage of serial writing, which results in low throughput. Ion-beam lithography can also be employed as a parallel process [134, 135] which eliminates all these disadvantages and makes ion-beam induced processes a potential candidate for future nanotechnology applications.

We have already shown that the transformation of the Fe film from fcc to bcc (paramagnetic to ferromagnetic phase) in the thickness range-II can be induced by Ar^+ ion irradiation for 8-ML films (chapter 5) grown in UHV as well as 22-ML films stabilized by CO (chapter 6) and 44-ML $\text{Fe}_x\text{Ni}_{1-x}$ films (chapter 7). In these studies, due to insufficient lateral resolution, we were not able to or we could only roughly explore the feasibility of this method for nano-patterning. Also the lateral resolution of this magnetic nano-patterning technique using ions remained unexplored.

The current chapter addresses this issue and, in addition to that, it presents an ion nano-patterning method using a mask (described in detail in chapter 4), which is an easy-to-handle and a cost-effective experimental method for any UHV system.

Both 8 and 22 ML fcc Fe films (stabilized in CO) were grown under the same experimental conditions as described in section 4.2.4, and later irradiated through the mask. These mask-irradiated Fe surfaces were then explored by STM.

8.2 Results

8.2.1 8 ML fcc Fe film

The cleanliness of the 8 ML fcc Fe films was examined by using AES, which typically showed an O_2/Fe of the Auger peak-to-peak heights below 4%, soon after preparation. The fcc-to-bcc transformation of the 8-ML fcc Fe films was carried out with Ar^+ ion irradiation at 1 keV, which gave the best transformation results for 8-ML fcc Fe films, as reported by Rupp et al. [64]. The film was irradiated through the mask with 1 keV Ar^+ ion doses of 0.5×10^{15} ions/cm² (slightly above the saturation dose according to Ref. [64] and 2.5×10^{15} ions/cm². These values correspond to 0.3 and 1.6 ions per surface atom, respectively. The STM images of the patterned 8-ML fcc Fe film are shown in Fig. 8.1, where the inset shows the surface of the as-grown 8-ML fcc Fe film. The surface exhibits almost perfect layer-by-layer growth with rounded islands and no bcc needles (which is typical for the 8 ML Fe surface [64]). For the lower dose of 0.5×10^{15} ions/cm², the irradiated areas are indicated by arrows, and still cannot be easily discerned in the overview scans [Fig. 8.1(a)]. The bcc areas are more easily distinguishable from the fcc surroundings after irradiation with the higher dose of 2.5×10^{15} ions/cm² [Fig. 8.1(b)]. When comparing the scale bar with the 1- μm square lattice of the irradiated spots, note that the scale of the overview scans is not accurate due to the creep and drift of the piezo

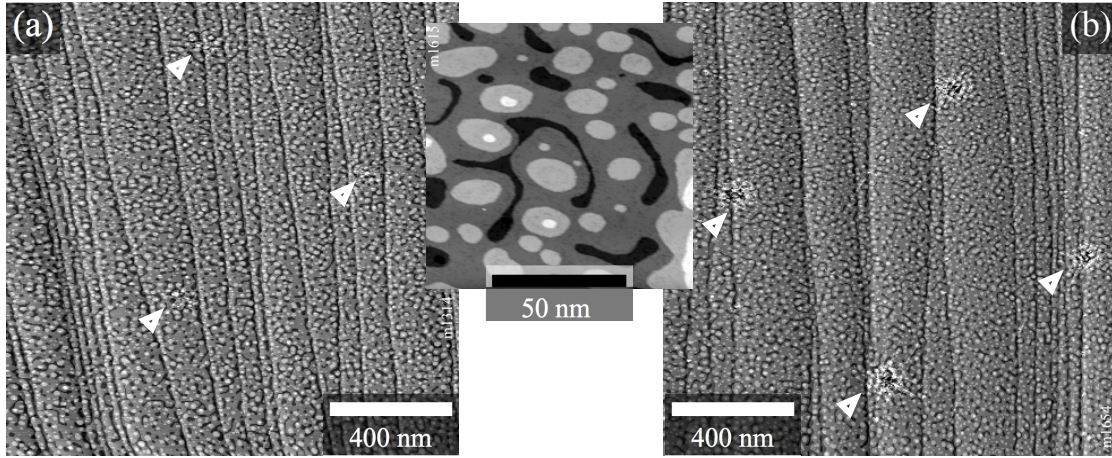


Figure 8.1: STM images of the 8-ML fcc Fe film nano-patterned with Ar^+ ion doses of (a) 0.5×10^{15} ions/cm² and (b) 2.5×10^{15} ions/cm² at 1 keV. The transformed areas are marked by arrows. The inset shows an unirradiated 8 ML fcc Fe film.

tube scanner.

Figures 8.2(b) and (d) show magnification of the irradiated areas for the two different ion doses; 0.5×10^{15} ions/cm² and 2.5×10^{15} ions/cm² respectively. Fig. 8.2(b) is a detail at the edge of the irradiated area in (a) marked by square. The size of the hole in the mask is marked with a dotted circle for visual guidance in both Figs. 8.2(a) and (c). At the higher ion dose [Fig. 8.2(c)], the size of this circle roughly agrees with the area having a reduced thickness due to sputtering (dark area in the centre). At the lower ion dose, sputtering is insufficient to be clearly detected (Assuming a sputter yield of $Y = 2$, only ≈ 0.7 ML are removed).

The STM images also show areas transformed to the bcc structure, which can be easily recognized by their elongated shape (oriented along the close-packed $[011]$ and $[0\bar{1}1]$ directions) and brightness. Their bright appearance is a consequence of 5-10% larger interlayer distance of bcc Fe (110) with respect to fcc Fe(100) [62, 64]. One such bcc needle extending out from a sputtered area in the fcc surrounding is shown in Fig. 8.2(d). Although the atomic lattice in Fig. 8.2(d) is not that of Fe but rather a $c(2 \times 2)$ superstructure (probably due to residual oxygen on surface), the square fcc(100) lattice and the bcc(110) lattice with $74 \pm 1^\circ$ bond angle can be clearly discerned. This value of angle is close to 75° which is the characteristic angle for unrelaxed bcc needles, i.e., bcc needles that still have the same distance of the atomic rows, as in the Cu(100) substrate and the neighboring fcc(100) Fe areas [7, 62]. Due to the higher surface roughness inside the irradiated areas, there we could not take atomically resolved images to determine whether the bcc structure in these areas is relaxed to the bulk bcc lattice or not. But the elongated island shapes and larger apparent height than the surrounding [at least for the low ion dose in Figs. 8.2(a) and (b)]

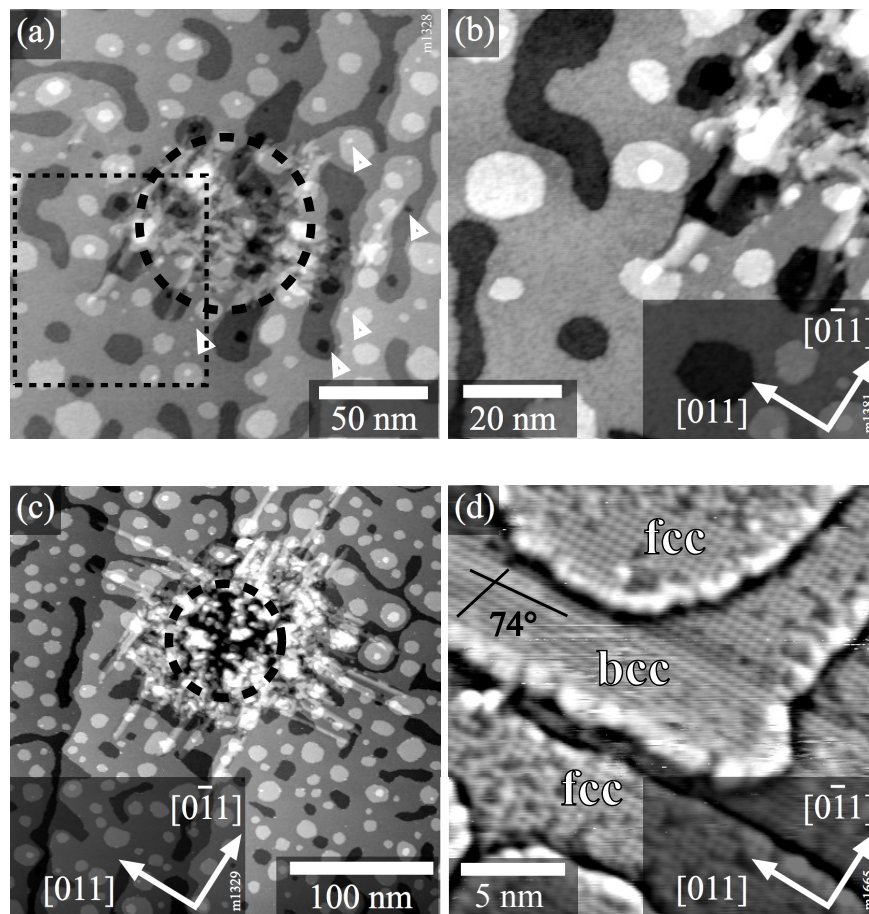


Figure 8.2: STM images of the nano-patterned 8 ML fcc Fe film with an Ar^+ ion dose of (a), (b) 0.5×10^{15} ions/cm² and (c), (d) 2.5×10^{15} ions/cm² at 1 keV. Small arrows in (a) indicate sputter damage outside the nominally irradiated area (broken circle). The area of the magnified view (b) is indicated by the square in (a). Frame (d) shows a bcc needle protruding laterally outwards of a sputtered region. This frame was high-pass filtered to better show the corrugation on the terraces.

clearly indicate that these areas are at least predominately bcc.

At the low ion dose of 0.5×10^{15} ions/cm², we observe that the irradiated area (marked by a broken circle) is not fully transformed. Some obviously unmodified fcc regions reach about 15 nm inside this zone. Also the bcc needles are seen to be slightly protruding out of the marked area with typical length of few nm. A very few needles are also seen with 20 nm length. On the other hand, at high ion dose, some bcc needles are seen to extend out of the irradiated area. We also note an increased roughness around the hole area, with small

monolayer-deep pits and small adatom islands (emphasized by arrows in Fig. 8.2(a)). Far from the irradiated area, these features are absent and also they were not present in the as prepared film. Also, these features are common next to the other nearby irradiated spots. This indicates that the boundary between the irradiated and the untreated area was not sharp in this experiment, possibly due to a particularly large distance between the mask and the surface.

For the high-dose experiment [Fig. 8.2(c)], we do not observe any indications of sputtering beyond the areas transformed to bcc. This indicates that the boundary between the irradiated and unirradiated area must have been rather sharp and the density of stray ions impinging outside must have been rather low, in agreement with our estimate presented above. Nevertheless, the typical length of bcc needles outside the sputtered area is up to ≈ 100 nm, and the border between the fcc and bcc areas is not sharp. This frame was high-pass filtered to better show the corrugation on the terraces.

8.2.2 22 ML fcc Fe film

Figure 8.3(a) shows the STM image of the CO-stabilized 22-ML Fe film discussed in detail in chapter 6 [65]. Again, we have chosen the optimum energy for the fcc-bcc transformation of these films; the ion dose of 1×10^{15} ions/cm² was almost twice the saturation dose. The surface of the as-grown 22 ML film shows layer-by-layer growth with rectangular step edges and no transformation [Fig. 8.3(a)]. The crystallographic directions [011] and $[0\bar{1}1]$ are marked. The irradiated spots [Fig. 8.3(b)] are clearly visible in the overview images, which can be explained by the larger height difference between bcc and fcc areas compared to the 8-ML films. The magnified image of the transformed region [Fig. 8.3(c)] shows dark and bright areas, very similar to the previous results with uniform irradiation of the films (chapter 6). The typical width of the bright bcc areas was found to be between 5 and 15 nm [65]. As described in chapter 6 [65], the dark areas between and around the bright bcc areas are not fcc, but also bcc, as evidenced by the wedge-like structures typical for the Pitsch orientation of bcc Fe as shown in Fig. 8.3(d) [33].

Similar to the 8-ML films, the bcc area is significantly larger than the size of the hole in the mask (dotted circle). The fcc-bcc border is far from the marked circle (drawn to imitate the mask hole), with bcc fingers extending out of the marked circle. Again, the fcc areas between these bcc fingers show no evidence of ion irradiation. Due to increased roughness inside the transformed (bright) areas, atomically resolved images with STM were almost impossible.

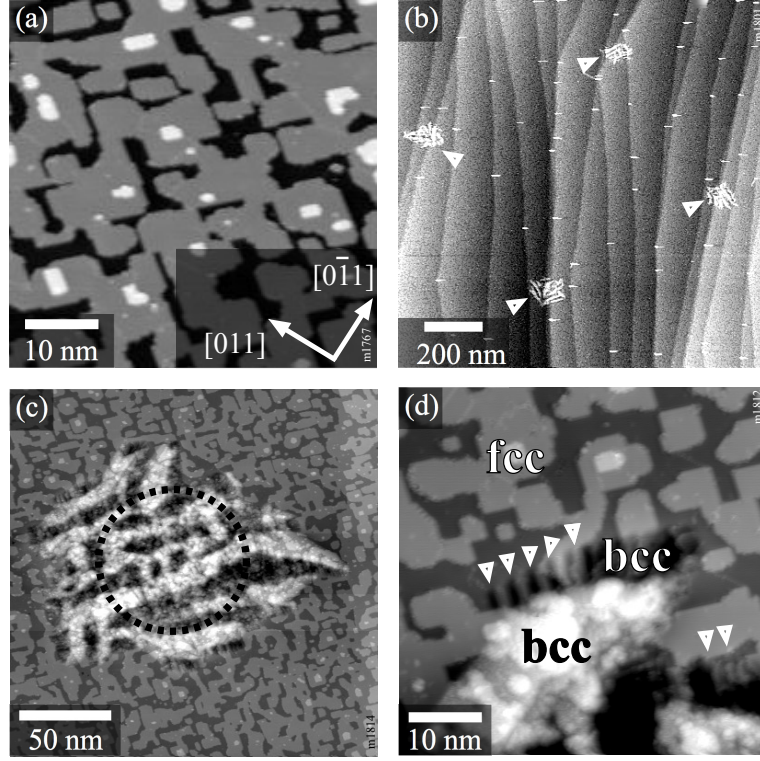


Figure 8.3: STM images of the 22-ML fcc Fe film grown in CO and patterned with an Ar^+ ion dose of 1.0×10^{15} ions/cm² at 2 keV: (a) as prepared surface in CO (b) overview image with the transformed areas (marked by arrows). (c) Magnified image of an irradiated area. (d) Zoom-in on the edge of a bcc area. Wedges of Pitsch-oriented bcc Fe are highlighted with white arrows.

8.3 Discussion

In both the 8-ML and the 22-ML films, growth of the ferromagnetic bcc structure outside the irradiated areas limits the resolution of the nano-patterning process. For the 8-ML films, we have shown that the spatial resolution is better at the lower ion dose of 0.5×10^{15} ions/cm² than far above the threshold dose, even though the irradiated area had no sharp boundary in the 8-ML experiment. This effect is similar to conventional lithography techniques: in photolithography, the irradiation has no sharp borders due to diffraction; in electron lithography, electron backscattering leads to a halo of weaker irradiation surrounding the electron beam [136]. Over-exposure of ion irradiation thus leads to enlargement (blooming) of the area receiving sufficient exposure.

In our case, we need not care about lateral spreading of the ions in the sample (SRIM calculations give a lateral spreading of only 0.7 nm for 1 keV and 1 nm for 2 keV ion

energy) [91]. As mentioned previously, we have to care much more about factors limiting the sharpness of the irradiation pattern. The Cu crystal is not perfectly flat, thus the mask touches the surface in only a few points and will have a distance of a few micrometers from the surface in most places. For the well-collimated part of the ion beam, this implies that the edge of the mask will be projected onto the surface with slight blurring, the transition between the unirradiated and irradiated area should be much smaller than the hole diameter in most cases [Fig. 8.1(a) obviously being an exception]. There is also a halo of badly collimated ions or atoms due to gas-phase scattering, with an intensity $\leq 10^{-3}$ of the main beam. If these stray ions or atoms are distributed over a larger surface area than the hole diameter in the mask, the flux will be further reduced by a factor corresponding to the area spread. The low flux of stray ions is also confirmed by the absence of any signs of sputtering (roughness, vacancy, or adatom islands) outside the hole area in Figs. 8.2(c) and 8.3(c,d). Thus, even for the case of the high dose irradiation shown in Fig. 8.2(c,d), the flux of stray ions outside the projected hole area will be far below 1% of the saturation dose for the fcc-bcc transformation.

We have discussed previously in section 6.8 that ion-induced nucleation of a bcc nucleus is a very rare event [65], which clearly rules out nucleation of new bcc nuclei by stray ions. The situation may be different for growth of already existing nuclei, however: previous experiments have shown bcc needles with ≈ 400 nm length already at an ion dose of 1.9×10^{13} ions/cm² [64]. Assuming linear growth of the bcc needles with ion dose, this would correspond to about 20 nm needle growth with the maximum dose of stray ions conceivable for Fig. 8.2(c) ($\approx 2 \times 10^{12}$ ions/cm²). The actual length of the bcc needles beyond the hole area, i.e., in the area where only stray ions may impinge on the surface, is much larger, however (≈ 100 nm). This difference does not invalidate our view of the stray ions being at least partly responsible for the growth of the bcc needles beyond the area of the hole in the mask: the bcc needles are not independent of their surrounding; the lattice distortion induced by a local fcc-bcc transformation will facilitate the transformation in nearby regions. Of course, the same mechanism will also occur without stray ions, i.e., some of the bcc needles will grow spontaneously beyond the sputtered area, similar to the (rare) spontaneously formed bcc needles in metastable unirradiated films [62]. The strain field caused by ion impact and by the fcc-bcc transformation in the main irradiated area may also contribute to this effect. Due to the rather thin films [1.4 nm for 8 ML Fe/Cu(100)], the strain should be negligible at lateral distances of tens of nanometers or more, so it will promote the fcc-bcc transformation only in a close vicinity of the source of the strain.

8.4 Magnetic Force Microscopy

As these ferromagnetic structures are very small, and occupy only a negligible fraction of the whole sample surface, SMOKE is not a good option to explore the magnetic behavior

of these magnetic nano-patterns. Therefore, to verify the ferromagnetic character of the regions transformed to the bcc structure, we conducted a magnetic force microscopy (MFM) measurement on the Au-coated nano-patterned surface. Due to the soft-magnetic character of the films, [64] a high-coercivity MFM tip was used. MFM images were acquired with the tip lifted 50 nm above the mean tip height in the previous intermittent-contact scan line. When taking the vibration amplitude into account, this corresponds to an average tip height of ≈ 100 nm above the surface. For the MFM images, a sample with 8 ML fcc Fe/Cu(100) was irradiated through the mask with 0.5×10^{15} ions/cm² Ar⁺ ions at 1 keV. Thereafter, the sample was coated with a 2-nm Au film [corresponding to 10 ML Au(111)] to protect it against oxidation during the MFM measurements at ambient conditions. This is different from bombardment through the Au layer discussed before in section 5.4.1. Fig. 8.4 shows an MFM image of this sample, where two ferromagnetic spots separated by a distance of $1\mu\text{m}$ are seen [137]. The image shows the phase and has been slightly smoothed to reduce noise, leading to a granular appearance of the noisy background. The apparent diameter of the spots (at 50%-levels) is about 150 nm, more than what would be expected from the typical size of the bcc area found by STM [cf. Fig. 8.1(a)]. We consider it likely that this is broadening due to the finite resolution of the MFM, determined by the size of the tip and the tip-sample distance. On the other hand, the resolution is somewhat better than that of the MFM data obtained in the previous work by Rupp et al. [64], where $0.11\mu\text{m}$ spots with $0.11\mu\text{m}$ distance in between were hardly seen as separate maxima. We therefore believe that the limited resolution in this work was not only due to the MFM, but also due to other limitations. A prime candidate is the limited depth of focus of the ion lithography machine used in Ref. [64], which strongly affects the resolution on the uneven Cu single crystal.

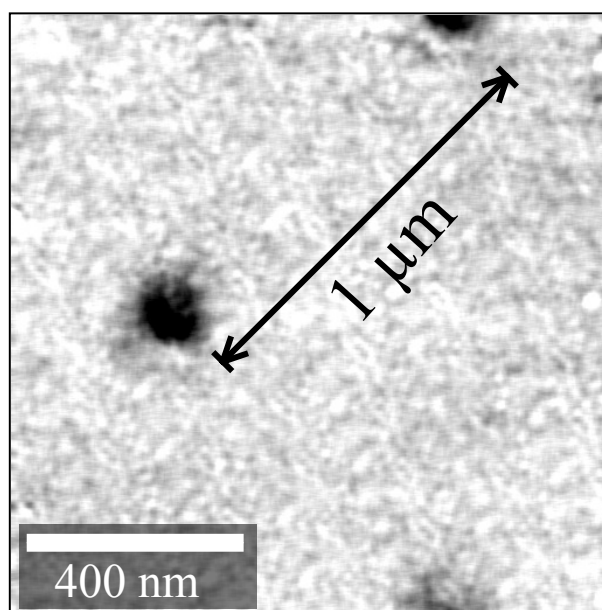


Figure 8.4: MFM image of the 8-ML fcc Fe film patterned with an Ar^+ ion dose of $0.5 \times 10^{15} \text{ ions/cm}^2$ and coated with Au.

Chapter 9

Conclusion

9.1 Conclusion

In this thesis we have worked to develop a better understanding of the structural and magnetic behavior of the Fe films grown on Cu(100) in UHV at room temperature. This work is basically an extension of the work by Rupp et al. We conducted selected STM experiments for 8-ML fcc Fe films with different noble ion gases to understand the SMOKE results presented by Rupp et al. We found better efficiency for heavier ions than for lighter ions at any ion energy. At higher ion energies, lighter ions have poor efficiency due to Fe-Cu intermixing. We also showed that the fcc-bcc transformation can be observed in 2 nm Au coated 8 ML Fe films by ion irradiation by STM.

We have successfully stabilized 22-ML-thick fcc Fe films on Cu(100) at RT by growing films in suitable CO background pressures. AES data suggest that carbon and oxygen play an important role to stabilize the bulk and surface stability of the film, respectively. STM images show layer-by-layer growth; STM and LEED also confirm the fcc(100) structure of these films.

Irradiation with Ar^+ ion causes the film to transform from fcc to bcc. Elongated wavy bcc crystallites are easily recognized in the STM images as protruding (bright) structures. Also, the dark areas next to the needles, lower than the fcc areas are also found to be bcc. The transformation was confirmed by the appearance of bcc spots in the LEED image. SMOKE measurements showed that the structural transformation is accompanied by a magnetic transformation from paramagnetic (fcc Fe) to ferromagnetic (bcc Fe). Coercivity decreased rapidly with Ar^+ ion fluences for all Ar^+ ion energies. The transformation rate was found to depend on the Ar^+ ion energy. For these films, the fastest transformation was observed for 2 keV Ar^+ . At higher energies, Fe-Cu intermixing at the interface impedes

the transformation. Low number of bcc nucleation sites is true for all films i.e., 8, 22 and 44 ML films. We have proposed that the process responsible for bcc nucleation is recrystallization of the small molten volume by ion impact (thermal spike).

We also showed that these films could be coated with Pd and Au; Au grows in an almost layer-by-layer fashion and possibly causes the fcc-bcc transformation of a small fraction of a film already on the verge of the transformation. The ion-induced transformation is possible by bombarding the Au-coated film.

We were also successful in stabilizing a thicker fcc Fe film, which was 44 ML thick by alloying with Ni. In our co-deposition experiments, Ni concentration being the main stabilizing agent in the fcc film, was difficult to reproduce due to its dependence on the rates of evaporation of Fe and Invar evaporators. We found that fcc Fe film can be stabilized if the Ni concentration is close to $\approx 15.1\%$. Transformation from fcc Fe to bcc Fe was observed by Ar^+ irradiation at 2 keV. Monitoring carefully the evaporation rates of Invar and Fe during evaporation, this technique promises even thicker films. Anyhow, these experiments could be useful for any future research on this system.

We have presented a method for in-situ magnetic nano-patterning of fcc Fe films grown on Cu(100) in ultrahigh vacuum. 8 and 22-ML fcc Fe films were irradiated by Ar^+ ions through a SiN mask. Structural analysis of these nano-patterned surfaces was conducted by STM, and magnetic behavior was explored by conducting MFM on a gold-coated fcc Fe film. We could show that the irradiated areas are transformed to the ferromagnetic bcc structure, but there are also bcc needles emanating from the main irradiated area. This effect might be partly due to stray ions, but also strain-induced growth of the bcc needles in the metastable fcc films is expected to play a role. The formation of these bcc areas limits the resolution of the nano-patterning method. When overexposure is avoided, there are hardly any bcc needles extending by more than 20 nm from the border of the irradiated area in the 8-ML films. The resolution is somewhat lower for the 22-ML films grown in CO, where a spread of ≈ 40 nm of the fcc-bcc border was obtained.

List of Figures

1.1	The Fe-Phase diagram [44–46].	2
1.2	correlation between the structural and magnetic properties of Fe as a function of film thickness (a) magnetic moment and curie temperature as a function of Fe film thickness [16], (b) bulk ferromagnetism is observed with strained bcc having nanomartensitic structure [7, 16, 39, 58], (c) at RT; films are paramagnetic with fcc and below RT; surface magnetism is observed [16, 51, 59–62] (d) above 10 ML, films show bulk ferromagnetism with relaxed bcc phase [63].	4
2.1	Schematic view of the processes occurring during film growth: (1) evaporated atoms, (2) atom diffusing to a cluster, (3) 2D cluster, (4) atom dissociating from the cluster, (5) cluster nucleation, (6) atom diffusing on the substrate surface, (7) atom re-evaporating from the surface, (8) re-evaporation from a 3D cluster, (9) atom diffusing to step edge or (10) to kink.	7
2.2	(a) Schematic view of the three growth modes: (a) Frank-van der Merwe growth mode (FM), (b) Stransky-Krastanov growth mode (SK) (c) Volmer-Weber growth mode (VW)	9
2.3	simplified view of the deposited material on the substrate surface, where γ_S , γ_{SF} and γ_F are the surface tension between substrate and vacuum interface, substrate and film interface, and between vacuum and film interface respectively.	9
2.4	Magnetization versus applied magnetic field, (a) diamagnetic system and (b) a paramagnetic system. The arrow show the direction of increasing and decreasing applied magnetic field.	11
2.5	Hysteresis loop of a ferromagnetic material.	13
2.6	Energy as a function of angle for single domain particle	16
2.7	Magnetic field energy reduced by formation of domains [72, 74].	17
2.8	Types of domain walls (a) Bloch wall (b) Néel wall [72, 74].	17

2.9	Schematic view of the ion-surface interaction: showing electronic and nuclear energy loss of an ion [57].	18
2.10	Ion-surface interaction: showing sputtering process.	21
2.11	melt outflow model: (A) sketch of the ion-surface interaction showing (a) incoming ion, (b) molten volume, (c) solid substrate. Outflow of the material from the molten volume onto the surface is labelled by arrows. (B) After few picoseconds (d) atoms onto the surface form vacancy clusters, (e) the melt freezes out. The arrows pointing in the centre of molten volume show the direction of re-crystallization [90].	23
3.1	(a) One-dimensional rectangular potential barrier caused by different work functions of the tip (ϕ_T) and the sample (ϕ_S). The tunnel effect causes electrical equilibrium between tip and sample (if no additional voltage is applied) for sufficiently small distances between tip and sample. The Fermi level of both surfaces are at the same energy and the electrons have no preferred tunneling direction. (b) Direction of the tunneling current when a negative voltage V is applied to the sample.	26
3.2	One-dimensional rectangular potential barrier and resulting wave function. . . .	27
3.3	Model of a spherical tip and the s-states which are one of the solutions of the time independent Schrödinger equation for a spherically symmetric potential.	29
3.4	Scattering of a plane wave at a one dimensional periodic lattice [97].	31
3.5	Energy level diagram of an Auger process. Electron from E_2 drops into the E_1 level with the emission of an E_3 electron [95, 97].	32
3.6	Schematic view of the Faraday (transmitted-light) and Kerr (reflected-light) effects.	34
3.7	Geometrical representation of Kerr angle ' θ ' (the real part of complex angle) and the ellipticity ' ε ' (the imaginary part of the complex angles). ' θ ' is related to the major axis of the ellipse whereas ' ε ' is related to the minor to major axis ratio. .	35
3.8	(a) Polar: \vec{M} perpendicular to sample plane and parallel to plane of incidence, (b) Longitudinal: \vec{M} parallel to sample plane and plane of incidence, (c) Transversal: \vec{M} parallel to sample plane and perpendicular to the plane of incidence	36
4.1	Schematic view of the RT-STM [102].	38
4.2	Scanning electron micrographs showing the mask with different magnifications. Frame (a) shows the carrier; the membrane appears dark in the center of the image.	40
4.3	(a) Schematic view of the experimental set-up for patterning. (b) view of the cone with mask glued at the lower side (c) the cone plus mask placed on the fcc Fe/Cu(100) film and bombarded with Ar^+ ions. (d) the patterned film after removing the mask.	40

4.4	Schematic view of the Smoke Setup [57].	42
5.1	Calculated number of involved atoms N_m in molten volume as a function of ion energy for 8-ML-thick fcc Fe film on Cu-substrate for different ions: (a) He^+ , (b) Ne^+ , (c) Ar^+ , (d) Kr^+ , (e) Xe^+ ions. Each graph is marked with small schematic diagrams for low and high ion energies showing the size and penetration depth for respective ions at respective energies.	46
5.2	Longitudinal Kerr ellipticity at saturation value, ε_{sat} , and coercive field H_c are plotted as a function of ion dose for 8-ML thick fcc Fe film grown on Cu(100) and irradiated with: (a) Ne^+ , (b) Ar^+ , (c) Kr^+ , and (d) Xe^+ ions. Data from Ref. [57]	47
5.3	Normalized longitudinal Kerr ellipticity signal at saturation value, ε_{sat} , as a function of ion dose for different gases at (a) 500 eV, (b) 1 keV, and (c) 3 keV. Data from Ref. [57, 64]	48
5.4	STM images of 8 ML fcc Fe film irradiated with 500 eV Ar^+ ion energy with doses of: (a) as-prepared film, (b) $2.3 \times 10^{14} \text{ cm}^{-2}$ (c) $4.5 \times 10^{14} \text{ cm}^{-2}$, (d) $6.8 \times 10^{14} \text{ cm}^{-2}$	51
5.5	STM images of 8 ML fcc Fe film irradiated with 500 eV Xe^+ ion energy with doses of (a) as-prepared film, (b) $3.9 \times 10^{13} \text{ cm}^{-2}$, (c) $7.8 \times 10^{13} \text{ cm}^{-2}$, (d) $1.2 \times 10^{14} \text{ cm}^{-2}$, (e) $1.56 \times 10^{14} \text{ cm}^{-2}$, (f) $1.95 \times 10^{14} \text{ cm}^{-2}$	52
5.6	STM images of 8 ML fcc Fe film (a) irradiated with 3 keV Ar^+ ion energy with doses of: (b) $1.9 \times 10^{14} \text{ cm}^{-2}$, (c) $4.7 \times 10^{14} \text{ cm}^{-2}$, (d) $9.5 \times 10^{14} \text{ cm}^{-2}$	53
5.7	STM images of 8 ML fcc Fe film irradiated with 3 keV Xe^+ ion energy with doses of (a) as-prepared film, (b) $5 \times 10^{13} \text{ cm}^{-2}$, (c) $7.8 \times 10^{13} \text{ cm}^{-2}$, (d) $1.1 \times 10^{14} \text{ cm}^{-2}$	54
5.8	STM images of 8 ML fcc Fe film irradiated with 2 keV Ne^+ ion energy with doses of (a) as-prepared film, (b) $1 \times 10^{15} \text{ cm}^{-2}$, (c) $2 \times 10^{15} \text{ cm}^{-2}$	55
5.9	(a) STM image of the 8 ML Fe film, (b) Au coated 8 ML Fe film surface, (c) frame (b) after processing shows the underlying fcc islands marked by dotted ellipsoids as well as Au herringbone structures, (d) Atomically resolved Au surface showing Au(111), (e) the section profile over the marked area in (d) reveals a step height of $\approx 235 \text{ pm}$	59
5.10	Schematic view of the Au layers on Fe/Cu(100) to show the underlying Fe islands. The difference of $\sim 55 \text{ pm}$ between Au and Fe layers is maintained up to the top Au layer.	60

5.11	(a) STM image of the Au surface after Ar^+ ion dose of 3.5×10^{14} ions/cm ² at 3 keV, (b) frame (a) after processing (Au layers and noise subtracted) shows stripes along the marked crystallographic directions, pointing towards the transformation of the Au coated Fe film.	60
5.12	Calculated number of atoms N_m in the molten volume for a 1.4 nm Fe film coated with 2 nm Au. The fraction of Cu atoms in the melt is negligible up to 1 keV and increases with the increasing ion energy.	62
6.1	Normalized Auger peak-to-peak heights of carbon and oxygen signals for 22 ML Fe films as a function of CO pressure during evaporation for RT-STM.	66
6.2	Schematic view of the film growth process in the presence of CO.	66
6.3	STM images of a 22 ML Fe film grown with unstable CO pressure during the experiment, leading to a surface with bcc crystallites (bright). Frames (a)-(d) show the same area with increasing magnification. (e) bcc area with an adjacent trough (image shown as if illuminated from the left). The inclined bcc wedges in the trough are indicated with arrows. The section profile (f) over the vertical frame in (e) shows the bcc trough next to the needle.	67
6.4	STM image of the as-grown 22 ML Fe film in the presence of CO. (a) The inset shows the oxygen $c(2 \times 2)$ superstructure highlighted by a white square. The white spot in the inset is probably the missing oxygen atom (white circle). (b) The surface of an 8 ML Fe film grown without CO (shown here for comparison) .	69
6.5	Structure model for the Fe steps of the films grown in CO (top view). The $c(2 \times 2)$ oxygen superstructure is shown only in the upper layer.	69
6.6	Fe film (≈ 23 to 24 ML) grown in CO. (a) STM image of the as-grown surface with partially transformed areas (bright). (b) After dosing atomic hydrogen to remove the surface oxygen.	71
6.7	STM images of a 22 ML Fe film prepared in 7.5×10^{-10} mbar CO. (a) as-grown film, and after 500 eV Ar^+ ion irradiation with ion doses of (b) 1.3×10^{15} cm ⁻² , (c) 1.8×10^{15} cm ⁻² , and (d) 2.4×10^{15} cm ⁻² . Overview images (b)-(d) are high-passfiltered to make the bcc needles more visible in spite of steps in the substrate.	72
6.8	High-resolution STM image of the film in Fig. 6.3 after bombardment with 1 keV Ar^+ ions (dose: 3×10^{14} cm ⁻²). (a) The bcc area in the lower left shows to poorly ordered oxygen while the well-ordered $c(2 \times 2)$ -O structure with its 90° bond angle is clearly seen in the bcc areas. (b) Filtering in the Fourier domain (spots marked in the inset) clearly shows the bcc lattice with a bond angle of $71 \pm 0.5^\circ$	74

6.9	STM images of the 22 ML Fe film irradiated with different Ar^+ ion energies. (a) 500 eV (dose: $9.5 \times 10^{14} \text{ cm}^{-2}$), (b) 2000 eV (dose: $4 \times 10^{14} \text{ cm}^{-2}$), and (c) 4000 eV (dose: $3.6 \times 10^{14} \text{ cm}^{-2}$). Height histograms are shown at the bottom right. .	76
6.10	STM images of the 22 ML Fe film irradiated with 4000 eV Ar^+ ion energy with ion dose of $8 \times 10^{14} \text{ cm}^{-2}$ for slightly different thicknesses of ≈ 22 ML fcc Fe films; film (a) is slightly thicker than the film (b).	76
6.11	(a) LEED image of the as-grown 22 ML Fe film, showing fcc(100) and oxygen $c(2 \times 2)$ spots. (b) After Ar^+ irradiation of $2.4 \times 10^{15} \text{ cm}^{-2}$ at 500 eV, diffuse bcc satellites are visible [the rectangular bcc(110) unit cell is indicated].	78
6.12	Hysteresis loops of the 22-ML Fe films irradiated with 2 keV Ar^+ ions, showing longitudinal Kerr ellipticity ε as a function of magnetic field H . The transformation from paramagnetic (ion dose: 0) to ferromagnetic with increasing ion fluence can be seen.	79
6.13	(a) Saturation value of longitudinal Kerr ellipticity ε_{sat} as a function of Ar^+ ion dose for different ion energies and (b) coercive field H_c as a function of Ar^+ ion dose.	79
6.14	(a) Calculated number of atoms N_m in the molten volume for a 22-ML-thick fcc Fe film. The fraction of Cu atoms in the melt is negligible up to 2 keV and increases with increasing ion energy (b) Schematic view of an arrangement leading to a sheared structure during recrystallization, a possible bcc nucleus.	81
6.15	SRIM output file for a 2 keV Ar^+ ion energy showing ion-energy-absorption profile as a function of target depth with 22-ML Fe (closed circles) and Cu (open circles) atoms.	82
6.16	STM images (strongly high-pass filtered) of the 22 ML fcc Fe film covered with 2.25 nm Pd. (a) Pd grows in (100) orientation in the regions indicated with black arrows and as (111) indicated with white arrows. (b) Most of this area shows (111) growth.	84
6.17	High-pass filtered STM images of the 22 ML fcc Fe film (a) as prepared in 7.5×10^{-10} mbar CO pressure and after deposition of (b) 0.52 nm and (c) 2 nm Au. (d) Surface covered with 2 nm Au after irradiation with $9 \times 10^{14} \text{ cm}^{-2}$ Ar^+ ions at 3 keV.	85
6.18	The calculated number of atoms in the molten volume for 22 ML (4 nm) Fe films coated with 10 ML (2nm) Au for different ion energies.	86
7.1	The magnetic phase diagram of $\text{Fe}_x\text{Ni}_{1-x}$ [116].	88
7.2	STM image of the as-grown 44-ML fcc Fe film with less than 13.1% Ni. The film is already transformed to bcc. The inset shows the complex shape of the bcc areas.	90

7.3	STM images of the 44-ML fcc Fe film with 15.1% Ni concentration irradiated with 2 keV Ar^+ ion energy. (a) As grown 44 ML fcc film, with very few bcc areas. Inset of the image shows layer-by-layer growth. (b) After an Ar^+ ion irradiation of 2.0×10^{14} ions/cm ² , few areas undergo fcc to bcc transformation. (c) The surface of the 44 ML fcc Fe film after Ar^+ ion dose of 6.5×10^{14} ions/cm ² . (d) The film transforms to bcc after an Ar^+ ion dose of 3×10^{15} ions/cm ² with a few patches still fcc.	91
7.4	STM images of the 44 ML fcc Fe film with more than 20.7% Ni concentration. (a) The film grows as fcc with no bcc areas. The inset shows layer-by-layer growth of the film. (b) After Ar^+ ion irradiation of 2.8×10^{15} ions/cm ² at 2 keV, no transformation is observed. The inset shows the sputtered fcc surface after prolonged irradiation.	92
8.1	STM images of the 8-ML fcc Fe film nano-patterned with Ar^+ ion doses of (a) 0.5×10^{15} ions/cm ² and (b) 2.5×10^{15} ions/cm ² at 1 keV. The transformed areas are marked by arrows. The inset shows an unirradiated 8 ML fcc Fe film.	97
8.2	STM images of the nano-patterned 8 ML fcc Fe film with an Ar^+ ion dose of (a), (b) 0.5×10^{15} ions/cm ² and (c), (d) 2.5×10^{15} ions/cm ² at 1 keV. Small arrows in (a) indicate sputter damage outside the nominally irradiated area (broken circle). The area of the magnified view (b) is indicated by the square in (a). Frame (d) shows a bcc needle protruding laterally outwards of a sputtered region. This frame was high-pass filtered to better show the corrugation on the terraces.	98
8.3	STM images of the 22-ML fcc Fe film grown in CO and patterned with an Ar^+ ion dose of 1.0×10^{15} ions/cm ² at 2 keV: (a) as prepared surface in CO (b) overview image with the transformed areas (marked by arrows). (c) Magnified image of an irradiated area. (d) Zoom-in on the edge of a bcc area. Wedges of Pitsch-oriented bcc Fe are highlighted with white arrows.	100
8.4	MFM image of the 8-ML fcc Fe film patterned with an Ar^+ ion dose of 0.5×10^{15} ions/cm ² and coated with Au.	103

Bibliography

- [1] C. Chappert, H. Bernas, J. Ferré, V. Kottler, J. P. Jamet, Y. Chen, E. Cambril, T. Devolder, F. Rousseaux, V. Mathet, and H. Launois, “Planar patterned magnetic media obtained by ion irradiation,” *Science*, vol. 280, p. 1919, 1998.
- [2] B. D. Terris, “Fabrication challenges for patterned recording media,” *J. Magn. Magn. Mater.*, vol. 321, p. 512, 2009.
- [3] B. D. Terris and T. Thomson, “Nanofabricated and self-assembled magnetic structures as data storage media,” *J. Phys. D: Appl. Phys.*, vol. 38, p. R199, 2005.
- [4] C. A. Ross, “patterned magnetic recording media,” *Annu. Rev. Mater. Res.*, vol. 31, p. 203, 2001.
- [5] A. Guedes, J. M. Almeida, S. Cardoso, R. Ferréira, and P. P. Freitas, “Improving magnetic field detection limits of spin valve sensors using magnetic flux guide concentrators,” *IEEE Trans. Magn.*, vol. 43, p. 2376, 2007.
- [6] M. Wuttig and X. Liu, *Ultrathin metal films: magnetic and structural properties*. Springer Verlag, 2004.
- [7] A. Biedermann, R. Tscheliessnig, M. Schmid, and P. Varga, “Local atomic structure of ultra-thin Fe films grown on Cu(100),” *Appl. Phys. A*, vol. 78, p. 807, 2004.
- [8] W. A. Jesser and J. W. Matthews, “Evidence for pseudomorphic growth of iron on copper,” *Philos. Mag.*, vol. 15, p. 1097, 1967.
- [9] M. T. Kief and W. F. Egelhoff Jr., “Growth and structure of Fe and Co thin films on Cu(111), Cu(100), and Cu(110): A comprehensive study of metastable film growth,” *Phys. Rev. B*, vol. 47, p. 10785, 1993.
- [10] D. P. Pappas, K. P. Kämper, and H. Hopster, “Reversible transition between perpendicular and in-plane magnetization in ultrathin films,” *Phys. Rev. Lett.*, vol. 64, p. 3179, 1990.

- [11] C. Liu, E. R. Moog, and S. D. Bader, "Polar Kerr-effect observation of perpendicular surface anisotropy for ultrathin fcc Fe grown on Cu(100)," *Phys. Rev. Lett.*, vol. 60, p. 2422, 1988.
- [12] W. A. A. Macedo and W. Keune, "Magnetism of epitaxial fcc-Fe(100) films on Cu(100) investigated in situ by conversion-electron maussbauer spectroscopy in ultrahigh vacuum," *Phys. Rev. Lett.*, vol. 61, p. 475, 1988.
- [13] D. A. Steigerwald and W. F. Egelhoff Jr., "Epitaxial fcc Fe films on Cu(100)," *Phys. Rev. Lett.*, vol. 60, p. 2558, 1988.
- [14] D. P. Pappas, K. P. Kämper, B. P. Miller, H. Hopster, D. E. Fowler, A. C. Luntz, C. R. Brundle, and Z. X. Shen, "Magnetism of ultrathin films of Fe on Cu(100)," *J. Appl. Phys.*, vol. 69, p. 5209, 1991.
- [15] F. Petroff, A. Barthelemy, D. H. Mosca, D. K. Lottis, A. Fert, P. A. Schroeder, W. P. Pratt Jr, R. Loloee, and S. Lequien, "Oscillatory interlayer exchange and magnetoresistance in Fe/Cu multilayers," *Phys. Rev. B.*, vol. 44, p. 5355, 1991.
- [16] J. Thomassen, F. May, B. Feldmann, M. Wuttig, and H. Ibach, "Magnetic live surface layers in Fe/Cu(100)," *Phys. Rev. Lett.*, vol. 69, p. 3831, 1992.
- [17] P. Xhonneux and E. Courtens, "Direct correlation between the structure and magnetism of thin epitaxial Fe on Cu(100)," *Phys. Rev. B*, vol. 46, p. 556, 1992.
- [18] R. Allenspach and A. Bischof, "Magnetization direction switching in Fe/Cu(100) epitaxial films: Temperature and thickness dependence," *Phys. Rev. Lett.*, vol. 69, p. 3385, 1992.
- [19] T. Kraft, P. M. Marcus, and M. Scheffler, "Atomic and magnetic structure of fcc Fe/Cu(100)," *Phys. Rev. B.*, vol. 49, p. 11511, 1994.
- [20] D. Li, M. Freitag, J. Pearson, Z. Q. Qiu, and S. D. Bader, "Magnetic and structural instabilities of ferromagnetic and antiferromagnetic Fe/Cu(100)," *J. Appl. Phys.*, vol. 76, p. 6425, 1994.
- [21] D. Li, M. Freitag, J. Pearson, Z. Q. Qiu, and S. D. Bader, "Magnetic phases of ultrathin Fegrown on Cu(100) as epitaxial wedges," *Phys. Rev. Lett.*, vol. 72, p. 3112, 1994.
- [22] J. Shen, H. Jenniches, C. V. Mohan, J. Barthel, M. Klaua, P. Ohresser, and J. Kirschner, "In-plane anisotropy and reversed spin reorientation of fcc Fe ultrathin films on Cu(100) by pulsed-laser deposition," *Europhys. Lett.*, vol. 43, p. 349, 1998.

- [23] H. Jenniches, J. Shen, C. V. Mohan, S. S. Manoharan, J. Barthel, P. Ohresser, M. Klaua, and J. Kirschner, "Structure and magnetism of pulsed-laser-deposited ultrathin films of Fe on Cu (100)," *Phys. Rev. B*, vol. 59, p. 1196, 1999.
- [24] D. Schmitz, C. Charton, A. Scholl, C. Carbone, and W. Eberhardt, "Magnetic moments of fcc Fe overlayers on Cu(100) and Co(100)," *Phys. Rev. B*, vol. 59, p. 4327, 1999.
- [25] K. Amemiya, S. Kitagawa, D. Matsumura, H. Abe, T. Ohta, and T. Yokoyama, "Direct observation of magnetic depth profiles of thin Fe films on Cu(100) and Ni/Cu(100) with the depth-resolved x-ray magnetic circular dichroism," *Appl. Phys. Lett.*, vol. 84, p. 936, 2004.
- [26] H. Magnan, D. Chandesris, B. Vilette, O. Heckmann, and J. Lecante, "Structure of thin metastable epitaxial Fe films on Cu(100): Reconstruction and interface ordering by coating," *Phys. Rev. Lett.*, vol. 67, p. 859, 1991.
- [27] D. Qian, X. F. Jin, J. Barthel, M. Klaua, and J. Kirschner, "Spin-density wave in ultrathin Fe films on Cu(100)," *Phys. Rev. Lett.*, vol. 87, p. 227204, 2001.
- [28] D. A. Steigerwald, I. Jacob, and W. F. Egelhoff Jr., "Structural study of the epitaxial growth of fcc-Fe films, sandwiches, and superlattices on Cu(100)," *Surf. Sci.*, vol. 202, p. 472, 1988.
- [29] M. Onellion, M. A. Thompson, J. L. Erskine, C. B. Duke, and A. Paton, "Epitaxial growth of fcc Fe on Cu(100)," *Surf. Sci.*, vol. 179, p. 219, 1987.
- [30] W. Daum, C. Stuhlmann, and H. Ibach, "Displacive phase transition and surface-phonon anomalies in fcc Fe films on Cu(100)," *Phys. Rev. Lett.*, vol. 60, p. 2741, 1988.
- [31] P. Bayer, S. Müller, P. Schmailzl, and K. Heinz, "Nonpseudomorphic and surface-reconstructed ultrathin epitaxial fcc Fe films on Cu(100)," *Phys. Rev. B*, vol. 48, p. 17611, 1993.
- [32] K. E. Johnson, D. D. Chambliss, R. J. Wilson, and S. Chiang, "Growth and morphology of partial and multilayer Fe thin films on Cu(100) and the effect of adsorbed gases studied by scanning tunneling microscopy," *J. Vac. Sci. Technol. A*, vol. 11, p. 1654, 1993.
- [33] K. Kalki, D. D. Chambliss, K. E. Johnson, R. J. Wilson, and S. Chiang, "Evidence for martensitic fcc-bcc transition of thin Fe films on Cu(100)," *Phys. Rev. B*, vol. 48, p. 18344, 1993.
- [34] M. Wuttig and J. Thomassen, "Structure determination for Fe films on Cu(100)," *Surf. Sci.*, vol. 282, p. 237, 1993.

- [35] P. Schmailzl, K. Schmidt, P. Bayer, R. Döll, and K. Heinz, "The structure of thin epitaxial Fe films on Cu(100) in the transition range fcc→bcc," *Surf. Sci.*, vol. 312, p. 73, 1994.
- [36] H. Zillgen, B. Feldmann, and M. Wuttig, "Structural and magnetic properties of ultrathin Fe films deposited at low temperature on Cu(100)," *Surf. Sci.*, vol. 321, p. 32, 1994.
- [37] S. Müller, P. Bayer, C. Reischl, K. Heinz, B. Feldmann, H. Zillgen, and M. Wuttig, "Structural instability of ferromagnetic fcc Fe films on Cu(100)," *Phys. Rev. Lett.*, vol. 74, p. 765, 1995.
- [38] M. Straub, R. Vollmer, and J. Kirschner, "Surface magnetism of ultrathin γ -Fe films investigated by nonlinear magneto-optical Kerr effect," *Phys. Rev. Lett.*, vol. 77, p. 743, 1996.
- [39] A. Biedermann, R. Tscheliessnig, M. Schmid, and P. Varga, "Crystallographic structure of ultrathin Fe films on Cu(100)," *Phys. Rev. Lett.*, vol. 87, p. 86103, 2001.
- [40] D. D. Chambliss and K. E. Johnson, "Nucleation with a critical cluster size of zero: Submonolayer Fe inclusions in Cu(100)," *Phys. Rev. B*, vol. 50, p. 5012, 1994.
- [41] J. Giergiel, J. Shen, J. Woltersdorf, A. Kirilyuk, and J. Kirschner, "Growth and morphology of ultrathin Fe films on Cu(001)," *Phys. Rev. B*, vol. 52, no. 11, p. 8528, 1995.
- [42] H. L. Meyerheim, R. Popescu, D. Sander, J. Kirschner, O. Robach, and S. Ferrér, "Layer relaxation and intermixing in Fe/Cu(001) studied by surface x-ray diffraction," *Phys. Rev. B*, vol. 71, p. 035409, 2005.
- [43] H. Landskron, G. Schmidt, K. Heinz, K. Müller, C. Stuhlmann, U. Beckers, M. Wuttig, and H. Ibach, "Low-temperature $p2mg(2\times 1)$ structure of ultrathin epitaxial films Fe/Cu(100)," *Surf. Sci.*, vol. 256, p. 115, 1991.
- [44] R. Boehler, "Temperatures in the earth's core from melting-point measurements of iron at high pressures," *Nature*, vol. 363, p. 534, 1993.
- [45] S. K. Saxena, G. Shen, and P. Lazor, "Experimental evidence for a new iron phase and implications for earth's core," *Science*, vol. 260, p. 1312, 1993.
- [46] L. S. Dubrovinsky, S. K. Saxena, and P. Lazor, "X-ray study of iron with heating at ultra-high pressure," *Geophys. Res. Lett.*, vol. 24, p. 1835, 1997.
- [47] A. Kirilyuk, J. Giergiel, J. Shen, and J. Kirschner, "Unusual surfactant effect and the stability of pseudomorphic gamma-Fe films," *Phys. Rev. B*, vol. 52, p. R11672, 1995.

- [48] A. Kirilyuk, J. Giergiel, J. Shen, M. Straub, and J. Kirschner, "Growth of stabilized gamma-Fe films and their magnetic properties," *Phys. Rev. B*, vol. 54, p. 1050, 1996.
- [49] R. Hallbauer and U. Gonser, "Antiferromagnetism of fcc iron films," *J. Magn. Magn. Mat.*, vol. 35, p. 55, 1983.
- [50] D. Pescia, M. Stampanoni, G. L. Bona, A. Vaterlaus, R. F. Willis, and F. Meier, "Magnetism of epitaxial fcc iron films on Cu(001) investigated by spin-polarized photoelectron emission," *Phys. Rev. Lett.*, vol. 58, p. 2126, 1987.
- [51] A. Biedermann, R. Tscheliessnig, C. Klein, M. Schmid, and P. Varga, "Reconstruction of the clean and H covered "magnetic live surface layer" of Fe films grown on Cu(100)," *Surf. Sci.*, vol. 563, p. 110, 2004.
- [52] M. F. Onellion, C. L. Fu, M. A. Thompson, J. L. Erskine, and A. J. Freeman, "Electronic structure and properties of epitaxial Fe on Cu(100): theory and experiment," *Phys. Rev. B*, vol. 33, p. 7322, 1986.
- [53] T. Asada and S. Blügel, "Total energy spectra of complete sets of magnetic states for fcc-Fe films on Cu(100)," *Phys. Rev. Lett.*, vol. 79, p. 507, 1997.
- [54] R. E. Camley and D. Li, "Theoretical calculation of magnetic properties of ultrathin Fe films on Cu(100)," *Phys. Rev. Lett.*, vol. 84, p. 4709, 2000.
- [55] S. S. A. Razee, J. B. Staunton, L. Szunyogh, and B. L. Gyorffy, "Onset of magnetic order in fcc-Fe films on Cu(100)," *Phys. Rev. Lett.*, vol. 88, p. 147201, 2002.
- [56] D. Spisák and J. Hafner, "Shear instability of gamma-Fe in bulk and in ultrathin films," *Phys. Rev. Lett.*, vol. 88, p. 056101, 2002.
- [57] W. Rupp, "Ionenstrahl induzierter Ferromagnetismus von dünnen Fe Schichten auf Cu(100)," *Dissertation, IAP, TU Wien*, 2008.
- [58] A. Biedermann, "Stability of the nanomartensitic phase in ultrathin Fe films on Cu(100)," *Phys. Rev. B*, vol. 80, p. 235403, 2009.
- [59] G. Rauchbauer, A. Buchsbaum, H. Schiechl, P. Varga, M. Schmid, and A. Biedermann, "Ultra-thin Fe films grown on Cu by pulsed laser deposition: Intermixing and bcc-like structures," *Surf. Sci.*, vol. 602, p. 1589, 2008.
- [60] C. Egawa, E. M. McCash, and R. F. Willis, "Adsorption of hydrogen on thin fcc-iron films grown on Cu(100)," *Surface Science*, vol. 215, p. L271, 1989.
- [61] S. Müller, P. Bayer, A. Kinne, P. Schmailzl, and K. Heinz, "High precision LEED structure analysis of ultra-thin epitaxial fcc Fe films on Cu(100)," *Surf. Sci.*, vol. 322, p. 21, 1995.

- [62] A. Biedermann, M. Schmid, and P. Varga, "Nucleation of bcc iron in ultrathin fcc films," *Phys. Rev. Lett.*, vol. 86, p. 464, 2001.
- [63] T. Detzel, N. Memmel, and T. Fauster, "Growth of ultrathin iron films on Cu(001): an ion-scattering spectroscopy study," *Surf. Sci.*, vol. 293, p. 227, 1993.
- [64] W. Rupp, A. Biedermann, B. Kamenik, R. Ritter, C. Klein, E. Platzgummer, M. Schmid, and P. Varga, "Ion-beam induced fcc-bcc transition in ultrathin Fe films for ferromagnetic patterning," *Appl. Phys. Lett.*, vol. 93, p. 063102, 2008.
- [65] S. Shah Zaman, H. Ossmer, J. Jonner, Z. Novotny, A. Buchsbaum, M. Schmid, and P. Varga, "Ion-beam-induced magnetic transformation of CO-stabilized fcc Fe films on Cu(100)," *Phys. Rev. B.*, vol. 82, p. 235401, 2010.
- [66] S. A. Kukushkin and A. V. Osipov, *Nucleation Theory and Applications*. Germany: WILEY-VCH, 2005.
- [67] E. Bauer, "Epitaxy of metals on metals," *Appl. Surf. Sci.*, vol. 11/12, p. 479, 1982.
- [68] F. C. Frank and J. H. van der Merwe *Proc. Roy. Soc. A*, vol. 198, p. 205, 1949.
- [69] J. N. Stranski and L. Krastanov *Ber. Akad. Wiss. Wien*, vol. 146, p. 797, 1938.
- [70] M. Volmer and A. Weber *Z. Phys. Chem.*, vol. 119, p. 6274, 1981.
- [71] N. W. Ashcroft and N. D. Mermin *Solid State Physics*, Thomson Learning Inc, 1976.
- [72] Chikazumi, *Physics of magnetism*. USA: John Wiley and Sons, 1964.
- [73] B. D. Cullity and C. D. Graham, *Introduction to magnetic materials*. USA: John Wiley and Sons, Inc., 2009.
- [74] C. Kittel, *Introduction to solid state Physics*. USA: John Wiley and Sons, 7th ed., 1996.
- [75] L. Néel, "Theorie du trainage magnetique des ferromagnetiques engrains fins avec application aux terrescluites," *Ann. Geophys.*, vol. 5, p. 99, 1949.
- [76] N. A. Spaldin, *Magnetic Materials*. UK: Cambridge University Press, 2003.
- [77] edited by D. Gignoux and M. Schlenker, *Magnetism Fundamentals*. USA: Springer, 2005.
- [78] W. Schilling and H. Ullmaier, "Physics of radiation damage in metals," *Materials, Science, and Technology*, edited by R. W. Cahn, P. Haasen, and K. Kramer (*Chemie, Weinheim, 1993*), vol. 10, p. 180.
- [79] M. Nastasi, J. W. Mayer, and J. K. Hirvonen, *Ion-solid interactions: fundamentals and applications*. UK: Cambridge University press, 1996.

- [80] T. B. Massalski, "Binary alloy phase diagrams," *ASM International*, p. 1408, 1990.
- [81] S. H. M. R. Ghassemi, A. Shokuhfar, and M. R. Vaezi, "Microstructure evaluation of solid-solution in Fe-Cu immiscible alloy system," *Defect and Diffusion Forum*, vol. 273, p. 622, 2008.
- [82] P. J. Schilling, V. Palshin, R. C. Tittsworth, J. H. He, and E. Ma, "Overlapping solid solubility in mechanically alloyed Fe-Ni and Fe-Cu," *Phys. Rev B*, vol. 68, p. 224204, 2003.
- [83] G. W. Yang, W. S. Lai, C. Lin, and B. X. Liu, "Irradiation-induced growth of nanoquasicrystals from amorphous matrix in the equilibrium immiscible Fe-Cu system," *Appl. Phys. Lett.*, vol. 74, p. 3305, 1999.
- [84] P. Sigmund, "Energy density and time constant of heavy-ion-induced elastic-collision spikes in solids," *Appl. Phys. Lett.*, vol. 25, p. 169, 1974.
- [85] P. Sigmund, "Sputtering from elastic-collision spikes in heavy-ion-bombarded metals," *Journal of Applied Physics*, vol. 52, p. 990, 1981.
- [86] W. Bolse, "Mechanisms of ion beam induced atomic mixing in solids," *Mat. Sci. Eng. A*, vol. 253, p. 194, 1998.
- [87] G. Yang, W. Lai, C. Lin, and B. X. Liu, "Metastable phases induced by ion irradiation in the equilibrium immiscible Fe-Cu system," *J. Appl. Phys.*, vol. 87, p. 7232, 2000.
- [88] W. L. Johnson, Y. T. Cheng, M. van Rossum, and M. A. Nicolet, "When is thermodynamics relevant to ion-induced atomic rearrangements in metals?," *Nucl. Inst. Meth. B*, vol. 7/8, p. 657, 1995.
- [89] M. Ghaly and R. S. Averback, "Effect of viscous flow on ion damage near solid surfaces," *Phys. Rev. Lett.*, vol. 72, p. 364, 1994.
- [90] C. Busse, H. Hansen, U. Linke, and T. Michely, "Atomic layer growth on Al(111) by ion bombardment," *Phys. Rev. Lett.*, vol. 85, p. 326, 2000.
- [91] <http://www.srim.org/>.
- [92] G. Binnig, H. Rohrer, C. Gerber, and E. Weibel, "Tunneling through a controllable vacuum gap," *Appl. Phys. Lett.*, vol. 40, p. 178, 1982.
- [93] G. Binnig and H. Rohrer, "Scanning tunneling microscopy," *Surf. Sci.*, vol. 126, p. 236, 1983.
- [94] J. A. Stroscio and W. J. Kaiser, *Methods of Experimental Physics, Scanning Tunneling Microscopy*, vol. 27. Boston: Academic press, 1993.

- [95] D. P. Woodruff and T. A. Delchar, *Modern techniques of Surface Science*. Cambridge University Press, 2nd ed., 1994.
- [96] C. J. Chen, *Introduction to Scanning Tunneling Microscopy*. New York: Oxford University Press, 1993.
- [97] J. C. Vickerman and I. S. Gilmore, *Surface Analysis-The Principal Techniques*. UK: John Wiley and Sons, Ltd., second ed., 2009.
- [98] J. Tersoff and D. R. Hamann, "Theory and application for the scanning tunneling microscope," *Phys. Rev. Lett.*, vol. 50, p. 1998, 1983.
- [99] J. Tersoff and D. R. Hamann, "Theory of the scanning tunneling microscope," *Phys. Rev. B.*, vol. 31, p. 805, 1981.
- [100] J. Bardeen, "Tunnelling from a many-particle point of view," *Phys. Rev. Lett.*, vol. 6, p. 57, 1961.
- [101] Y. W. Chung, *Practical guide to surface science and spectroscopy*. USA: Academic Press, 2001.
- [102] E. Napetschnig, "Thin alumina films on NiAl(110) and Cu-9%Al(111): Structure, domain boundaries and nucleation and growth of metallic clusters," *TU Wien, Austria*.
- [103] S. D. Bader, "Smoke," *J. Magn. Magn. Mat.*, vol. 100, p. 440, 1991.
- [104] S. D. Bader and Z. Q. Qiu, "Surface magneto-optic Kerr effect (SMOKE)," *J. Magn. Magn. Mat.*, vol. 200, p. 664, 1999.
- [105] A. Hubert and R. Schäfer, "Magnetic domains. the analysis of magnetic microstructures.," *Springer Verlag*, 1998.
- [106] B. C. Choi, M. Belov, W. K. Hiebert, G. E. Ballentine, and M. R. Freeman, "Ultrafast magnetization reversal dynamics investigated by time domain imaging," *Phys. Rev. Lett.*, vol. 86, p. 728, 2001.
- [107] S. D. Bader and J. L. Erskine, *Ultrathin magnetic structures*. USA: Springer, 2005.
- [108] J. Zak, E. R. Moog, C. Liu, and S. D. Bader, "Fundamental magneto-optics," *J. Appl. Phys.*, vol. 68, p. 4203, 1990.
- [109] D. Stickler, R. Frömter, W. Li, A. Kobs, and H. P. Oepen, "Integrated setup for the fabrication and measurement of magnetoresistive nanoconstrictions in ultrahigh vacuum," *Rev. Sci. Instrum.*, vol. 79, p. 103901, 2008.
- [110] J. Köhler, M. Albrecht, C. R. Musil, and E. Bucher, "Direct growth of nanostructures by deposition through an Si₃N₄ shadow mask," *Physica E*, vol. 4, p. 196, 1999.

- [111] <http://www.iap.tuwien.ac.at/www/surface/sputteryield>.
- [112] <http://www.npl.co.uk/nanoscience/surface-nanoanalysis/products-and-services/sputter-yield-values>.
- [113] C. Nagl, O. Haller, E. Platzgummer, M. Schmid, and P. Varga, "Submonolayer growth of Pb on Cu(111): surface alloying and de-alloying," *Surf. Sci.*, vol. 321, p. 237, 1994.
- [114] H. Oka and K. Sueoka, "Connection of herringbone ridges on reconstructed Au(111) surfaces observed by scanning tunneling microscopy," *Jpn. J. Appl. Phys.*, vol. 44, p. 5430, 2005.
- [115] H. H. Andersen, *Nonlinear effects in collisional sputtering under cluster impact*, pp. 127–153. Det Kongelige Danske Videnskabernes Selskab, 1993.
- [116] P. Entel, E. Hoffmann, P. Mohn, K. Schwarz, and V. L. Moruzzi, "First-principles calculations of the instability leading to Invar effect," *Phys. Rev. B.*, vol. 47, p. 8706, 1993.
- [117] E. F. Wasserman, *Ferromagnetic materials*, vol. 5. Holland: Elsevier Science Publishers, 1990.
- [118] Y. Nakamura, "The Invar problem," *IEEE Trans. Magn.*, vol. 12, p. 278, 1976.
- [119] J. R. Davis, *Alloying: Understanding the basics*. USA: ASM International, 2001.
- [120] C. M. Sorensen, *Nanoscale Materials in Chemistry*. New York USA: Wiley, Inc., 2001.
- [121] S. Sun, C. B. Murray, D. Weller, L. Folks, and A. Moser, "Monodisperse Fe-Pt nanoparticles and ferromagnetic Fe-Pt nanocrystal superlattices," *Science*, vol. 287, p. 1989, 2000.
- [122] R. L. Edelstein, C. R. Tamanaha, P. E. Sheehan, M. M. Miller, D. R. Baselt, L. J. Whitman, and R. Colton, "The BARC biosensor applied to the detection of biological warfare agents," *J. Biosens. Bioelectron.*, vol. 14, p. 805, 2000.
- [123] Y. Xia, J. A. Rogers, K. Paul, and G. M. Whitesides, "Unconventional methods for fabricating and patterning nanostructures," *Chem. Rev.*, vol. 99, p. 1823, 1999.
- [124] M. R. Freeman and B. C. Choi, "Advances in magnetic microscopy," *Science*, vol. 294, p. 1484, 2001.
- [125] R. M. H. New, R. F. W. Pease, and R. L. White, "Submicron patterning of thin cobalt films for magnetic storage," *J. Vac. Sci. Technol. B*, vol. 12, p. 3196, 1994.

- [126] S. Y. Chou, P. R. Krauss, and L. Kong, "Nanolithographically defined magnetic structures and quantum magnetic disk (invited)," *J. Appl. Phys.*, vol. 79, p. 6101, 1996.
- [127] K. O'Grady and H. Laidler, "The limits to magnetic recording - media considerations (invited)," *J. Magn. Magn. Mater.*, vol. 2000, p. 616, 1999.
- [128] K. Nielsch, R. B. Wehrspohn, J. Barthel, J. Kirschner, U. Gösele, S. F. Fischer, and H. Kronmüller, "Hexagonally ordered 100 nm period nickel nanowire arrays," *Appl. Phys. Lett.*, vol. 79, p. 1360, 2001.
- [129] C. A. Ross and J. Y. Cheng, "Patterned magnetic media made by self-assembled block-copolymer lithography," *MRS Bull.*, vol. 33, p. 838, 2008.
- [130] A. Buchsbaum, M. D. Santis, H. C. N. Tolentino, M. Schmid, and P. Varga, "Highly ordered Pd, Fe, and Co clusters on alumina on Ni₃Al(111)," *Phys. Rev. B*, vol. 81, p. 115420, 2010.
- [131] B. Voigtländer, G. Meyer, and N. M. Amer, "Epitaxial growth of thin magnetic cobalt films on Au(111) studied by scanning tunneling microscopy," *Phys. Rev. B*, vol. 44, p. 10354, 1991.
- [132] J. P. Adam, J. P. Jamet, J. Ferré, A. Mougin, S. Rohart, R. Weil, E. Bourhis, and J. Gierak, "Magnetization reversal in Pt/Co(0.5 nm)/Pt nano-platelets patterned by focused ion beam lithography," *Nanotechnology*, vol. 21, p. 115302, 2010.
- [133] J. Orloff, "High-resolution focused ion beams," *Rev. Sci. Instrum.*, vol. 64, p. 1105, 1993.
- [134] J. Butschke, M. Irmischer, F. Letzkus, L. Nedelmann, and E. Platzgummer, "Resistless mask structuring using an ion multi-beam projection pattern generator," *Proc. SPIE*, vol. 6730, p. 673047, 2007.
- [135] E. Platzgummer, H. Loeschner, and G. Gross, "Projection maskless patterning (pmlp) for the fabrication of leading-edge complex masks and nano-imprint templates," *Proc. SPIE*, vol. 6730, p. 673033, 2007.
- [136] A. N. Broers, A. C. F. Hoole, and J. M. Ryana, "Electron beam lithography-resolution limits," *Microelectron. Eng.*, vol. 32, p. 131, 1996.
- [137] S. Shah Zaman, P. Dvořák, R. Ritter, A. Buchsbaum, D. Stickler, H. P. Oepen, M. Schmid, and P. Varga, "In-situ magnetic nano-patterning of Fe films grown on Cu(100)," *J. Appl. Phys.*, vol. 110, p. 024309, 2011.